UCLA
UCLA Electronic Theses and Dissertations

Title
Synthesis, photophysics, and rotational dynamics of a crystalline molecular dirotor for electrooptical applications

Permalink
https://escholarship.org/uc/item/5g29g4zt

Author
Parenzan, Alexander Henry

Publication Date
2015

Peer reviewed|Thesis/dissertation

eScholarship.org Powered by the California Digital Library
University of California

UNIVERSITY OF CALIFORNIA

Los Angeles

Synthesis, photophysics, and rotational dynamics of a crystalline molecular dirotor for electrooptical applications

A dissertation submitted in partial satisfaction of the requirements for the degree

Masters of Science in Chemistry

by

Alexander Henry Penades Parenzan

2015

ABSTRACT OF THE THESIS

Synthesis, photophysics, and rotational dynamics

of a crystalline molecular dirotor towards optoelectronic investigations

by

Alexander Henry Penades Parenzan

Master of Science in Chemistry

University of California, Los Angeles, 2015

Professor Miguel A. Garcia-Garibay, Chair

A new derivative of a crystalline linearly conjugated phenyleneethynylene molecular dirotor was synthesized for its potential in optoelectronic applications. Previously developed conjugated molecular dirotors contained a central pentiptycene stator flanked by two outer trityl stators to promote free rotation of the dual phenylene rotors. A new outer stator, the meta-terphenyl moiety, was utilized instead of the smaller trityl group in attempt to increase the free volume within the crystal of the target compound **9** and its deuterated isotopologue **11**. The increase in free volume was expected to result in decreased rotational barrier towards a freely rotating dirotor, while preserving beneficial photophysical properties within the central axle and rotor framework.

The synthesis was carried out and resulted in relatively low overall yields of compounds **9** and **11**. The low yields resulted due to the lengthy nine-step synthesis required to achieve the final product, but was mostly due to the final two Sonogashira coupling reactions. These two reactions required the reaction of high-molecular-weight hydrocarbons that could not easily dissolve in the reaction mixture and thus contributing to unsatisfactory yields. This inability to dissolve also decreased the efficiency of purification techniques, leading to poor separation via column chromatography using silica gel.

The target compound **9** was crystallized in DCM/toluene and obtaining a crystal in the space group P1-bar. Photophysical measurements were carried out on the target compound **9** and two major spectral bands were present, indicative of the presence of the meta-terphenyl and pentiptycene chromophores. The crystalline powder was also measured at 298K and 77K, yielding similar spectra with an additional band present. This band was attributed to the increased population of non-coplanar phenylene rotors. Attempts were made towards measuring fluorescence lifetime, but the lifetime was too short to achieve significant data using our instrument.

Rotational dynamics were measured using variable temperature solid-state nuclear magnetic resonance. The spectra indicated four-fold rotational dynamics in the fast regime at high temperatures, which progressed to two-fold rotational dynamics at low temperatures. Attempts were made to simulate the set of spectra and determine the kinetics and activation energy, but the suitable fitting of the spectra was unsuccessful.

The thesis of Alexander Henry Penades Parenzan is approved.

Neil K. Garg

Hilary A. Coller

Miguel A. Garcia-Garibay, Committee Chair

University of California, Los Angeles

2015

Table of Contents

ABSTRACT OF THESIS……ii

Table of Figures ……vii

Table of Schemes ……ix

Acknowledgements……x

Introduction ……1

Inorganic Electrooptic Materials……1

Organic Electrooptic Materials……5

Amphidynamic Molecular Rotors……10

Proposed Studies……16

Methods and Results ……18

Synthesis of *Meta*-terphenyl Stator ……19

Compound **1** ……19

Compound **2** ……20

Compound **3** ……21

Synthesis of Pentiptycene Stator ……22

Compound **4** ……22

Compound **5** ……23

Compound **6** ……24

Compound **7** ……25

Synthesis of Target Rotor……25

Compound **8** ……25

Compound **9** ……..…….....26

Synthesis of D_8-Rotor……..…….....28

Compound **10** ……..……..…….....28

Compound **11**……..……..……..…….....29

Crystal Growth of Target Rotor **9**……30

Single-Crystal X-Ray Diffraction……..……..…….....31

Powder X-Ray Diffraction……..…….....33

Differential Scanning Calorimetry and Thermogravimetric Analysis……34

Photophysical Studies……35

Solid-State D-NMR……37

Conclusions……39

Future Studies……40

Experimental……41

Appendix……..49

Table of Spectra……..……..49

References…….....90

Table of Figures

Figure 1: Integrated phase modulator 2

Figure 2: Integrated intensity modulator 3

Figure 3: Integrated wavecoupler 4

Figure 4: Nematic phase (left) and calamitic molecule (right) 6

Figure 5: Layered-view of a typical liquid crystal cell 7

Figure 6: Top and bottom layer arrangement (a) and helical arrangement (b) 8

Figure 7: 'OFF' and 'ON' state of a liquid crystal 9

Figure 8: Space filling model and cartoon of target rotor **9** 11

Figure 9: Molecular compass(left) and macroscopic compass (right) 12

Figure 10: Modulation of pi-system by rotation of phenylene rotor 13

Figure 11: Directed alignment of rotor by external field 14

Figure 12: Ferroelectric (left) and antiferroelectric (right) crystals 15

Figure 13: Target compounds for proposed investigations 17

Figure 14: H^1 NMR comparison of **3**, **8**, and **9** 28

Figure 15: Single X-ray crystal diffraction of **9** 31

Figure 16: Crystal-packing structure of **9** 32

Figure 17: Powder X-ray diffraction of **9** 33

Figure 18: Absorbance spectrum of **9** 34

Figure 19: Solution (a) and Solid-state(b) fluorescence spectrum of **9** 35

Figure 20: TGA (a) and DSC (b) of **9**..... 37

Figure 21: Solid-state NMR of **9** 38

Table of Schemes

Scheme 1……18

Scheme 2……19

Scheme 3……20

Scheme 4……20

Scheme 5……21

Scheme 6……22

Scheme 7……23

Scheme 8……24

Scheme 9……24

Scheme 10……25

Scheme 11……26

Scheme 12……27

Scheme 13……29

Scheme 14……30

Acknowledgements

I am extremely thankful for the knowledge and guidance which I acquired while contributing to the research within the Garcia-Garibay research group. Most importantly, I am grateful for the opportunity that Prof. Garcia-Garibay granted me by allowing me to operate creatively within the laboratory, as well as providing the necessary criticisms to promote advances in my overall scientific knowledge.

Also, the research group as a whole was instrumental towards the advancement of my research, and thus I am very thankful for their assistance and guidance throughout these past years. In particular, I'd like to thank Jean-Luc for his constant mentorship within the laboratory, and his assistance with many experiments present throughout this work.

Introduction

This thesis reports the design, synthesis, photophysics, and rotational dynamics of a crystalline molecular gyroscope that is proposed to have beneficial optoelectronic properties. Optoelectronic materials are typically composed of either inorganic or organic materials and are utilized to manipulate photophysical properties of materials such as index of refraction, absorbance, and fluorescence. An external electric field can be generated by a capacitor, which then causes a change in the internal order of the material, thus leading to modulation of spectroscopic properties. By changing these spectroscopic properties, most notably, the index of refraction, the frequency and phase of light wave can be altered quickly and reversibly. This offers opportunities for the introduction of fast-switching reversible spectroscopic properties into technology.

Inorganic Electrooptic Materials

Throughout modern technology, a variety of inorganic materials have been constructed for usage in optoelectronics. These materials include NH_4, NPO_4, KH_2PO_4 $LiNbO_3$, $LiTiO_3$, and CdTe among others. One of the more common materials utilized is $LiNbO_3$ because of its notable ability to change its refractive index under exposure to an external electric field. This modulation of refractive index leads to the changes in the light-waves frequency and phase.[2]

An example of how one of these devices could be constructed to modulate the phase of a light wave is depicted in Figure 1. There are four main components that

allow the device to function including the electrodes, the waveguide, the inorganic material, and the light source. Firstly, the light source is directed towards the capacitor by the waveguide. The waveguide is typically constructed of titanium, and is especially useful because it reduces the scattering of light. Once the light is transported by the waveguide, it is then guided towards the electrodes. The electrodes have the ability to change the refractive index of the material, and thus the light will change its phase and frequency according to the electric field supplied by the capacitor. This ultimately leads to the output light having a different phase and frequency compared to the input light.[2]

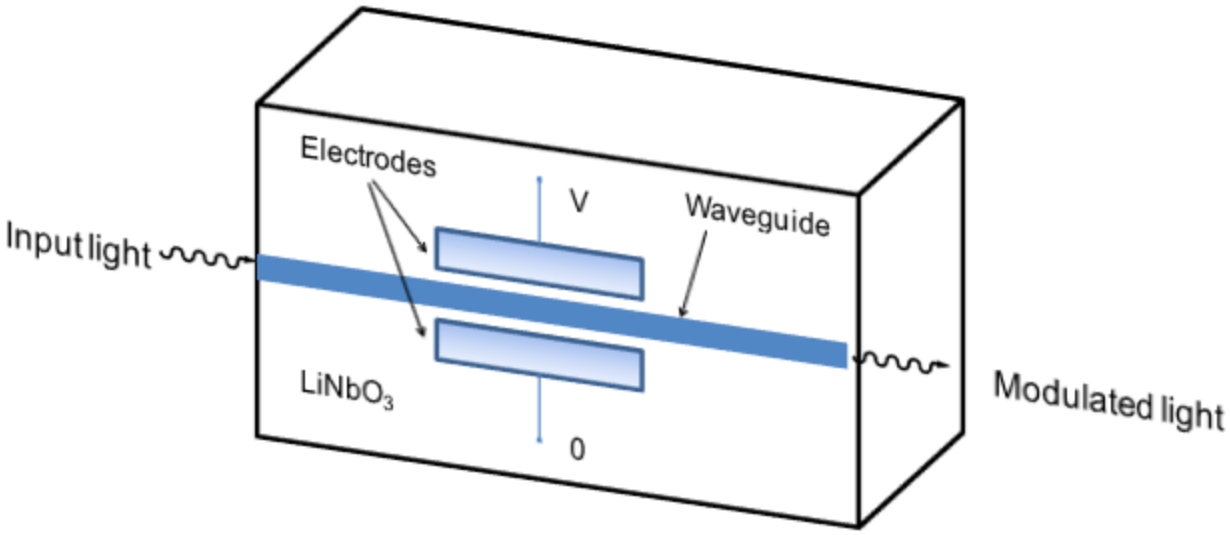


Figure 1: Integrated phase modulator[1]

Another property of the light wave that can be modulated is the intensity and this process is depicted in Figure 2. In an integrated intensity modulator, a beam of light can be directed towards the waveguide, similar to Figure 1. But, in this case, the wave guide has two paths: one that directs towards the capacitor and another that directs away

from the capacitor. This causes the light wave's phase to be changed in one path, but remain the same while travelling through the alternate path. When the two light waves converge near the end of the waveguide, the interference of the converging waveforms ultimately leads to the modulation of the intensity of the original waveform, depending on the applied voltage of the electrodes.[2]

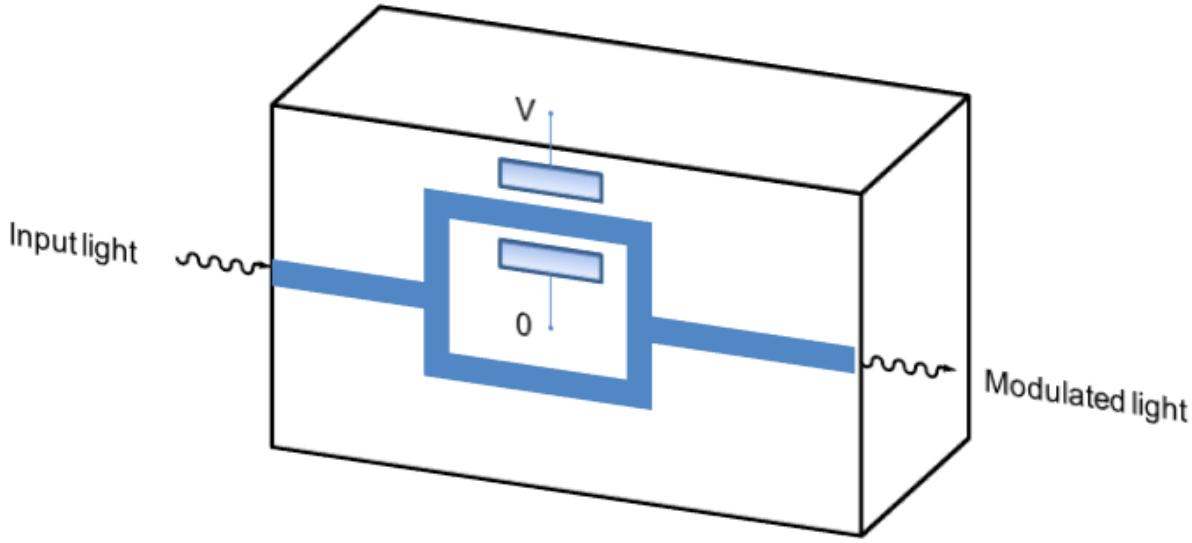


Figure 2: Integrated intensity modulator[1]

Previously demonstrated in Figure 1 and 2 was the modulation of the light wave's intensity and phase. The index of refraction can also be modulated to change the direction of the wave path. This can be carried out through the usage of an integrated directional coupler, as seen in Figure 3. Once again, an electric field in the form of two electrodes is utilized to modulate the light wave's refractive index. In this particular example, fiber optics is used to direct the light beam towards two electrical paths. Light is directed into one of the optical fibers and is then sent towards the electrical field, where both of the waveforms converge. At this point of convergence, the input light can

be transferred to the opposite waveguide by altering the length (L) of the electrodes and the electrode spacing distance (d). Upon transfer to the opposite waveguide, the light can then exit through the opposite wave path.[2]

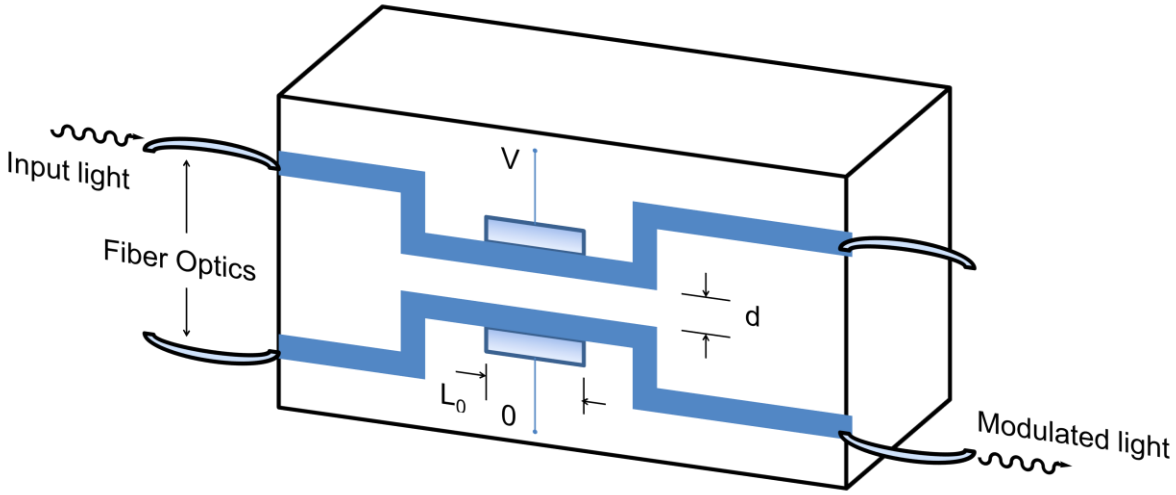


Figure 3: Integrated directional coupler[1]

These processes describe in the three aforementioned figures have a wide range of usage throughout the electronic industry. Unfortunately, due to these inorganic materials lacking sensitivity to an external electric field, they require fairly powerful voltage sources to achieve desirable results. Typical frequencies of the waveforms are employed in the gigahertz regime and requiring power sources around 10^6 V/m. This is not achievable for smaller-scale hand-held electronics, including watches, cell-phones, and calculators. Organic optoelectronics are much more applicable for this application because they are more sensitive to modulation by an external electric field and can be viable with lower voltage power sources.

Organic Electrooptic Materials

Beyond the aforementioned inorganic materials, organic materials are also of wide interest to technological industry because of their similar features. The most prominent class of organic optoelectronic materials is the liquid crystal. They are called liquid crystals because their varying properties of diffusion and organization lend them characteristics of both the solid and liquid phase. They were firstly discovered in 1888 by Austrian botanical physiologist Friedrich Reinitzer, while he was examining cholesterol derivatives. He noticed that cholesteryl benzoate had a peculiar melting pattern. It melted first into a cloudy liquid and then as the temperature continued to increase, the cloudy liquid became clear again.[3]

Friedrich was further interested in the cause of these melting patterns and sought help from a physicist, Otto Lehmann, who noticed that crystals existed in the cloudy sample. Further investigations revealed that these cholesteric crystals had a variety of properties: most importantly their ability to rotate the polarization of light. In 1962, this monumental discovery eventually led to the development of liquid crystal displays at RCA laboratories, and the eventual replacement of cathode ray vacuum tubes used in televisions, proving their importance in technological industry.[3]

Liquid-crystal phases can be found in a variety of packing motifs and can be characterized based off attributes such as positional order (packing of the molecules), orientation order (directionality of the molecule), and the range of the order (long or short). One of the most common liquid crystal phases is the nematic phase in which there is no short range positional order, but there is long range directional order as seen

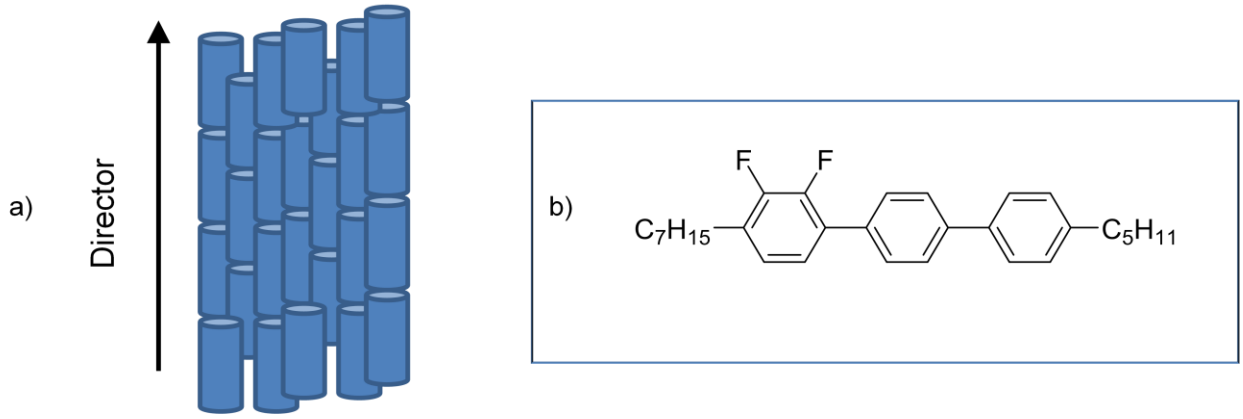


Figure 4: Nematic phase (left) and calamitic molecule (right)[1]

in Figure 4a. These nematic phases depicted in Figure 4b, are formed by aggregates of rod-shaped organic molecules known as calamitic molecules. This specific phase type is interesting because it can be easily directed by an external electric field, which is necessary for the liquid crystal display to function by changes in morphology.

A mesogen or a calamitic molecule, is a compound that displays liquid crystal properties. As seen in Figure 4a, the rod-shaped molecules order in such a way that the long-range order is evident, but the short range is order is not optimal. In Figure 4b, the most important properties of the calamitic liquid crystal can be observed. The rigid rod-like polyphenyl backbone functions as the scaffold for organization (the mesogenic part), the flexible alkyl chains offer additional mobility, and the fluorine substituents improve alignment with the electric field. These calamitic molecules can be integrated in a specific manner to produce a liquid-crystal display.[3]

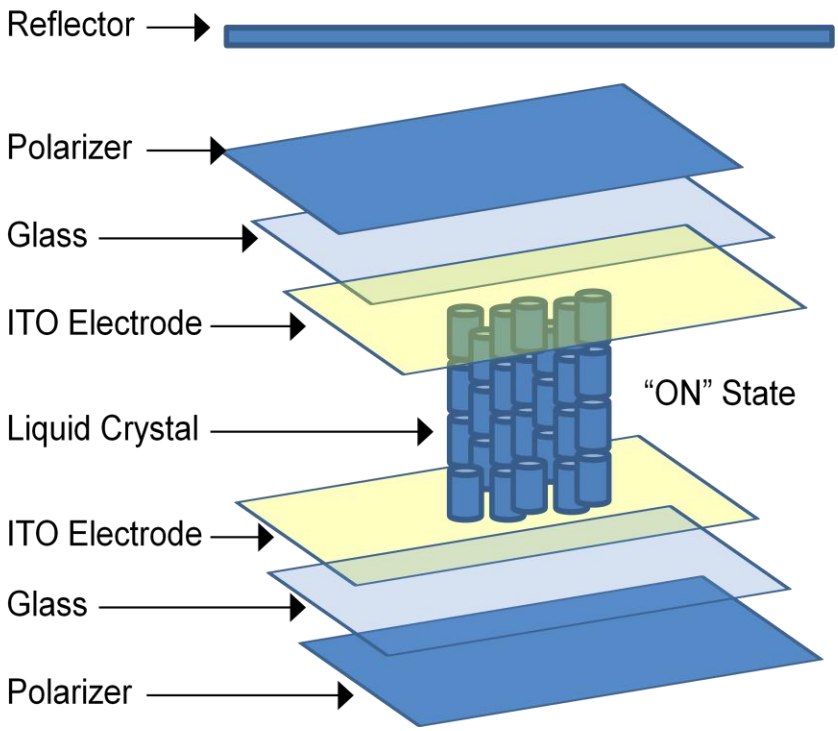


Figure 5: Layered view of a typical liquid crystal cell.

The architecture of a liquid crystal display involves five primary components depicted in Figure 5. Firstly the light enters through the polarizer at the bottom of the diagram, causing the light to incur a specific direction of polarity. This light then travels through the glass and liquid the crystal, where the polarization of the light can be further altered depending on the state of the crystal. The ITO electrodes control the morphology of the crystal by generating an external electric field. While this external field is active, the crystal structure enters the aligned nematic state, allowing light to pass through without change of polarization. This causes the light to be absorbed at the oncoming polarizer because the two polarizers' directions are perpendicular to each other.[3]

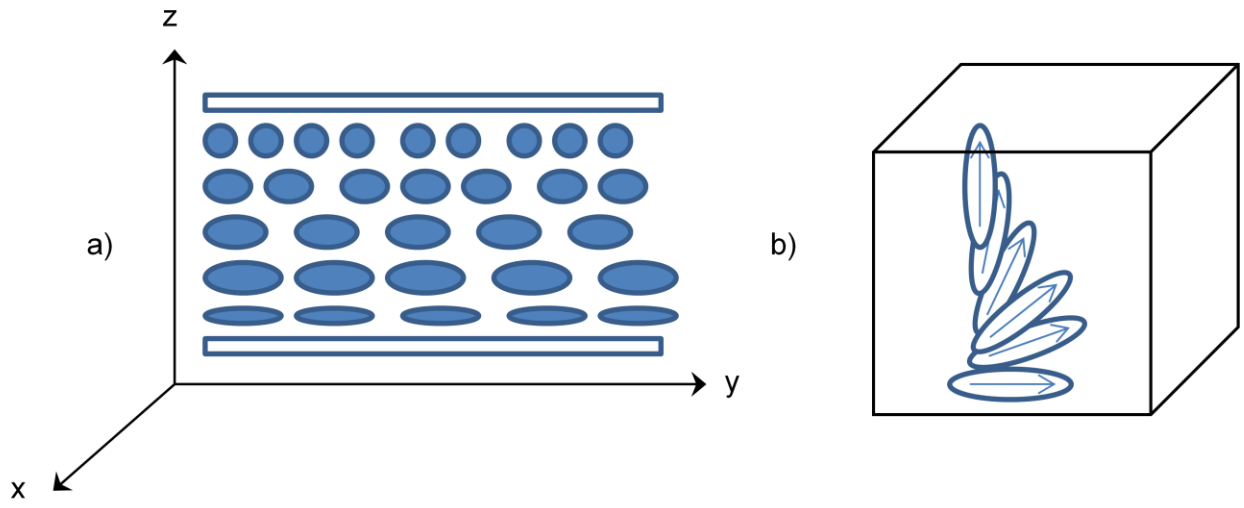


Figure 6: Top and bottom layer arrangement (a) and helical arrangement (b).[1]

If the external field is not being applied, the liquid crystal will revert to the helical arrangement depicted in Figure 6a. This diagram shows the structure looking down the individual rods. The rods are firstly held in place by two films depicted in Figure 6b. Each film has the crystal deposited on the layer, with the overall directionality being of 90 degrees difference. This gradient of directionality difference can be seen clearly in the cubic view of Figure 6b. The direction of the arrow at the bottom of the cube is 90 degrees different in comparison to the top of the cube. This is of significance because as described earlier, the polarizers are situated so their directionalities are perpendicular to each other. The 90 degree helical turn will cause the light-wave to induce a 90 degree directionality change in polarization, and thus pass through the filter.

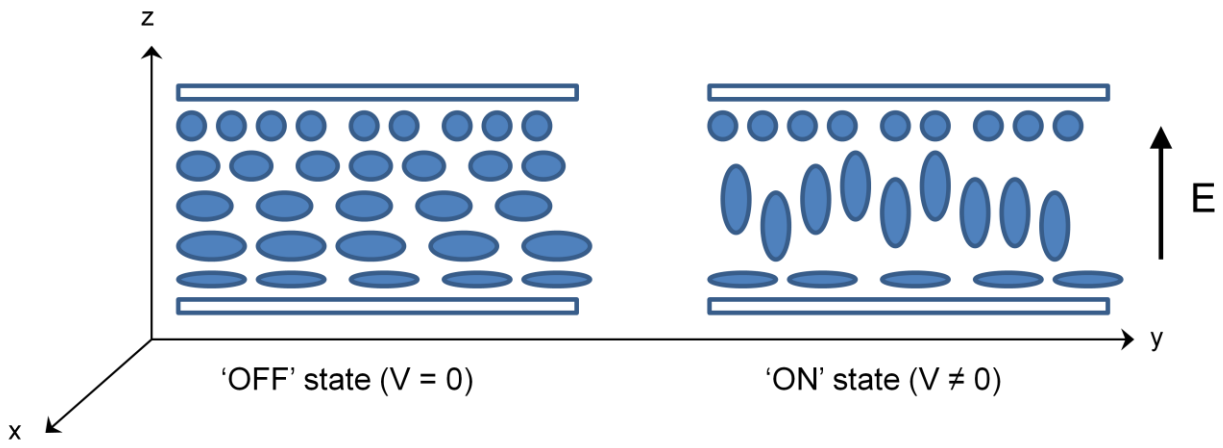


Figure 7: ‘OFF’ and ‘ON’ state of a liquid crystal cell.[1]

The different states of the crystalline packing can be seen in Figure 7. The applied voltage produces the external field which causes the liquid crystal to reach an organized ‘ON’ state, which is quickly reverted to the helical ‘OFF’ state. While in the ‘OFF’ state, the directionality of the calamitic molecules are helical and 90 degrees in difference between the two polarizers, thus allowing the light to go through, reflect backwards, and emit light. When the voltage is applied and in the ‘ON’ state, the more organized nematic phase is obtained and the direction of polarity is not modulated, causing the light to be absorbed at the polarizer and thus not observed.

This process can be undergone reversibly and extremely quickly, but the major limiting factor in reversibility is the required change in structural shape. If the overall shape of the crystalline structure is not altered during the switching process, reversibility could be achieved much more rapidly. The most effect liquid crystal displays can only achieve a temporal resolution of approximately 20 microseconds, but if this process

were controlled by the rotation of a single molecule, the nanosecond regime is plausible.

Amphidynamic Molecular Rotors

A machine can be simply defined as an object that uses energy to perform an action. These machines exist throughout the universe with macroscopic functions, as immense as large galaxies that are gravitationally set in motion by their large centers of mass, or, with nanoscopic functions, as small as the molecular absorption of a photon inducing a conformational change. Recently in literature, a large amount of interest has been directed towards the topic of “molecular machinery.”

The quintessential example of a complex molecular machine is a protein located in the mitochondria of the cell, known as ATP synthase. ATP synthase functions as a molecular gear that is electromechanically driven by the flux of protons across the lipid bilayer. This electrical flux of protons induces conformational changes within the active site, causing a three-fold rotation[4], eventually leading to the synthesis of ATP.

Although proteins like ATP synthase provide efficient machinery with extremely dynamic and selective mechanisms of action, their machinery is very complex, due to the massive amount of molecular parts involved in their systems[5]. Much smaller, less complex processes can be utilized, such as the photoisomerization of azobenzene[6], to gain an elementary understanding of how nanomachines operate. In this specific study, the nanomachine of interest mimics the mechanism of a macroscopic gyroscope[7].

A gyroscope, very similarly to a compass is a device that is designed to measure or maintain an orientation on a fixed axis and is primarily composed of three components[5]: an axle, rotator, and stator. In order for a compass to be functional, the rotation must be able to occur easily, otherwise the compass is useless. Similarly with the molecular version of the compass, the rotor portion must be able to rotate as easily as possible to imbue the molecule with functionality. This free space is clearly depicted in the space-filling model of the target molecule (Figure 8). The outer and inner stators provide a framework around the molecule which shields the phenylene rotor from clashing with surrounding atoms.

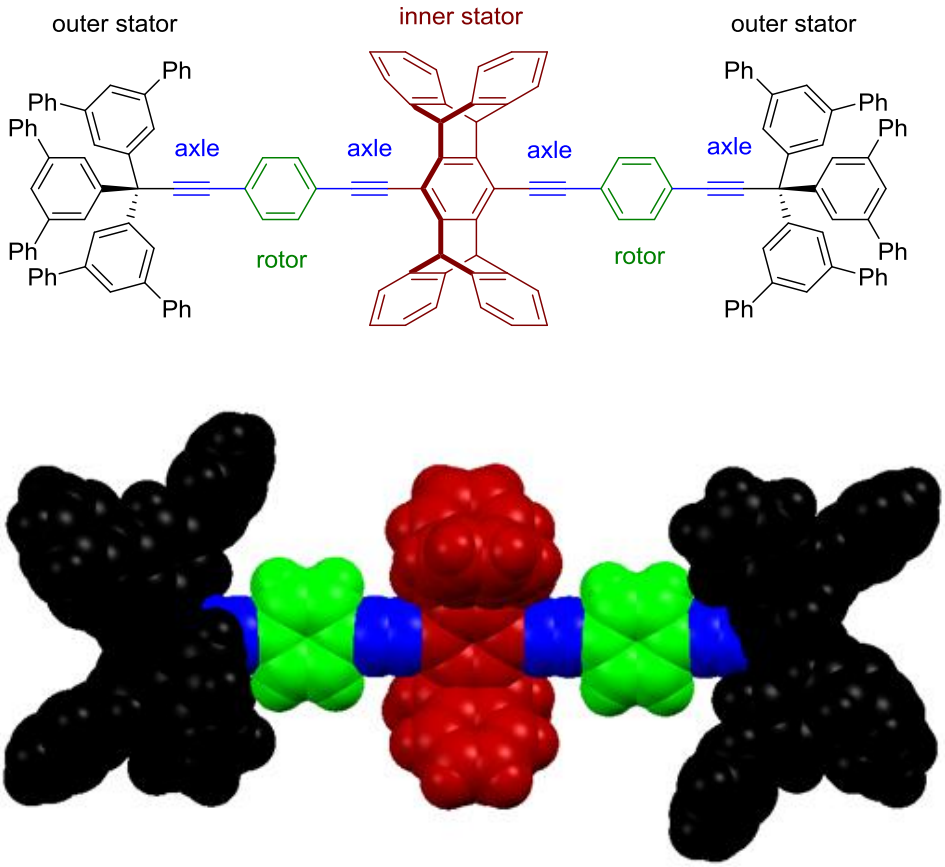


Figure 8. Space filling model and cartoon of target rotor **9**.

Within the target molecule **9** (Figure 8b), the axle is embodied by the rigid chain of the four successive ethynyls. The rotors are defined by the two phenylene rings and rotationally confined by the ethynyl-defined axis. The ethynyl linkers provide an ideal framework for mimicking the properties of an axle because of its cylindrical shape granted by the surrounding pi electrons. The inner pentiptycene and the two outer *meta*-terphenyl groups function as the stators, functionally shielding the rotating phenylene groups and providing space for rotation within the crystal lattice.

A macroscopic compass (Figure 9) contains an enclosing box functioning as a stator, a rotor in the center, and an axle acting as the director. The axle provides the axis that the rotor can spin on, the rotor provides the functional piece that rotates dynamically, and the stator assists in fixing the spin axis, while also providing the rotor with an optimal amount of space[8] to freely rotate within a crystalline state. Like the macroscopic compass, the molecular compass also contains an axle, rotor, and stator.

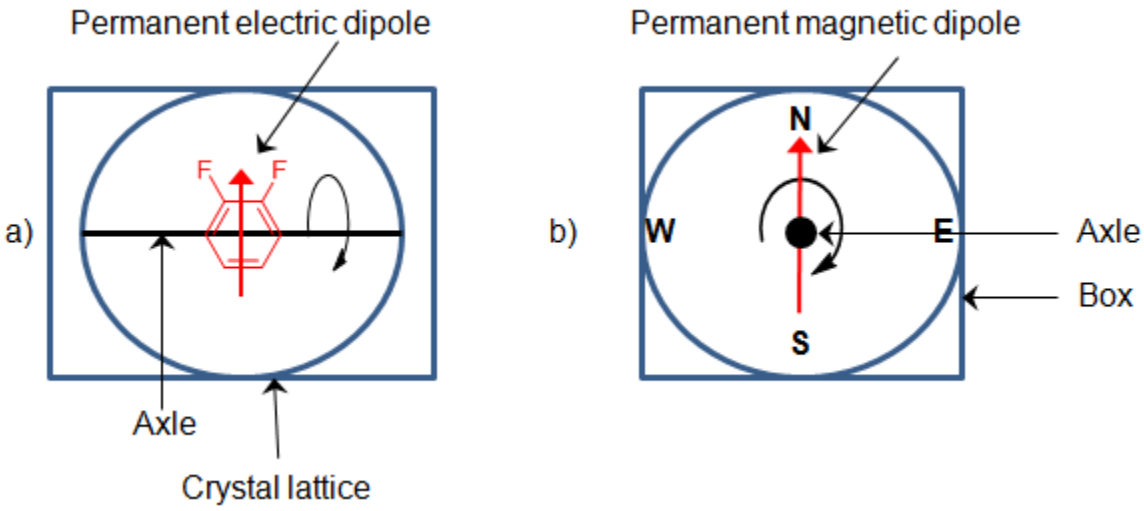


Figure 9. Molecular compass (left) and Macroscopic compass (right)

By providing a chromophoric molecule that can be modulated by the orientation of the rotors (Figure 8) a multi-state nanomachine can exist that is functionally driven by the extent of conjugation in the pi system.[9] Poly(arylacetylenes) are dynamic systems which contain equilibriums of the coplanar and twisted state. These systems are very appealing because the electronic communication can occur dynamically along the conjugated system. The orientation of the pi-system within the alkyne linkers and the central ring remains constant, but the outer phenyl rings rotate dynamically. The cylindrical symmetry of the triple bond causes the alkyne's shape to remain constant, while the phenyl-ethynyl bond rotates. In Figure 10, the equilibrium is demonstrated with each additional phenylene rotation of 90 degrees leading to a blue shift of the absorbance spectrum. The magnitude of this blue shift was experimentally determined as a 22 nm shift by using a 1,4-bis(phenylethynl)benzene molecule as the model.[11]

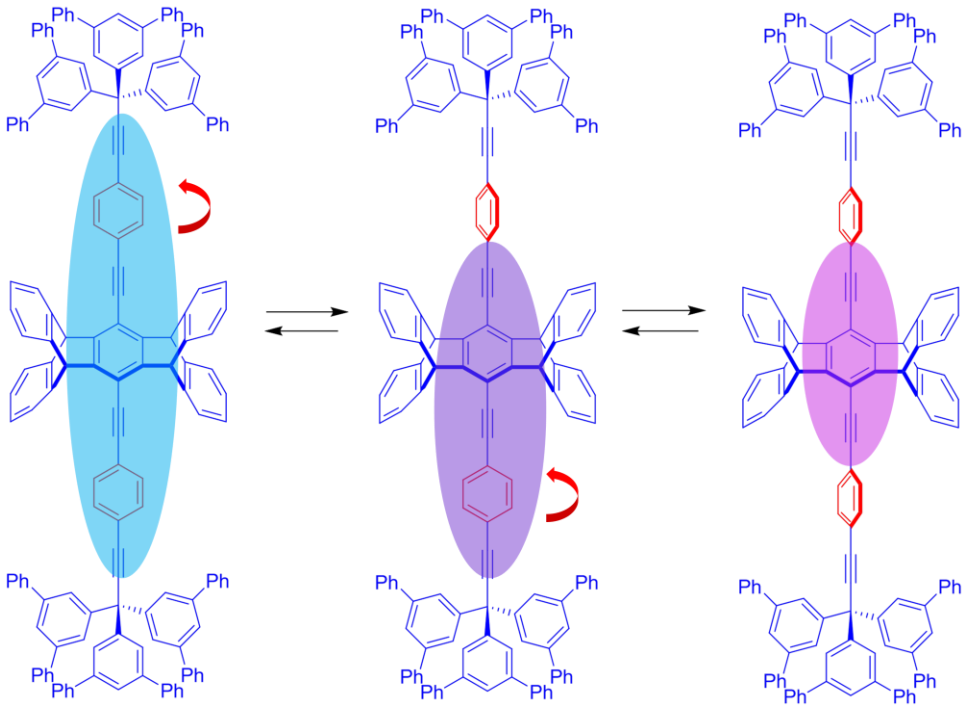


Figure 10. Modulation of pi-system by rotation of phenylene dirotor

It has been demonstrated that by using frequency dependent dielectric spectroscopy, the permanent dipole on a molecular rotor can be interfaced with an external electric field.[10] By functionalizing the phenylene rotors with fluorine (Figure 9) a permanent dipole could be created, which could interact with an external electric field and function as a rotating molecular switch. As the orientations of the two rotors differ between the three possible permutations, different spectroscopic properties arise, ultimately resulting in a functional molecular change. It is our goal to further harness the functional properties of this previously created gyroscopic molecular framework by providing additional modifications on the outer stator.[10] It is expected that by increasing the steric bulk of the outer stators, the dual phenylene rotators will be able to gain more rotational freedom, because of a more spatially optimized crystalline arrangement.[8]

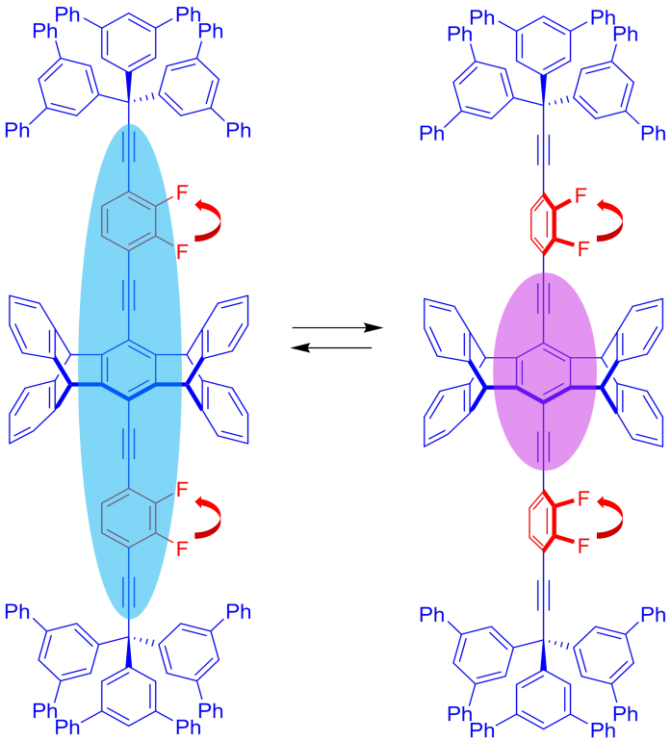


Figure 11. Directed alignment of rotor by external electric field

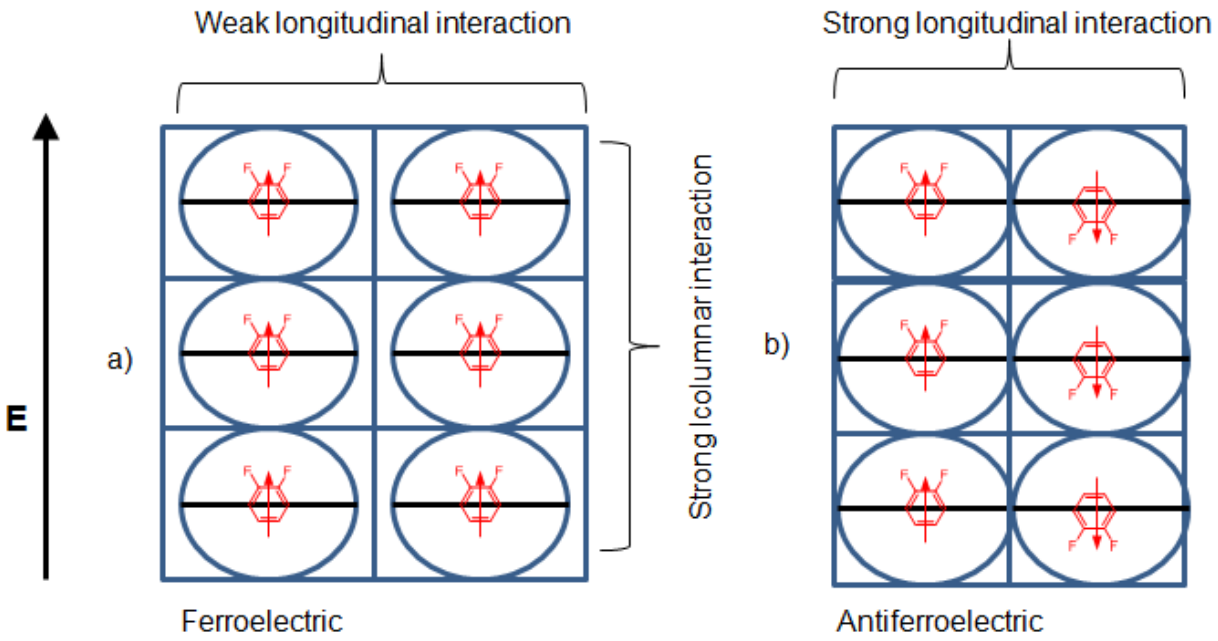


Figure 12. Ferroelectric (left) and antiferroelelctric (right) crystal lattice.

Unlike a regular macroscopic compass which has just one box, the crystalline framework has multiple interconnected boxes. This leads to additional possible interactions between each compass, depending on the distance of the fluorine-functionalized positions. If the rotors are separated appropriately, there will be a reduction of longitudinal interactions, and the ferroelectric effect will occur (Figure 11a). If the rotors are not separated effectively, then strong longitudinal interactions will occur (Figure 11b). In order to prevent the antiferroelectric effect from occurring, the pentiptycene and *meta*-terphenyl stators are necessary, for providing separation.

Proposed Studies

The primary goals of this research project included 1) to develop a synthetic and crystal growth strategy towards achieving the target compound in a crystalline state, 2) to investigate the photophysical properties of the system, and 3) to determine the rotational dynamics of the dual phenylene rotors.

Our primary interest is to determine the effect of replacing the previously utilized trityl moieties, with the more bulky *meta*-terphenyl substituents. This replacement was expected to confer more free space within the crystal lattice, leading to faster rotation and ultimately free rotation.

Fluorescence spectroscopy will be utilized to study the photphysical properties of compound **9**. Rotational dynamics and kinetics will be studied via solid-state nuclear magnetic resonance to determine the capabilities of the dirotor.

If the effect of the *meta*-terphenyl substituents is as pronounced as expected, fluorine functionalization can be achieved as illustrated in Figure 13. The fluorine functionalized rotor could then be used to study its photophysical properties while under the effect of an external electric field. These properties could be used as a benchmark towards further developing fast-switching optoelectronic materials.

Within the body of work, the synthetic scheme is first presented for the precursor meta-terphenyl ethynyl **3**, and the precursor pentiptycene diethynyl molecule **7**. The two precursors are then synthetically converged to produce the target natural abundance dirotor **9** and deuterated dirotor **11**. The relevant spectra can be referred to within the appendix section.

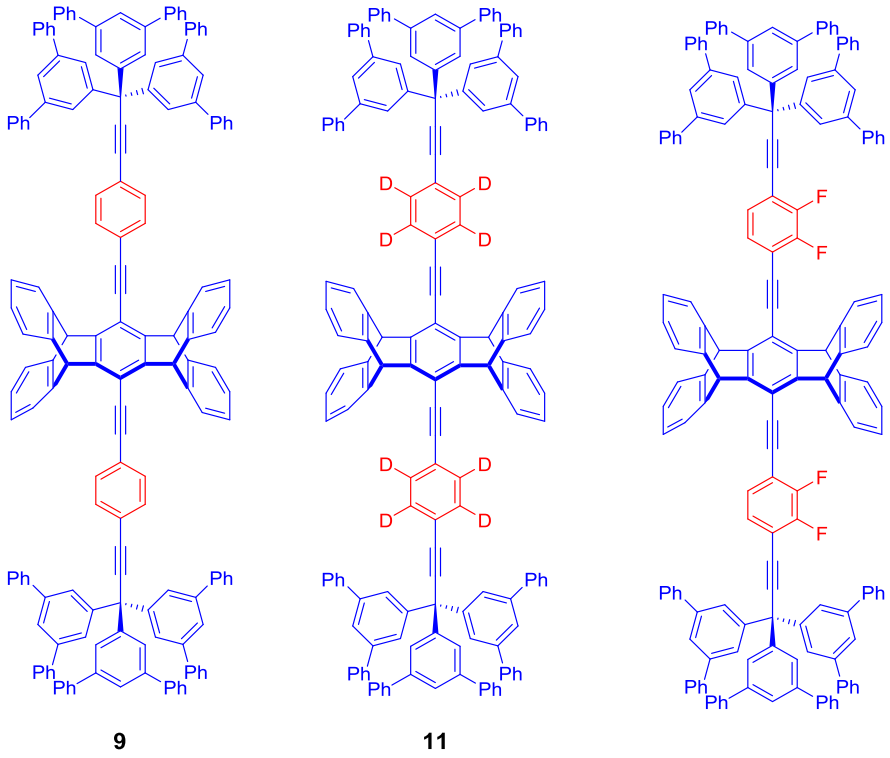


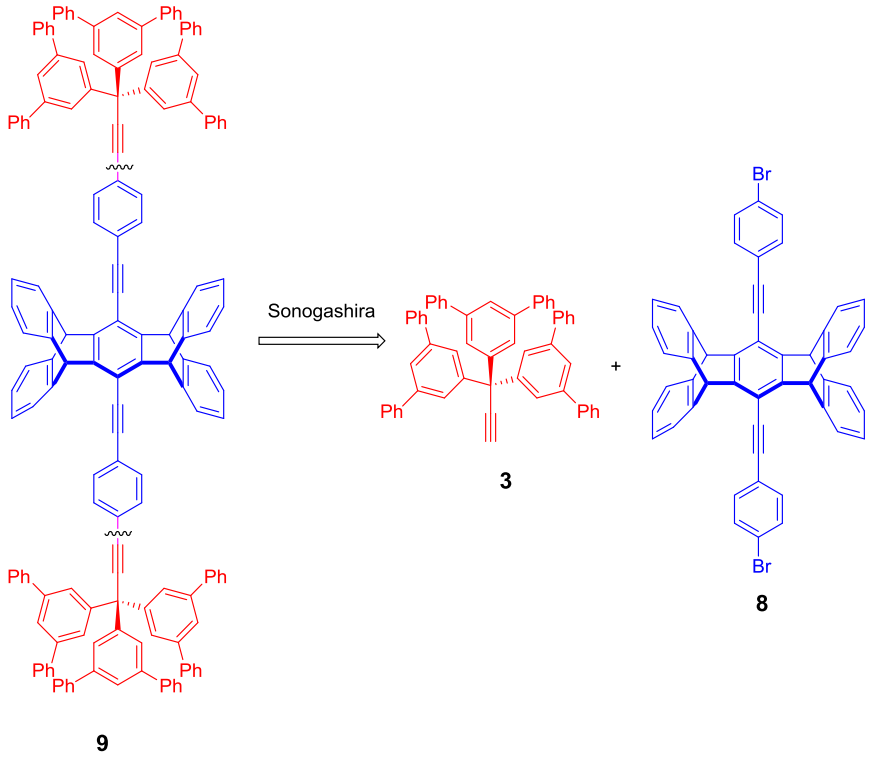
Figure 13. Target compounds for proposed investigations.

Methods and Results

Synthesis

Syntheses of compound **3** and compound **7** were carried out using previously developed procedures by Yang and Matusmoto .[14-15] A convergent scheme was first attempted, but was unsuccessful in attaching the 4-bromophenyl substituted diethynyl pentiptycene **7** to the 3,3,3-tri(meta-terphenyol)-propyne **3**. The divergent synthetic scheme utilized to couple the precursor meta-terphenyl **3** and diethynyl pentiptycene **8** is illustrated in Scheme 1.

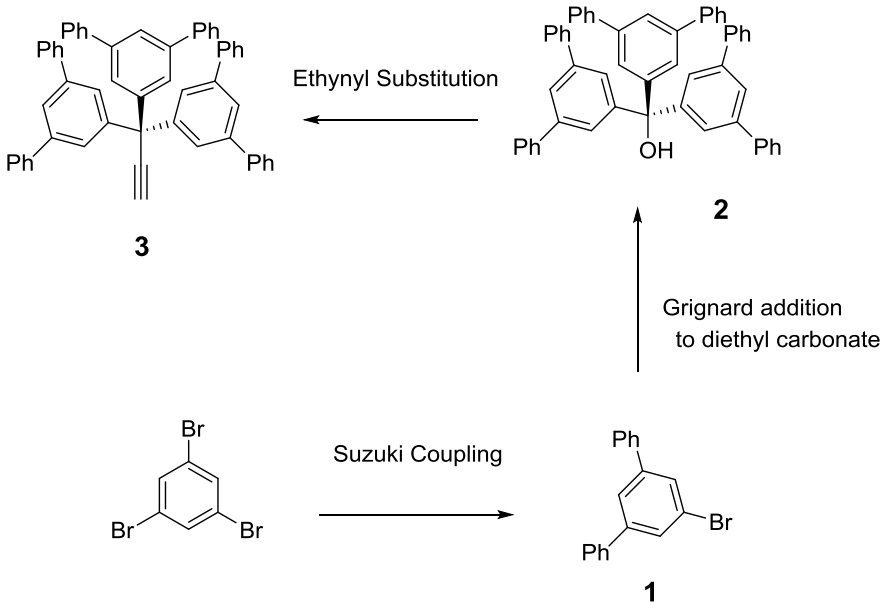
Scheme 1



9 **3** **8**

Synthesis of 3,3,3-tri(*meta*-tephenyl)-propyne

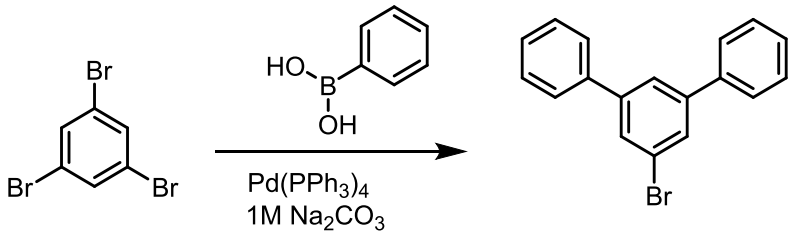
Scheme 2



Compound (1)

With samples of the central pentiptycene stator linker successfully confirmed by comparison to literature, the outer *meta*-terphenyl methyl stators (**3**) could be synthesized to eventually be linked together with **7**. This synthesis was adapted according to the procedure[14] adapted by O'Brien and coworkers. To begin the synthesis, a Suzuki coupling was performed with 1,3,5-tribromobenzene and two equivalents of phenylboronic acid, to produce the preferred diphenyl substituted product (**1**). The product was confirmed via H^1/C^{13} NMR by the presence of the aromatic peaks which closely matched with literature and also mass spectroscopy, producing a 308.01908 m/z signal, closely corresponding to the expected 308.01951 m/z.

Scheme 3

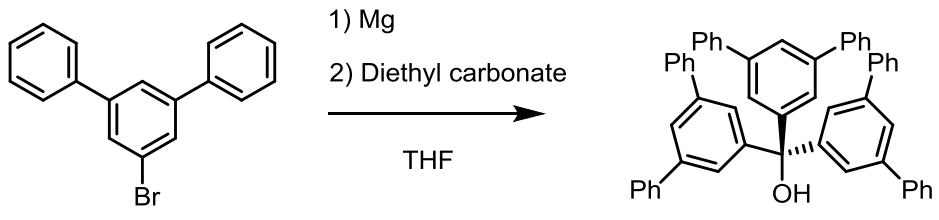


1

Compound (2)

Compound **1** was thereafter reacted with magnesium to form the Grignard reagent, which was subsequently utilized to react three equivalents with diethyl carbonate, eventually forming the know tri(*meta*-terphenyl)methanol compound (**2**).[14] Compound **2** was confirmed by a mass spectroscopy, producing a 720.18215 m/z signal, closely corresponding to the expected 720.338676 m/z. The 13-C NMR also produced the eight unique carbons in the aromatic region of 125-150 ppm, as well as the distinct sp^3 methanol carbon at 83 ppm. 1-H NMR produced the 5 expected proton signals in the 7-8 ppm aromatic region, as well as the expected alcohol proton located at 3 ppm.

Scheme 4

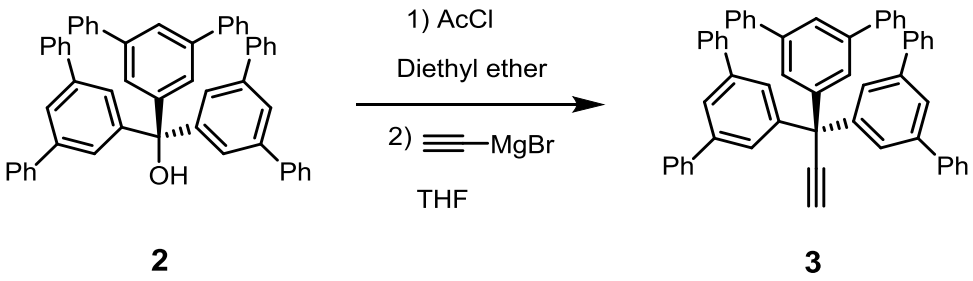


1 **2**

Compound (3)

Compound **2** was treated with acetyl chloride to form the corresponding triaryl chloride, followed by a reaction with ethynylmagnesium bromide to form the desired tri(meta-terphenyl)methyl ethynyl stator.[14] The formation of compound **3** was confirmed by mass spectroscopy, producing a 724.31717 m/z signal, closely corresponding to the expected 724.31245 m/z. 1-H NMR produced the 5 unique proton signals in the 7.3-7.8 ppm aromatic region, as well as the unique alkynyl proton located at 2.9 ppm.

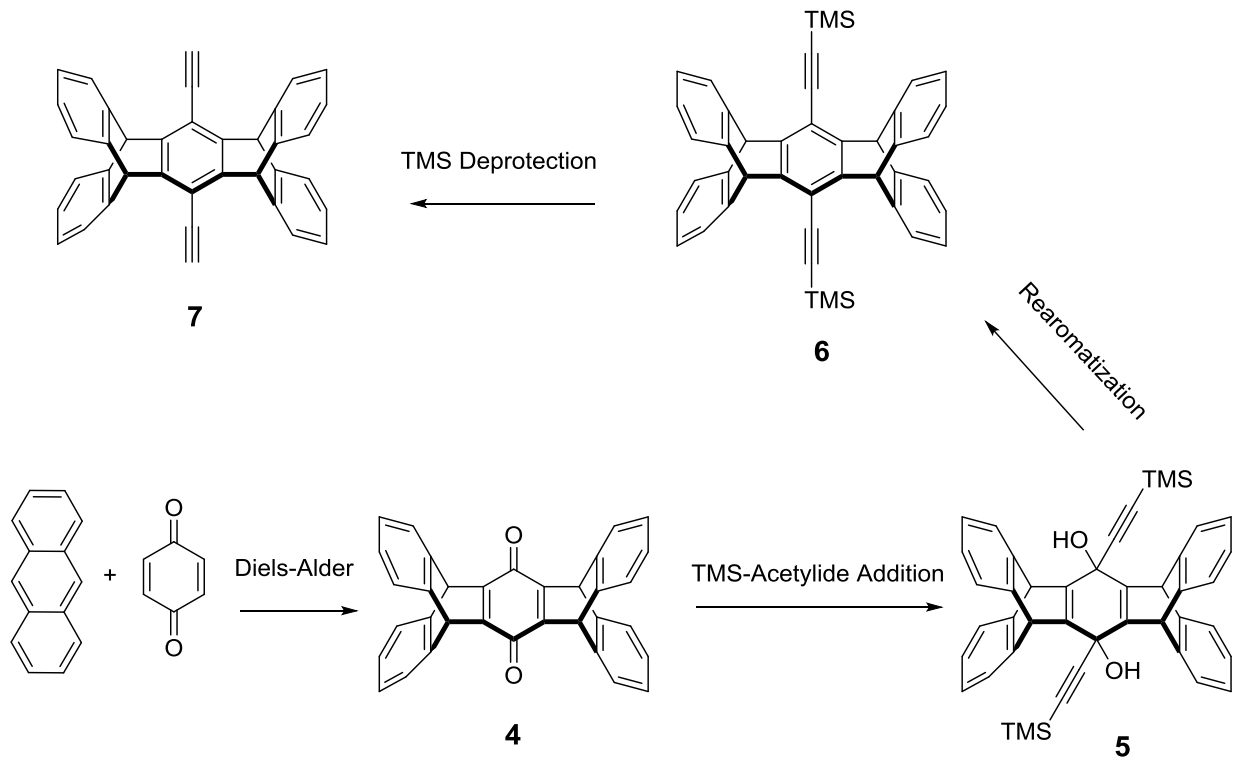
Scheme 5



2 **3**

Synthesis of Pentiptycene Stator

Scheme 6

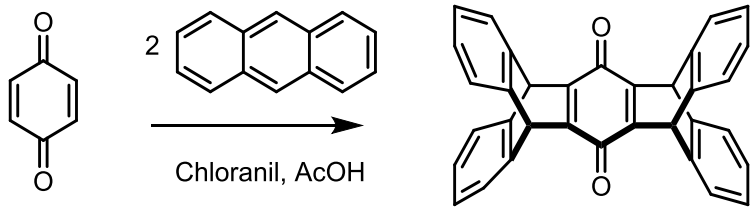


Compound (4)

The central pentiptycene stator component (**7**) was synthesized via the 4-step synthesis depicted in Scheme 1, according to the procedure[15] adapted by Hughs and coworkers. Firstly, pentiptycene (**4)** was formed via a Diels-Alder reaction of quinone and two equivalents of anthracene. The presence of **4** was confirmed via mass spectroscopy, yielding a 460.1469 m/z, which closely matched the expected mass of 460.14578 m/z. Also the two unique protons were present in the aromatic region at~7 ppm, as well as the bridgehead proton at 5.8 ppm . The C=O stretch was located 1650

cm^{-1} confirming the presence of the carbonyl peak, as well as the aromatic and aliphatic bridgehead C-H stretches located between 2950-3100 cm^{-1}.

Scheme 7

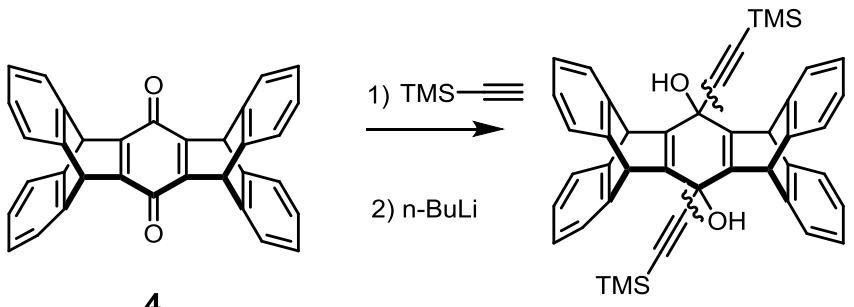


4

Compound (5)

Next, TMS-acetylene was deprotonated by n-BuLi to form TMS-ethynllithium, which ultimately performed nucleophilic additions on the dual carbonyl positions of **4**.[15] The resulting compound **5** was confirmed by mass spectroscopy, yielding the characteristic mass of 656.254 m/z, closely matching the expected 656.256 m/z. Also the presence of the newly added functionalities was ascertained via ^{1}H NMR: hydroxyl at 1.64 and the methyls at 0.46. The presence of the added alkynyl group was identified by the ^{13}C NMR peak at 52.1 ppm. The newly acquired alkyne C-C stretch were present in the IR spectrum at ~2200cm^{-1}, as well as the O-H stretch located at 3500 cm^{-1}.

Scheme 8

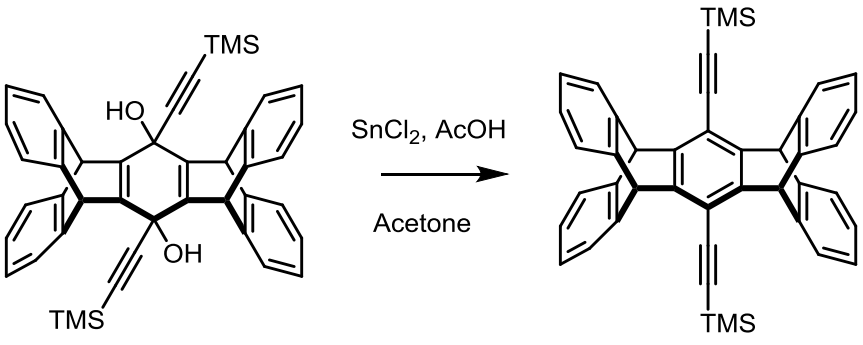


4 **5**

Compound (6)

Next, tin chloride (II) was utilized to facilitate the elimination of the dual hydroxyl groups, leading to the rearomatization of the central pentiptycene ring, and the production of the TMS-ethynyl substituted pentiptycene (**6**).[15] The alcohol (3500 cm^{-1}) functionality was no longer found on the IR spectra. On the proton NMR, the hydroxyl proton was also no longer present at 1.8 ppm as expected.

Scheme 9

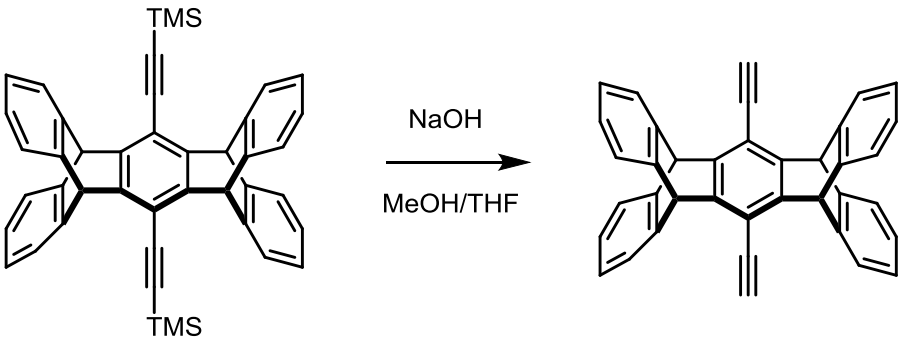


5 **6**

Compound (7)

The TMS substitutents were thereafter removed[15] with sodium hydroxide, and the loss of the TMS signal at ~0 ppm and the hydroxyl signal at ~1.6 ppm was confirmed via H-1 NMR. This high symmetry product (**6**) contained four unique protons. The two aromatic protons were identified by multiplets at 7.35 ppm and 6.95 ppm, the singlet bridgehead proton was identified by its distinct peak at 5.9 ppm, and the singlet alkynyl proton was found at 1.9 ppm. The alkyne C-H was also confirmed by the presence of a newly acquired peak at 3300 cm^{-1}. These characteristics confirmed the presence and successful synthesis of the central pentiptycene stator linker.

Scheme 10



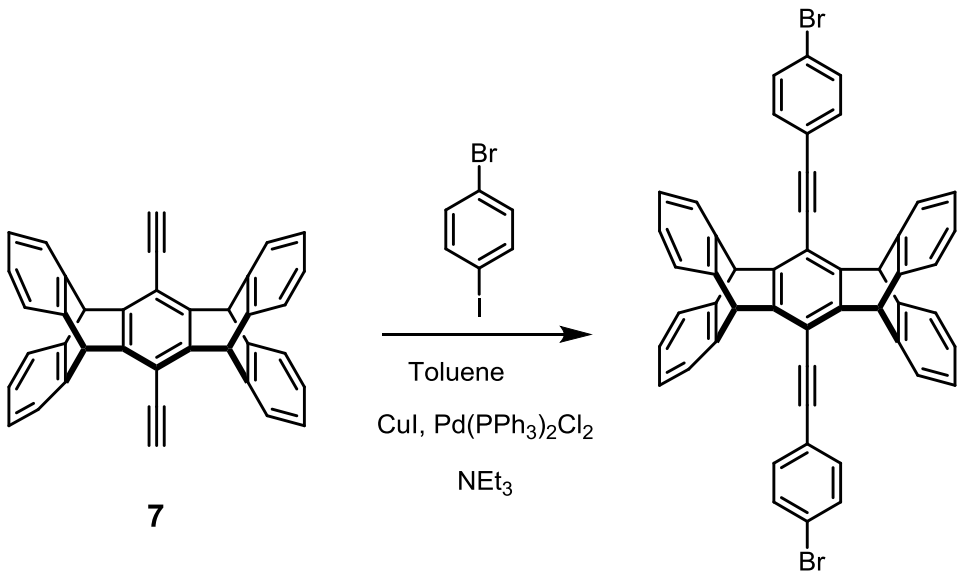
6 **7**

Compound (8)

The central stator, compound **7**, was next coupled with 1,4-bromoiodobenzene, using a Sonogashira coupling, which successfully formed the bromophenyl-substituted

compound **8**. The presence of the compound **8** was confirmed by mass spectroscopy, producing a characteristic signal of 788.05236 m/z. 1-H NMR also produced an added dd signal at 7.66 ppm, confirming the dual attachment of the phenylbromo substitutents.

Scheme 11



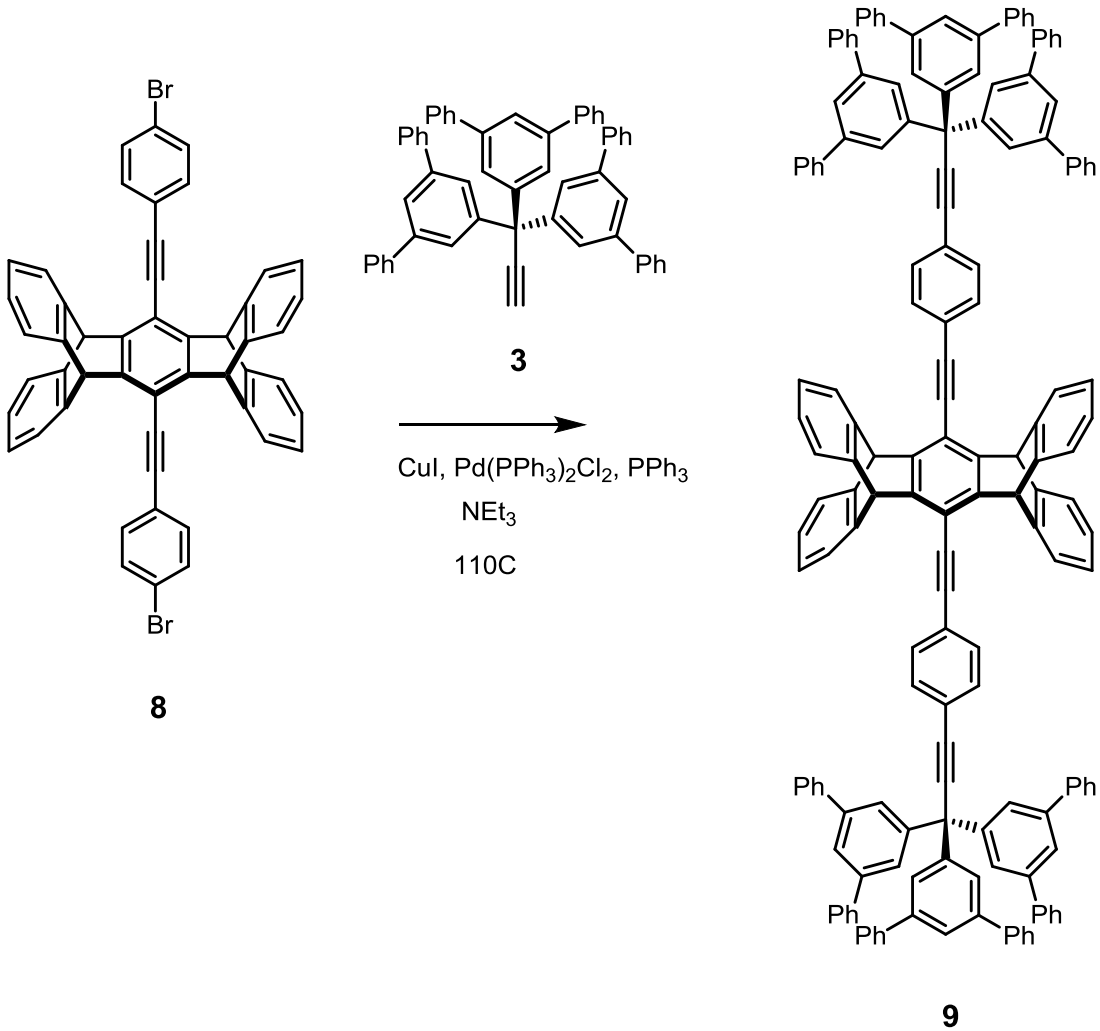
7 **8**

Compound (9)

Next the final Sonogashira coupling was performed between compound **8** and compound **3**, which successfully produced the target natural abundance rotor, compound **9**. The presence of compound **9** was clearly confirmed by proton NMR (Figure 14). The respective peaks from the meta-terphenyl species and the pentiptycene species combine together as expected in the final product. The coupling causes the loss of the alkyne protons, which are also no longer present in the spectra.

Also the two meta-terphenyl peaks at 7.73 and 7.76 ppm combine together to form one peak and the pentiptycene peak at 7.35 is eclipsed by the meta-terphenyl peak at 7.35, combing to produce the expected integration of 20 protons.

Scheme 12



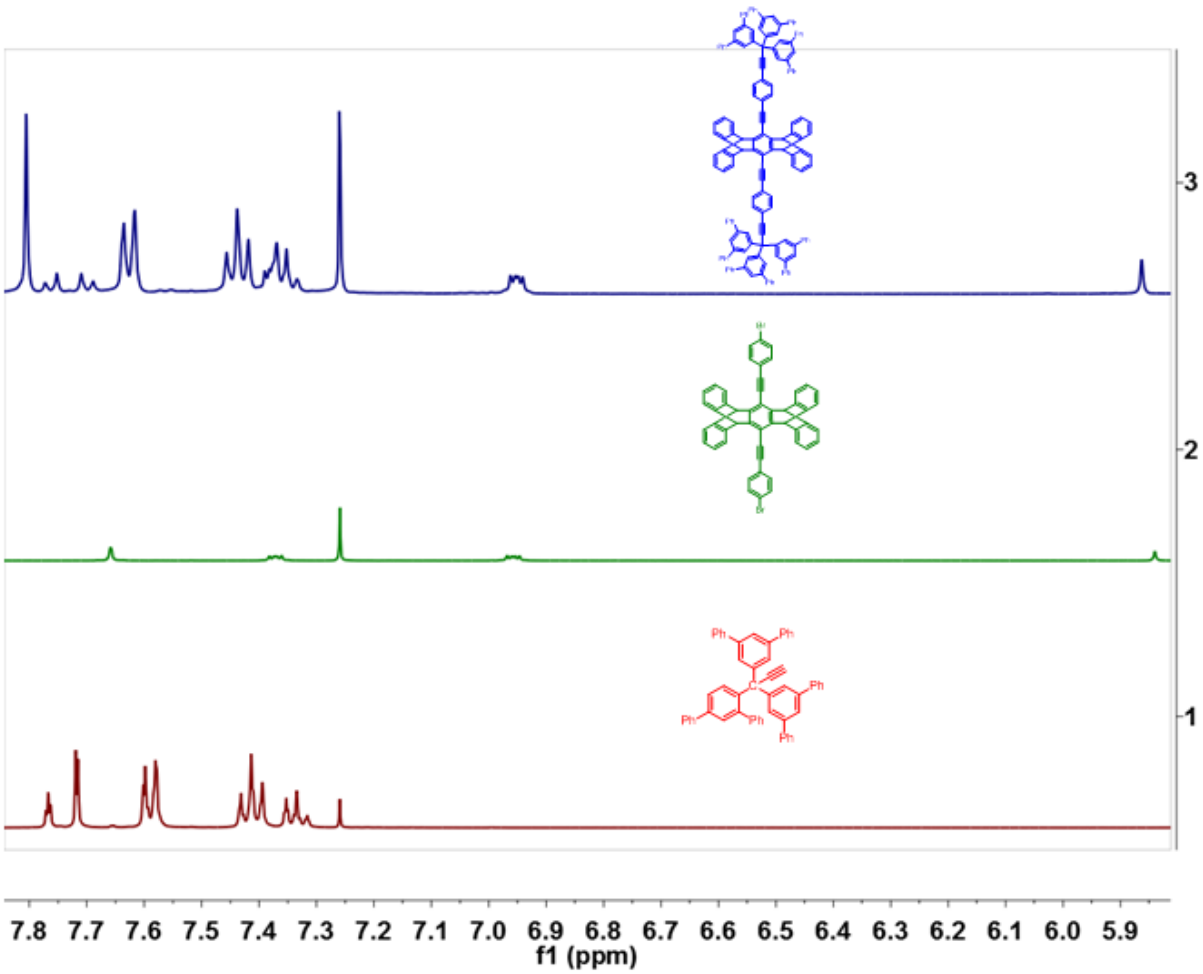


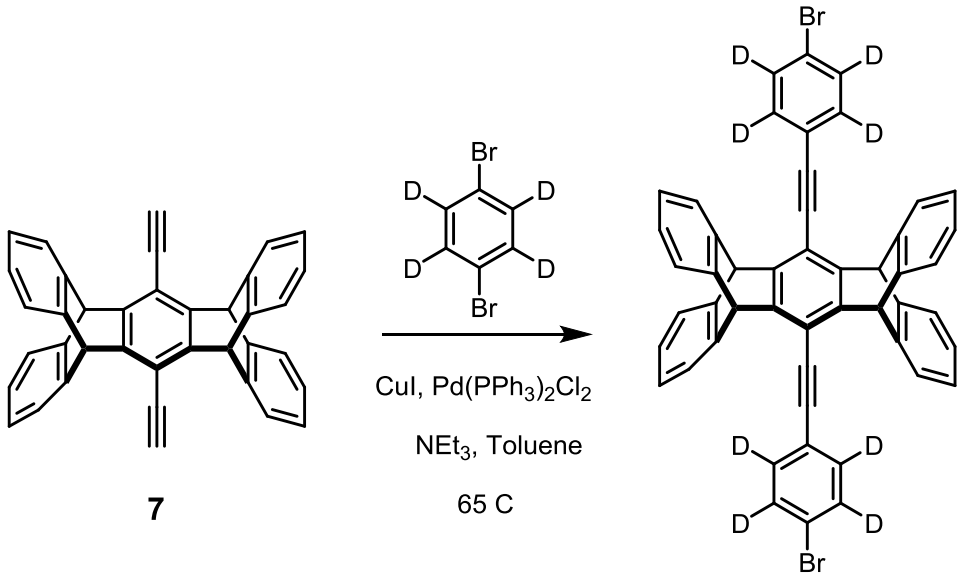
Figure 14. H^1 NMR comparison of **3**, **8**, and **9**

Compound (10)

The central stator, compound **7**, was next coupled with 1,4-dibromobenzene-D_4, using a Sonogashira coupling, which successfully formed the phenylbromo-substituted compound **10**. The presence of the compound **10** was confirmed by the absence of the dd signal at 7.66 ppm on the proton NMR spectrum, as well as the other expected

peaks. This confirmed the dual attachment of the phenylbromo substitutents, as well as the absence of the phenylene protons.

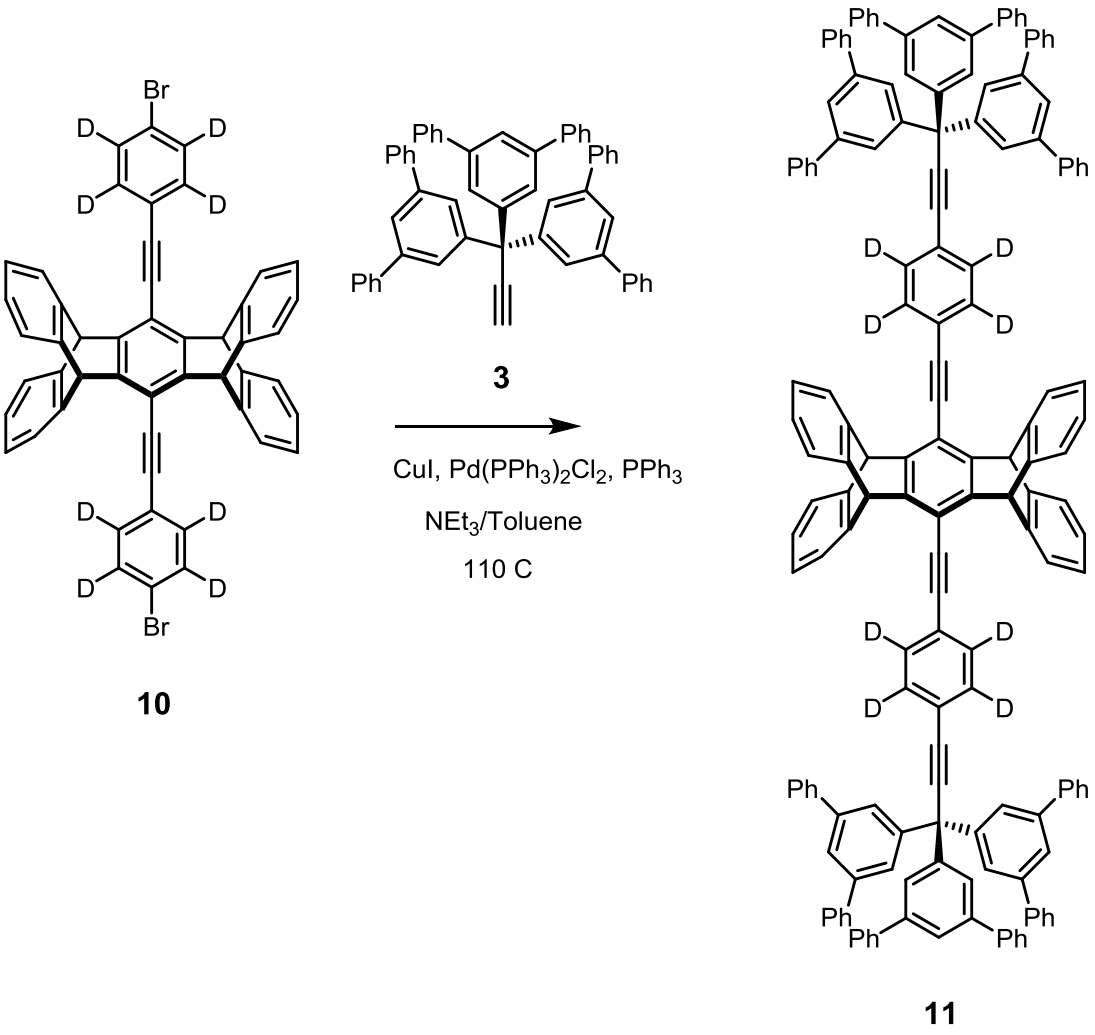
Scheme 13



Compound (11)

Next the final Sonogashira coupling was performed between compound **10** and compound **3**, which successfully produced the target D_8-rotor, compound **11**. The presence of compound **11** was clearly confirmed by proton NMR, similarly as seen in (Figure 14). The expected proton NMR peaks were present and the eight phenylene protons were absent at 7.75 ppm.

Scheme 14



Crystal Growth

With the target compound at hand, crystal growth was now the main focus. Crystal growth was attempted via slow evaporation in hexane/DCM, cyclohexane/DCM, and toluene/DCM. Similary to the single crystal flanked by triphenyl stators[9], toluene/DCM (1:5) proved to be the most reliable system to produce single crystals.

These crystals were thereater analyzed to produce the single-crystal structure (Figure 15).[16]

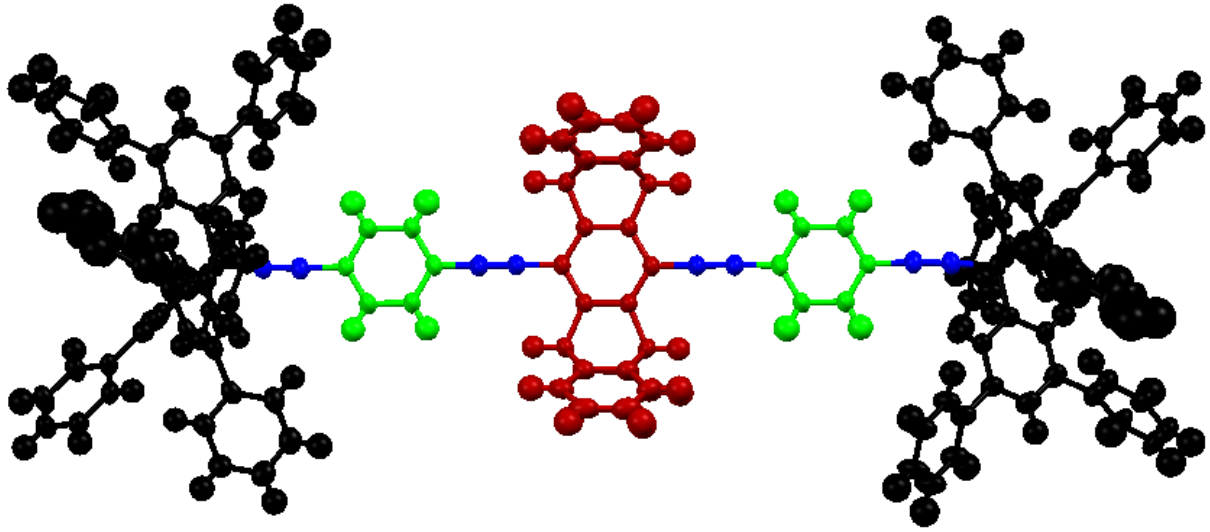


Figure 15. Single x-ray crystal structure of compound **9**

The single crystal structure (Figure 15) had many similar features to the trityl analog, most similarly the space group was also P -1. There were three toluene molecules present in the crystal per molecule of compound **9**. Also, a large amount of disorder of the central phenylene group was found within the phenylene rotors and the exterior *meta*-terphenyl phenyl rings. The disorder was found to be approximately perpendicular to the more common state, thus suggesting evidence of a possible 4-fold rotation occurring in the lattice.

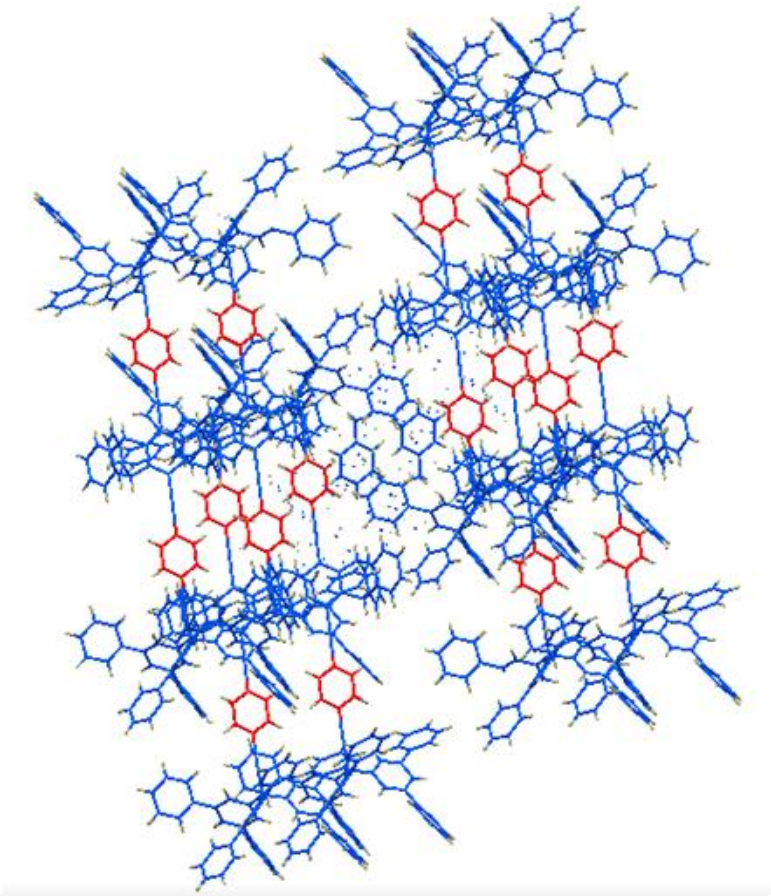


Figure 16. Crystal-packing structure of compound **9**

Within the crystal packing structure (Figure 16) there is some disorder of the meta-terphenyl system, suggesting rotation may be occurring within these exterior substituents (Figure 16). It is also evident that three solvent molecules of toluene are present per unit cell, which is comparable to results found in previously developed crystals.[17-18] It is possible that the solvent molecules near the phenylene rotor could act as a fluid, and still allow the phenylene rotor to rotate freely.

Powder X-Ray Diffraction

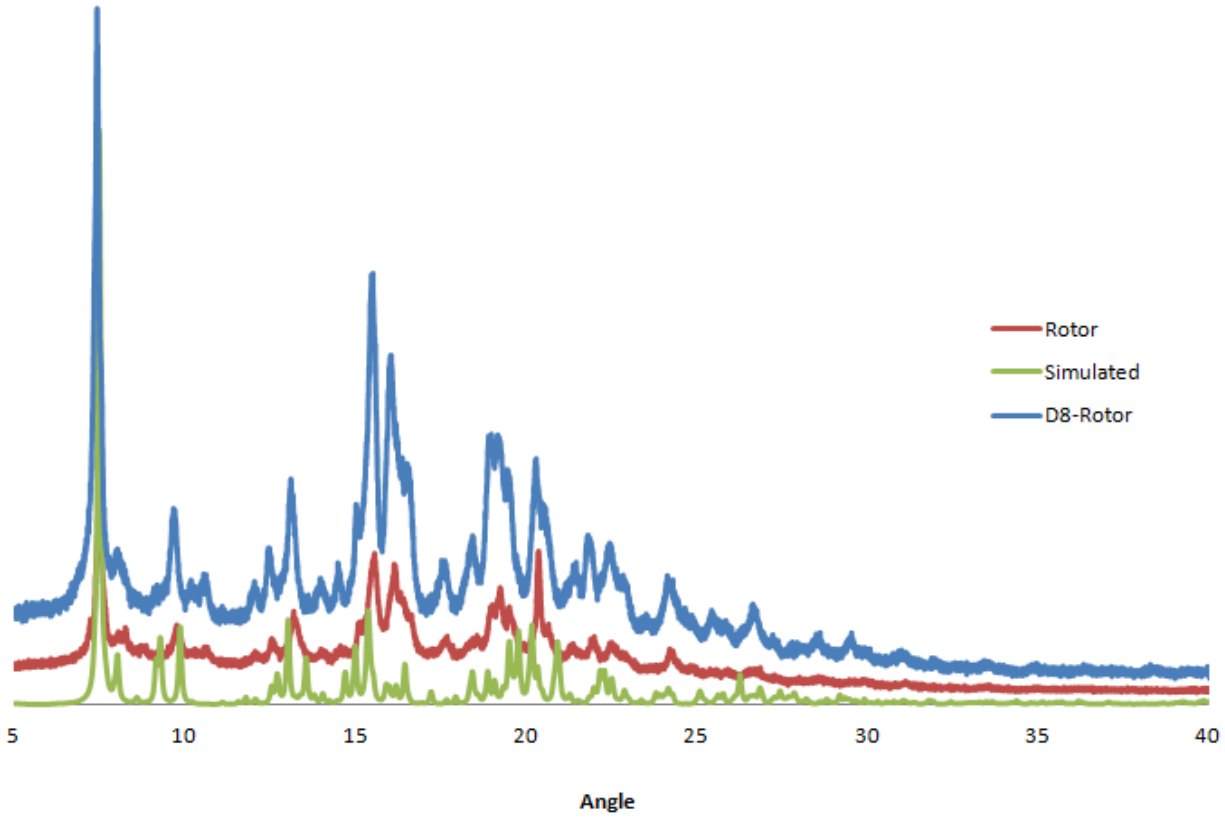


Figure 17. Powder x-ray diffraction of compound **9** and **11**

The powder x-ray diffraction pattern was determined for the natural abundance rotor **9** and the deuterated rotor **11** to confirm the replication of the previously obtained crystal structure for rotor **9**. It is evident in Figure 17 that the D8-rotor and regular rotor contained very similar diffraction peaks, although a difference of intensity existed due to the sample amount. Also these two diffraction patterns matched very closely with the simulated version, proving that the correct space group had once again been constructed.

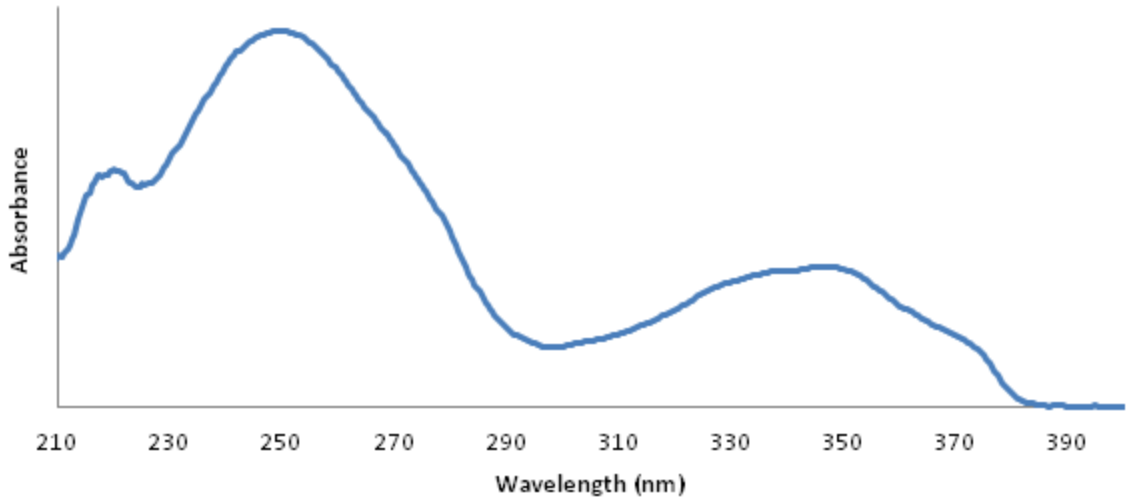


Figure 18. Absorbance spectrum of compound **9**

A qualitative absorbance spectrum was obtained by preparing a 5 microliter concentrated cyclohexane solution of the natural abundance compound **9** in cyclohexane. The spectra contained prominent peaks located at 250 and 350 nm. It is suspected that the larger peak at 250 nm is representative of the phenyl chromphores contained within the dual meta-terphenyl substituents. The farther shifted band at 350 nm was suspected to be the diphenylethylvenzene chromophore, which could be excited for fluorescent measurements.

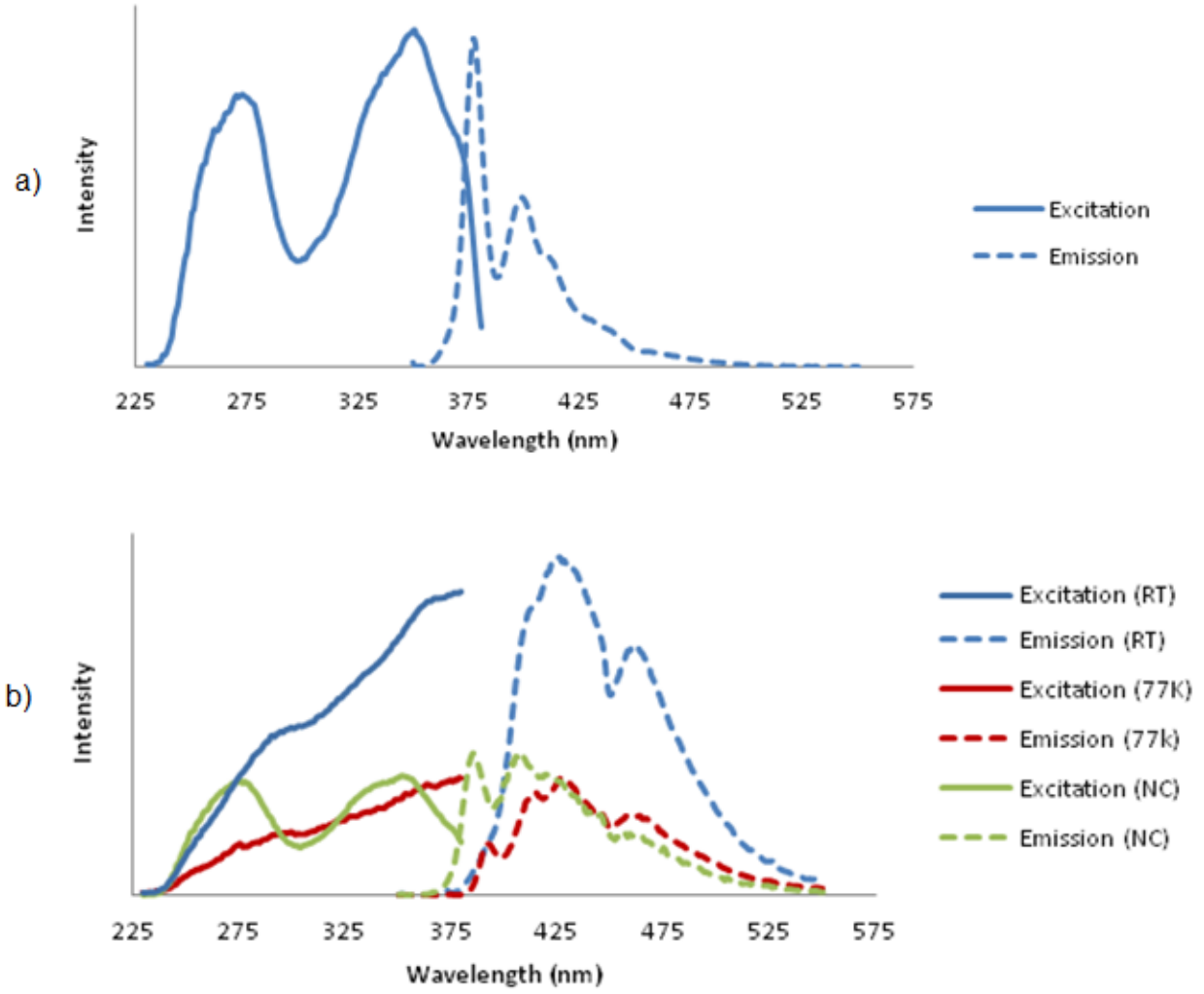


Figure 19. Fluorescence spectrum of compound **9**.

A fluorescence spectrum was obtained using a 5 micromolar cyclohexane solution of the target compound **9**. The resulting excitation and emission spectra were very comparable to the trityl derivative previously reported by Hughes et al. The emission peak ratios match almost exactly, but the excitation peak ratios are slightly different. This is most likely due to the additional phenyl groups added to the meta-terphenyl stator in comparison to the trityl, thus giving more absorbance in the phenyl band. Attempts were also made to obtain a fluorescence lifetime measurement, but the

lifetime of the fluorophore was less than a nanosecond and thus was too short to obtain a reasonable measurement.

The same measurements were also conducted using a crystal powder and nanocrystalline suspension. The nanocrystalline suspension was prepared by adding 5 microliters of a 72 micromolar solution of compound **9** in tetrahydrofuran. This solution was then added to 2 mL of a concentrated solution of cetyl trimethylammonium bromide. The nanocrystalline suspension and the crystal powder contained excitation bands very similar to the solution measurement, but a new peak was visible at 375 nm. This band was most likely representative of the disorder of the phenylene dirotors in the crystal structure, which would contribute to a loss of coplanarity within the fluorophore.[19]

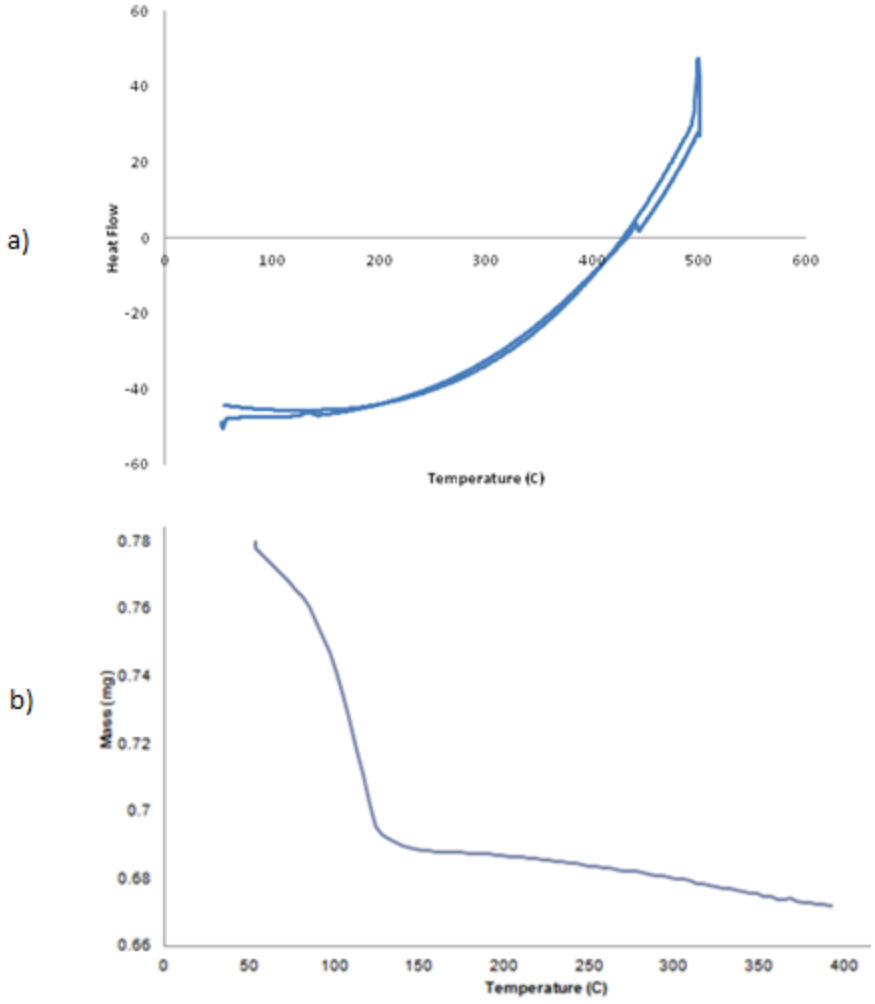


Figure 20. TGA (a) and DSC (b) of compound **9**.

Thermogravimetric analysis (TGA) and differential scanning calorimetry (DSC) were performed on the natural abundance rotor **9**. The DSC (Figure 20a) did not show any significant peaks within the trajectory, although the heat flow was representative of a slow decomposition. When the sample was removed from the holder, it was clearly charred black and thus had partially decomposed. The thermogravimetric analysis (Figure 20b)was also performed and showed a fast loss of mass up to 125 °C,

representative of the loss of toluene from the crystal lattice, and then at approximately 300 degrees a slow decomposition was once again evident.

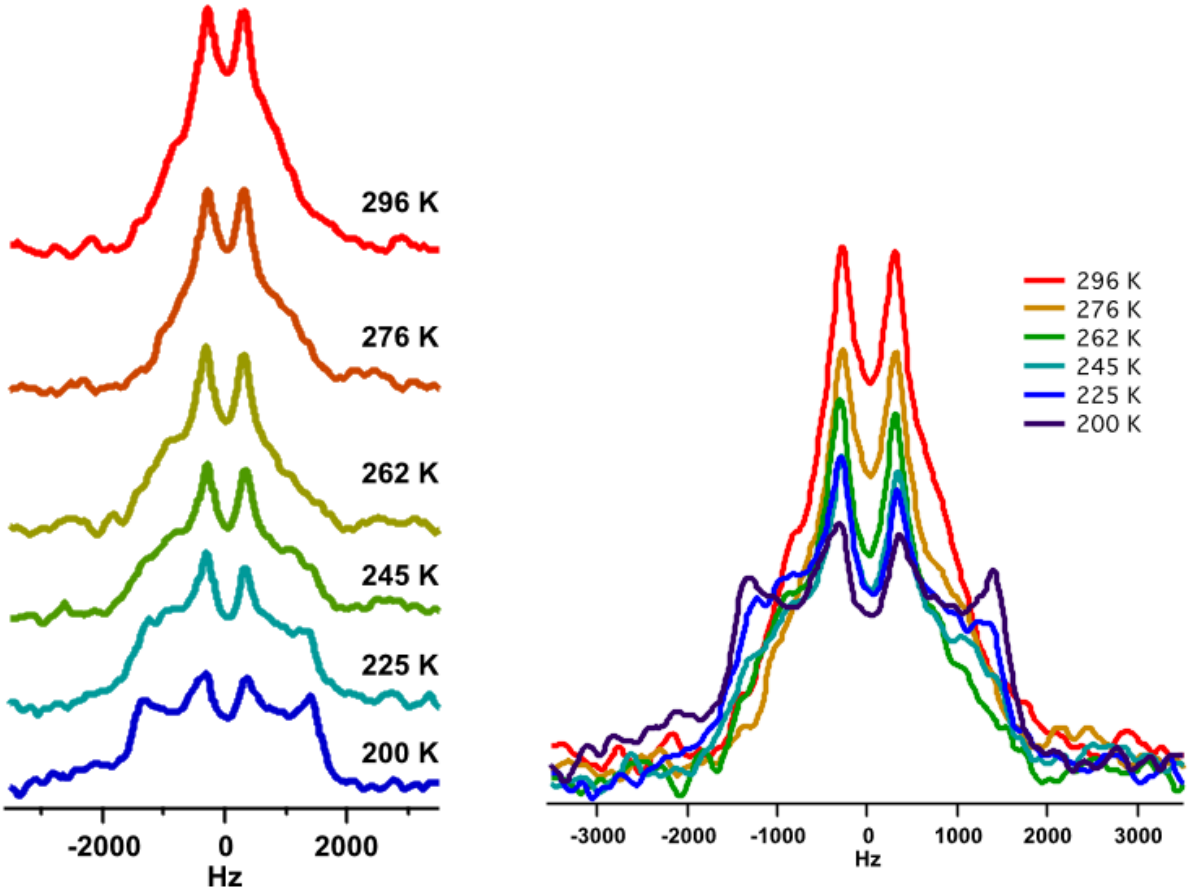


Figure 21. Solid-state NMR

Solid-state nuclear magnetic spectroscopy was utilized to carry out measurements using a quadrupolar echo pulse sequence. Static crystalline powder samples of deuterated rotor **11** were obtained at 46.07 MHz with a 90° pulse width of 2.5 microseconds, echo and refocusing delays of 50 and 42 microseconds respectively, a 5 s delay between pulses, and line broadening of 5000 Hz at temperatures ranging from 200 K to 320 K.

Attempts were made to fit experimental spectra to simulations, but a reasonable fit could not be obtained, even when a log-Gaussian distrubition model was utilized. It is very well possible that there are multiple environments within the distribution due to solvent disorder, thus making the line shape difficult to simulate. Nonetheless, the experimental line-shape patterns were representative of a transition from a fast four-fold rotation, to a slower two-fold rotation. The goal of the installed *meta*-terphenyl stator was to increase the speed of rotation towards a freely rotating phenylene ring. This could not be confirmed without successful simulations, but the line-shape patterns achieved at lower temperatures did seem promising in comparison to the trityl derivative.[20-22]

Conclusions

The proposed natural abundance molecular dirotor **9** and its respective D_8-form **11** were synthesized successfully by utilizing two successive Sonogashira reactions to complete the divergent synthesis. The yields for the final products were noticeably low, primarily due to the lacking yields of the Sonogashira steps, which were mostly attributed to reaction solubility and purification issues. The natural abundance rotor **9** was found to have two significant bands in the UV-vis band at 250 and 350 nm, which was representative of the phenyl substituents and central pentiptycene chromophores. The solid-state fluorescence showed an emergence of a new band in the emission spectra when cooled down to 77 K, most likely due to emergence of different population states of the rotating phenylene rings. The solid-state nuclear magnetic resonance spectra showed a change in the line shape when cooled from 296 K to 200 K, indicative

of a transition from a fast 4-fold rotation to an intermediate 2-fold rotation. Attempts were made to simulate each solid-state spectra, but the results were not significant.

Future Directions

With the successful synthesis of the deuterated and non-deuterated analogs of rotors **9** and **11**, the difluoro-derivatives could be synthesized as previously described in the proposal aims. This could be easily achieved by using a 1,4-dibromo-2,3-diflurobenzene to undergo two successive Sonogashira reactions, almost identical to the synthesis of **9** and **11**. After obtaining robust crystals, the fluorinated rotor could be placed within a capacitor's electric field and probed via spectroscopic techniques to determine its optoelectronic capabilities. This would have the potential to offer temporal resolution vastly superior to present liquid crystalline devices used for microelectronics.

Experimental

General. Reagents and solvents of the highest commercial purity were purchased from Fisher or Aldrich and were used as received. IR spectra were acquired on a Perkin-Elmer Paragon 1000 FT-IR instrument. The $^{1}H(^{13}C)$ NMR spectra were obtained on a Bruker NMR spectrometer operating at 400 MHz for ^{1}H using $CDCl_3$ as the solvent with TMS as internal standard.

3,5-Diphenylbromobenzene (1). A 500-mL three-neck round-bottomed flask equipped with a reflux condenser was charged with 1,3,5-tribromobenzene (10.00 g, 31.77 mmol) and tetrakistriphenylphospine palladium (0) (1.04 g, .9 mmol) under argon. A 125-mL suspension of phenylboron acid (8.40 g, 68.89 mmol) in toluene was sparged with argon for 30 min and added to the flask. A 100-mL solution of aqueous 1 M sodium carbonate was also sparged with argon and added to the flask. The mixture was stirred vigorously and set to reflux for 48 h. The mixture was washed with ethyl acetate (3x 100 mL), and the combined organic layers were dried over sodium sulfate. The solvent was removed via rotary vaporization, and the crude product was purified by column chromatography (100% hexanes) to afford 5.10 g (52% isolated yield) of **1** as a white solid. Characterization was confirmed by literature comparison[14]. Analysis: ^{1}H NMR (400 MHz, $CDCl_3$): δ 7.71 (s, 3H), 7.61 (dd, 4H, *J* = 1.5, 7.5 Hz), 7.47 (ttt, 4H, *J* = 1.5, 7.5, 7.5 Hz), 7.42 (ttt, 2H, *J* = 1.5, 7.5, 7.5 Hz). ^{13}C NMR (400 MHz, $CDCl_3$) δ 143.7, 139.8, 128.9, 128.0, 127.2, 124.9, 123.2; IR (DRIFT cm-1) 3059, 3035, 1753, 1595, 1559, 1423; MALDI-TOF MS, $C_{18}H_{13}Br$: calculated 308.01951 m/z, found 308.01908.

Tri(5'-*m*-terphenyl)methanol (2). A 250-mL three-neck round-bottom flask was charged with a magnetic stir bar and magnesium ribbon (0.65 g, 6.95 mmol) and equipped with a reflux condenser. The entire setup was flame-dried and allowed to cool under argon. A 100-mL solution of **1** (5.3 g, 13.91 mmol) was added, and the mixture was stirred at reflux until the magnesium ribbon disappeared. Diethyl carbonate (0.70 mL, mmol) was then added dropwise, and the mixture was set to reflux overnight. The reaction was quenched with saturated ammonium chloride, and the organics were extracted with diethyl ether and dried over sodium sulfate. The solvent was removed via rotary vaporization, and the crude product was purified by column chromatography (hexanes/CH_2Cl2 = 2:1) to afford 2.3 g (57% isolated yield) of **2** as a white solid. Characterization was confirmed by literature comparison.[14] Analysis: ^{1}H NMR (400 MHz, $CDCl_3$): δ 7.87 (t, 3H, *J* = 1.5 Hz), 7.72 (d, 6H, *J*= 1.5 Hz), 7.61 (dd, 12H, J = 1.50, 7.5 Hz), 7.42 (dd, 12H, *J*= 7.5, 7.5 Hz), 7.34 (tt, 6H, J = 1.0, 7.5 Hz), 3.08 (s, 1H). ^{13}C NMR (400 MHz, CDCl3) δ 147.9, 141.7, 141.2, 128.9, 127.6, 127.5, 126.0, 125.6, 82.7; IR (DRIFT cm-1) 3551, 3034, 1799, 1593, 1497, 1427; MALDI-TOF MS, $C_{55}H_{44}O$: calculated for 720.33867 m/z, found 720.18215.

3,3,3-Tri(5'-*m*-terphenyl)propyne (3). A dry 500-mL round-bottom flask was charged with a magnetic stir bar and **2** (1,25 g, 1.21 mmol) and equipped with a reflux condenser. Acetyl chloride (15 mL) was added, and the mixture was set to reflux for 60 min. Excess acetyl chloride was removed via rotary vaporization, and the residue was taken up in 30 mL of dry toluene. The solvent was removed again, and 100 mL of dry toluene was added. The solution was allowed to stir for 15 min before a 0.5 M solution of ethynylmagnesium bromide in THF (9.3 mL, 1.21 mmol) was added. The mixture was

set to reflux for 4 hr and was quenched with saturated ammonium chloride, and the organics were extracted with diethyl ether and dried over sodium sulfate. The solvent was removed via rotary vaporization and the crude product was purified by column chromatography (1 L of 100% hexanes followed by 1 L of 9:1 hexanes/diethyl ether) to afford 800 mg (65% recovered yield) of **3** as a white solid. Characterization was confirmed by literature comparison.[14] Analysis: ^{1}H NMR (400 MHz, $CDCl_3$) δ7.77 (t, 4H, J = 1.5 Hz), 7.72 (d, 4H, *J* = 1.5 Hz), 7.42 (dd, 12H, *J* = 1.0, 7.0 Hz), 7.33 (ddd, 12H, *J* = 1.0, 7.5, 7.5 Hz), 7.36 (t, 6H, *J* = 7.5 Hz), 2.89 (s, 2H). ^{13}C NMR (400 MHz, $CDCl_3$) δ 145.7, 141.7, 141.2, 128.9, 127.6, 127.5, 127.2, 125.3, 89.7, 74.8, 56.3; IR (DRIFT cm-1) 3285, 3033, 1591, 1497, 1411; MALDI-TOF MS, $C_{57}H_{40}$: calculated for 724.31245 m/z, found 724.31079.

5,6,7,12,13,14-Hexahydro-5,14:7,12-bis(o-benzeno)pentacene-6,13-dione (4). A 500-mL round-bottom flask was charged with a stir bar, anthracene (10.00 g, 56.11 mmol), p-chloranil (13.15 g, 53.48 mmol), and 1,4-benzoquinone (2.90 g, 26.83 mmol) in acetic acid (120 mL). The mixture was refluxed for 24 h. The resulting mixture was cooled to room temperature, filtered, washed with a saturated sodium bicarbonate solution, extracted with ether, dried with sodium sulfate, and rotary vaporized to produce the crude product. Column chromatography using 4:1 Hexanes:DCM was able to afford 5.50 g(42.57% recovered yield) of **4** as a yellow-orange solid. Characterization was confirmed by literature comparison.[15] Analysis: ^{1}H NMR (400 MHz, $CDCl_3$): δ7.36 (m, 8H), 6.98 (m, 8H), 5.75 (s, 4H). ^{13}C NMR (400 MHz, $CDCl_3$) δ 179.9, 150.9, 143.7, 125.5, 124.3, 47.4; IR (DRIFT cm-1) 3064, 1640, 1595, 1458; MALDI-TOF MS, $C_{34}H_{20}O_2$: calculated for 460.14578 m/z, found 460.14693.

6,13-bis((trimethylsilyl)ethynyl)-5,6,7,12,13,14-hexahydro-5,14:7,12-bis([1,2]benzene)pentacene-6,13-diol (5). A 100-mL round-bottom flask was charged with a stir bar, THF (60 mL), and trimethylsilyl acetylene (5.00 mL, 14.76 mmol) at 0 C, and thereafter 1.6M n-BuLi in hexane (19 mL) was added dropwise. The TMSLi mixture was then kept at 0 C for another 1 h before it was added to a solution of compound **4** (2.00 g, 1.78 mmol) in THF. The mixture was left to warm to room temperature and stirred overnight. The reaction was quenched with saturated ammonium chloride and extracted with ether. The solvent removed via rotary vaporization, and the crude product was purified by column chromatography by using 3:1 hexanes:DCM to elute the impurities, followed by 1:1 hexanes:DCM to afford 2.96 g (68% isolated yield) of **5** as an off-white solid. Characterization was confirmed by literature comparison.[15] Analysis: ^{1}H NMR (400 MHz, $CDCl_3$): δ7.32 (dd, 8H, *J* = 3.2, 5.3 Hz), 6.93 (dd, 8H, *J* = 3.2, 5.3 Hz), 5.77 (s, 4H), 1.64 (s, 2H), 0.48 (s, 18H). ^{13}C NMR (400 MHz, $CDCl_3$) δ144.8, 143.9, 125.1, 123.6, 102.4, 100.5, 52.1, 0.2; IR (DRIFT cm-1) 3493, 3018, 2167, 1457; MALDI-TOF MS, $C_{44}H_{40}O_2Si_2$: calculated for 656.25613 m/z, found 656.25399.

6,13-bis((trimethylsilyl)ethynyl)-5,7,12,14-tetrahydro-5,14:7,12-bis([1,2])benzene)pentacene (6).A 250-mL round-bottom flask was charged with a magnetic stir bar, compound **5**(0.82 g, 1.25 mmol) and acetone (60 mL). A solution of tin(II) chloride dehydrate(0.766 g, 4.04 mmol) in 50% acetic acid (20 mL) was added dropwise. The mixture was stirred at room temperature for 24 h and the product was filtered to afford 0.65 g of **6** as an off-yellow solid (83.60% isolated yield). Analysis: ^{1}H NMR (400 MHz, $CDCl_3$): δ7.34 (m, 8H), 6.95 (m, 8H), 5.78 (s, 4H), 0.49 (s, 18H). ^{13}C

NMR (400 MHz, $CDCl_3$) δ144.8, 143.9, 125.1, 123.6, 102.4, 100.5, 52.1, 0.2; IR (DRIFT cm-1) 3022, 2956, 2155, 1456;

6,13-diethynyl-5,7,12,14-tetrahydro-5,14:7,12-bis([1.2]benzene)pentacene (7). A 100-mL round-bottom flask was charged with compound **6** (0.65 g, 1.04 mmol) and dissolved in a 1:1:1 mixture of 50 mL of H2O, THF, and methanol. A pellet of potassium hydroxide was added, and the mixture was stirred at room temperature for 5 h. The resulting product was filtered, washed with water and dried in vacuo to afford 0.30 g (60.08% isolated yield) of **7** as a white solid. Characterization was confirmed by literature comparison.[15] Analysis: ^{1}H NMR (400 MHz, $CDCl_3$): δ1.86 (s, 2H), 5.82 (s, 4H), 6.94 (dd, 8H), 7.35 (dt, 8H). ^{13}C NMR (400 MHz, $CDCl_3$) δ51.24, 51.98, 94.92, 114.13, 123.83, 125.32, 143.2, 144.6; IR (DRIFT cm-1) 3302, 2977, 1458;

Bis(p-2-(4-bromophenyl)ethynylene pentiptycene (8). A 100-mL three-neck round-bottom flask was charged with a magnetic stir bar, **7** (0.20 g, 0.418 mmol), 1.4,-iodobromobenzene (0.295 g, 1.04 mmol), toluene (30 mL), and triethylamine (15 mL). The mixture was sparged with argon for 30 min. Bis(triphenylphosphine) palladium chloride (0.035 g, .0495 mmol) and copper(I) iodide (0.017g, .088 mmol) were added, and the mixture was stirred at room temperature for 24 h under argon. The reaction was washed with saturated ammonium chloride, organics extracted with dichloromethane, and dried over sodium sulfate. The crude product was rotary vaporized and purified by column chromatography (hexanes/DCM = 4:1) to afford 80 mg (24.28% recovered yield) of **8** as a white solid. Analysis: ^{1}H NMR (400 MHz, $CDCl_3$) δ7.66 (dd, 8H), 7.37 (dd, 8H), 6.96 (dd, 8H), 5.84 (dd, 4H); IR (DRIFT cm-1) 3018, 1457, 1383; MALDI-TOF MS, $C_{55}H_{44}O$: calculated for 788.05318m/z, found 788.05236.

Bis(p-2-(4-3,3,3-Tri(5'-*m*-terphenyl)propynyl)-p-phenylene)ethynylene pentiptycene (9). A 100-mL three-neck round-bottom flask was charged with a magnetic stir bar, **8**(60 mg, 76.09 mmol), **7** (120 mg g, 165.53 mmol), toluene (20 mL), and triiethylamine (10 mL). The mixture was sparged with argon for 30 min. Bis(triphenylphosphine) palladium chloride (20 mg, .028 mmol), copper(I) iodide (10 mg, 0.052 mmol), and triphenylphosphine (5 mg, .019 mmol) were added, and the mixture was set to reflux for 24 h. The reaction vessel was opened and then **7** (60 mg, 82.75 mmol), Bis(triphenylphosphine) palladium chloride (20 mg, .028 mmol), and triphenylphosphine (5 mg, .019 mmol) were added again, the vessel was sealed while under argon, and set to reflux for 24 h. The reaction was washed with saturated ammonium chloride, organics extracted with dichloromethane, and dried over sodium sulfate. The crude product was rotary vaporized and purified by column chromatography (hexanes/DCM = 3:1). The isolated compound was then dissolved in a minimal amount of DCM and precipitated out with hexanes to afford 22 mg (13.9% yield) of compound **9**. Analysis: ^{1}H NMR (400 MHz, $CDCl_3$) δ7.82 (s, 14H), 7.75 (dd, 8H), 7.6 (m, 24H), 7.45 (m, 24H), 7.25 (m, 20H), 6.95 (dd, 8H), 5.85 (s, 4H). ^{13}C NMR (400 MHz, $CDCl_3$) δ145.04, 144.05, 141.07, 141.72, 144.73, 128.87, 125.33, 127.36, 30.93; IR (DRIFT cm-1) 3018, 1457, 1383

Bis(p-2-(4-bromophenyl)ethynylene pentiptycene (10). A 100-mL three-neck round-bottom flask was charged with a magnetic stir bar, **7** (100 mg, 0.209 mmol), D4-1.4,-bromobenzene (125 mg, 0.522 mmol), toluene (20 mL), and triethylamine (10 mL). The mixture was sparged with argon for 30 min. Bis(triphenylphosphine) palladium chloride (0.035 g, .0495 mmol) and copper(I) iodide (0.017g, .088 mmol) were added, and the

mixture was set to reflux for 24 h. The reaction was washed with saturated ammonium chloride, organics extracted with dichloromethane, and dried over sodium sulfate. The crude product was rotary vaporized and purified by column chromatography (hexanes/DCM = 4:1) to afford 34 mg (20.43% recovered yield) of **10** as a white solid. Analysis: ^{1}H NMR (400 MHz, $CDCl_3$) δ7.37 (dd, 8H), 6.96 (dd, 8H), 5.84 (dd, 4H); IR (DRIFT cm-1) 3034, 1591, 1497.

Bis(p-2-(4-3,3,3- Tri(5'-*m*-terphenyl)propynyl)-p-phenylene)ethynylene pentiptycene (11). A 100-mL three-neck round-bottom flask was charged with a magnetic stir bar, **10** (34 mg, 0.0427 mmol), **7** (70 mg, .096 mmol), toluene (10 mL), and triethylamine (5 mL). The mixture was sparged with argon for 30 min. Bis(triphenylphosphine) palladium chloride (0.0178 g, .0252 mmol), copper(I) iodide (0.0091 g, 0.0471 mmol) and triphenylphosphine (5 mg, .019 mmol) were added, and the mixture was set to reflux for 24 h. The reaction vessel was opened and then **7** (35 mg, .048 mmol), Bis(triphenylphosphine) palladium chloride (0.0178 g, .0252 mmol), and triphenylphosphine (5 mg, .019 mmol) were added again, the vessel was sealed while under argon, and set to reflux for 24 h. The reaction mixture was washed with saturated ammonium chloride, organics extracted with dichloromethane, and dried over sodium sulfate. The crude product was rotary vaporized and purified by column chromatography (hexanes/DCM = 3:1). The isolated compound was then dissolved in a minimal amount of DCM and precipitated out with hexanes to afford 16 mg (17.98% recovered yield) of **11** as a white solid. Analysis: ^{1}H NMR (400 MHz, $CDCl_3$) δ7.82 (s, 14H), 7.6 (m, 24H), 7.45 (m, 24H), 7.25 (m, 20H), 6.95 (dd, 8H), 5.85 (s, 4H). ^{13}C NMR

(400 MHz, $CDCl_3$) δ145.05, 144.11, 141.10, 141.74, 144.81, 128.87, 125.33, 127.36, 53.33; IR (DRIFT cm-1) 3032, 2920, 11591, 1496, 1412.

Crystal growth of (9) and (11). In a vial, the white powder, **9** or **11**, was dissolved in a minimal amount of DCM and then 20% of the DCM's volume was added in toluene to produce a 5:1 DCM:Toluene solution. The vial was covered with parafilm and vented with a small hole produced by a syringe needle. The solution was allowed to sit undisturbed for 2 days and eventually producing square-shaped crystals.

Appendix

Table of Spectra

Figure 1: Infrared spectrum of **1** ……..51

Figure 2: Mass spectrum of **1**……..……52

Figure 3: Proton NMR of **1**……53

Figure 4: Carbon NMR of **1**……..……54

Figure 5: Infrared spectrum of **2**……..……55

Figure 6: Mass spectrum of **2**……..……56

Figure 7: Proton NMR of **2**……57

Figure 8: Carbon NMR of **2**……..……58

Figure 9: Infrared spectrum of **3**……..……59

Figure 10: Mass spectrum of **3**……..……60

Figure 11: Proton NMR of **3**……..……61

Figure 12: Carbon NMR of **3**……..……62

Figure 13: Infrared spectrum of **4**……..…63

Figure 14: Mass spectrum of **4**……..……64

Figure 15: Proton NMR of **4**……..……65

Figure 16: Carbon NMR of **4**……..……66

Figure 17: Infrared spectrum of **5**……..……67

Figure 18: Mass spectrum of **5**……..……68

Figure 19: Proton NMR of **5**……..……69

Figure 20: Carbon NMR of **5**……..……70

Figure 21: Infrared spectrum of **6**……71

Figure 22: Mass spectrum of **6**……72

Figure 23: Proton NMR of **6**……73

Figure 24: Carbon NMR of **6**……74

Figure 25: Infrared spectrum of **7**……75

Figure 26: Mass spectrum of **7**……76

Figure 27: Proton NMR of **7**……77

Figure 28: Carbon NMR of **7**……78

Figure 29: Infrared spectrum of **8**……79

Figure 30: Mass spectrum of **8**……80

Figure 31: Proton NMR of **8**……81

Figure 32: Infrared spectrum of **9**……82

Figure 33: Proton NMR of **9**……83

Figure 34: Carbon NMR of **9**……84

Figure 35: Infrared spectrum of **10**……85

Figure 36: Proton NMR of **10**……86

Figure 37: Infrared spectrum of **11**……87

Figure 38: Proton NMR of **11**……88

Figure 39: Carbon NMR of **11**……89

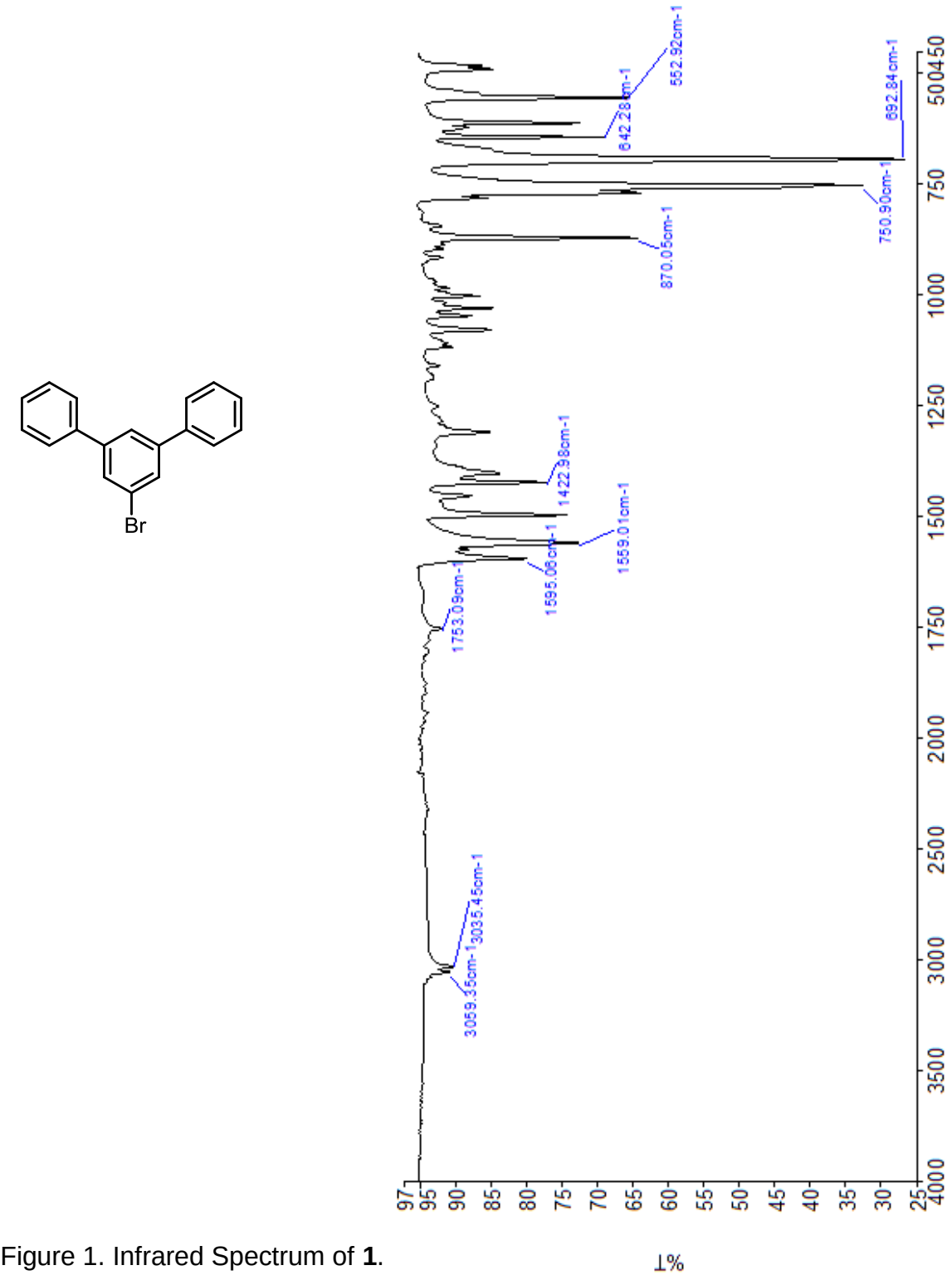


Figure 1. Infrared Spectrum of **1**.

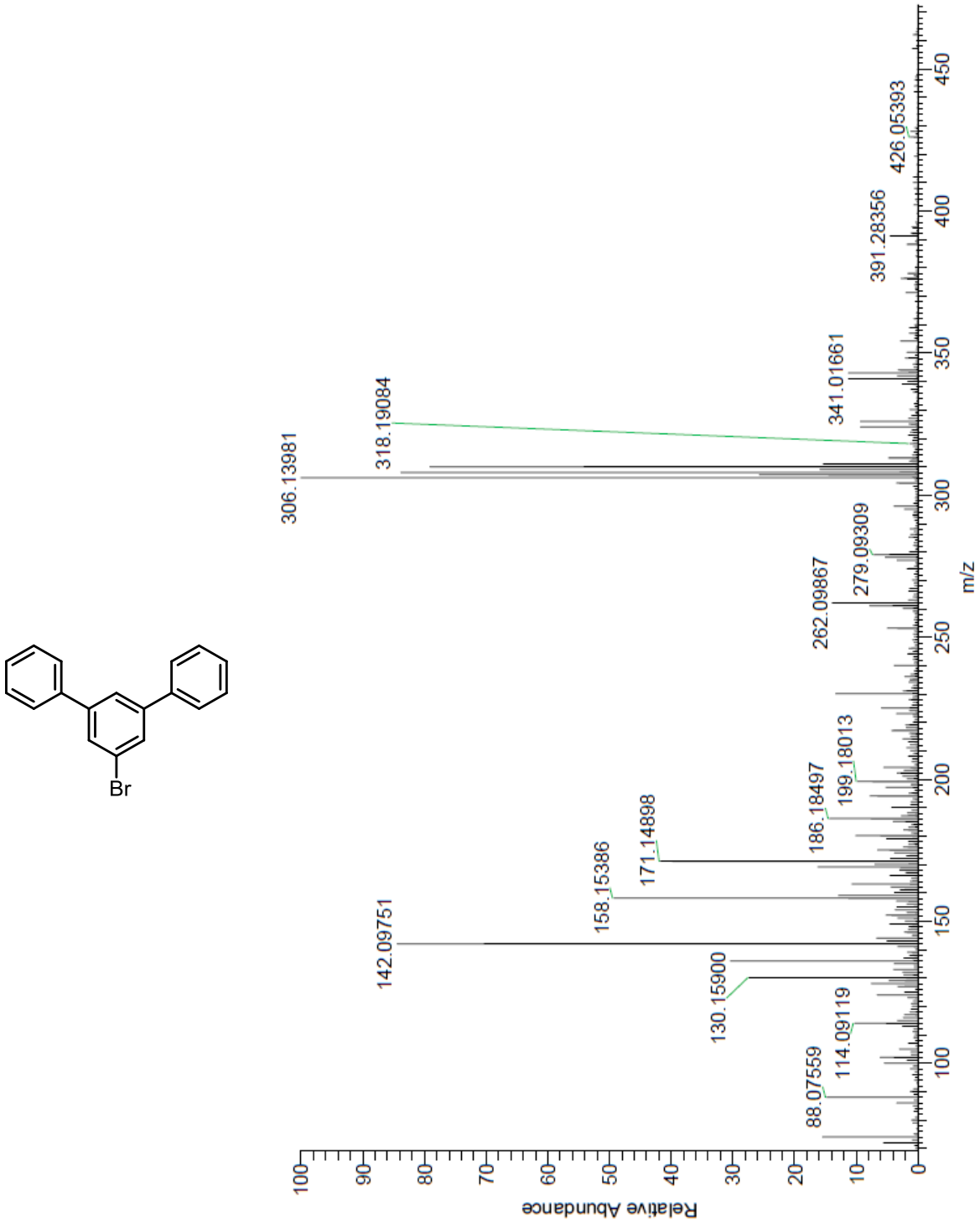


Figure 2. Mass Spectrum of **1**.

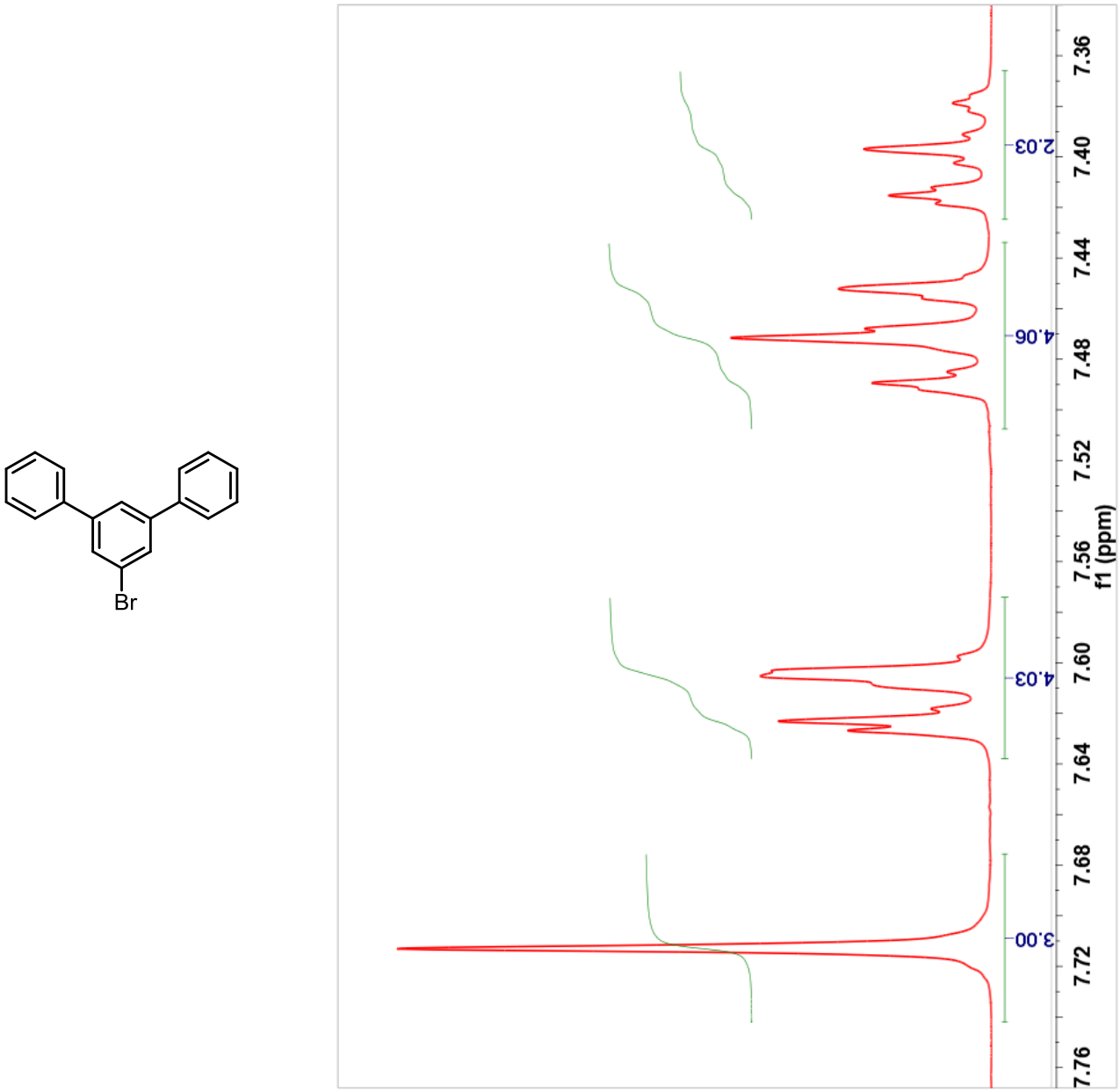


Figure 3. Proton NMR of **1**.

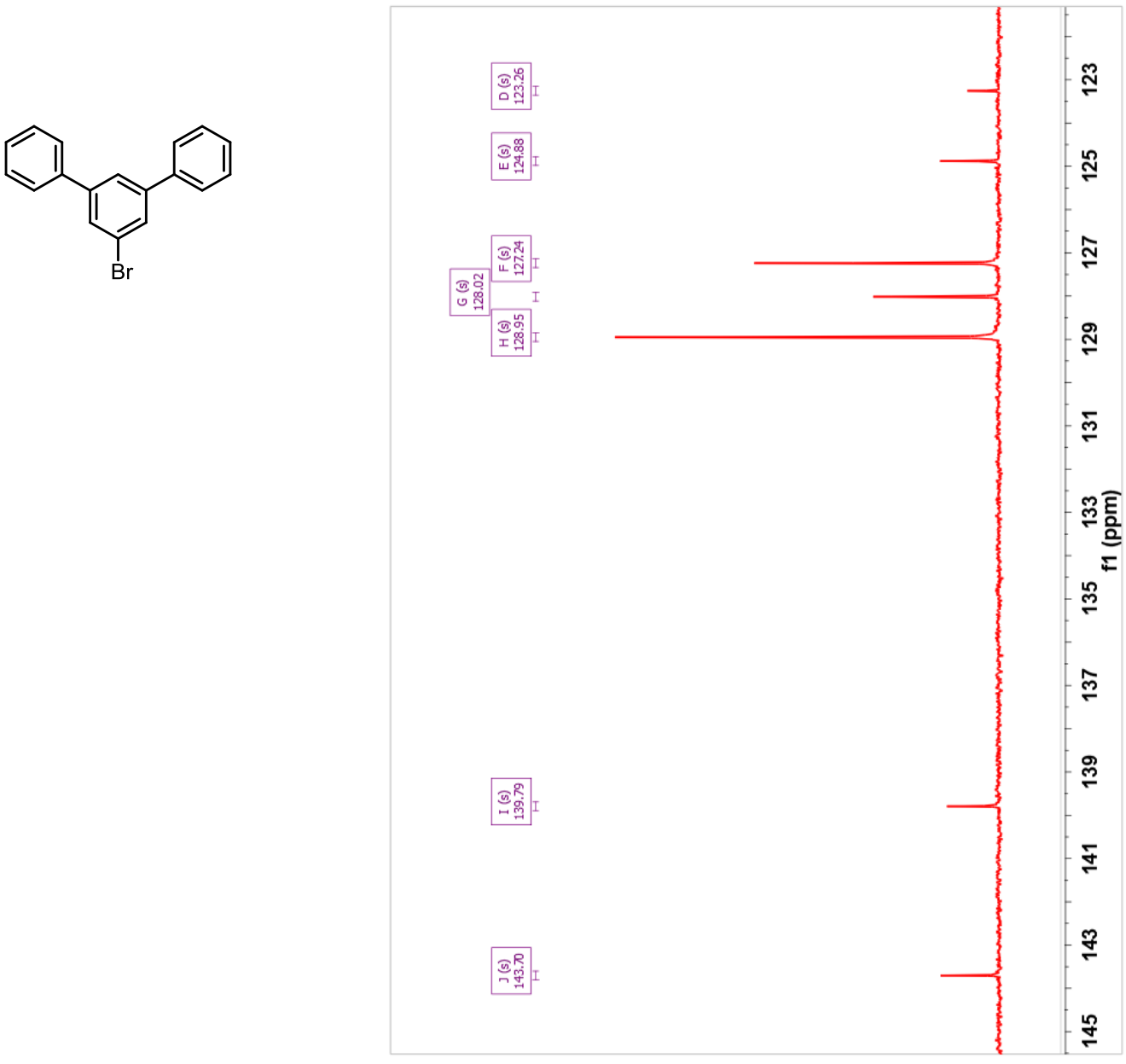


Figure 4. Carbon NMR of **1**.

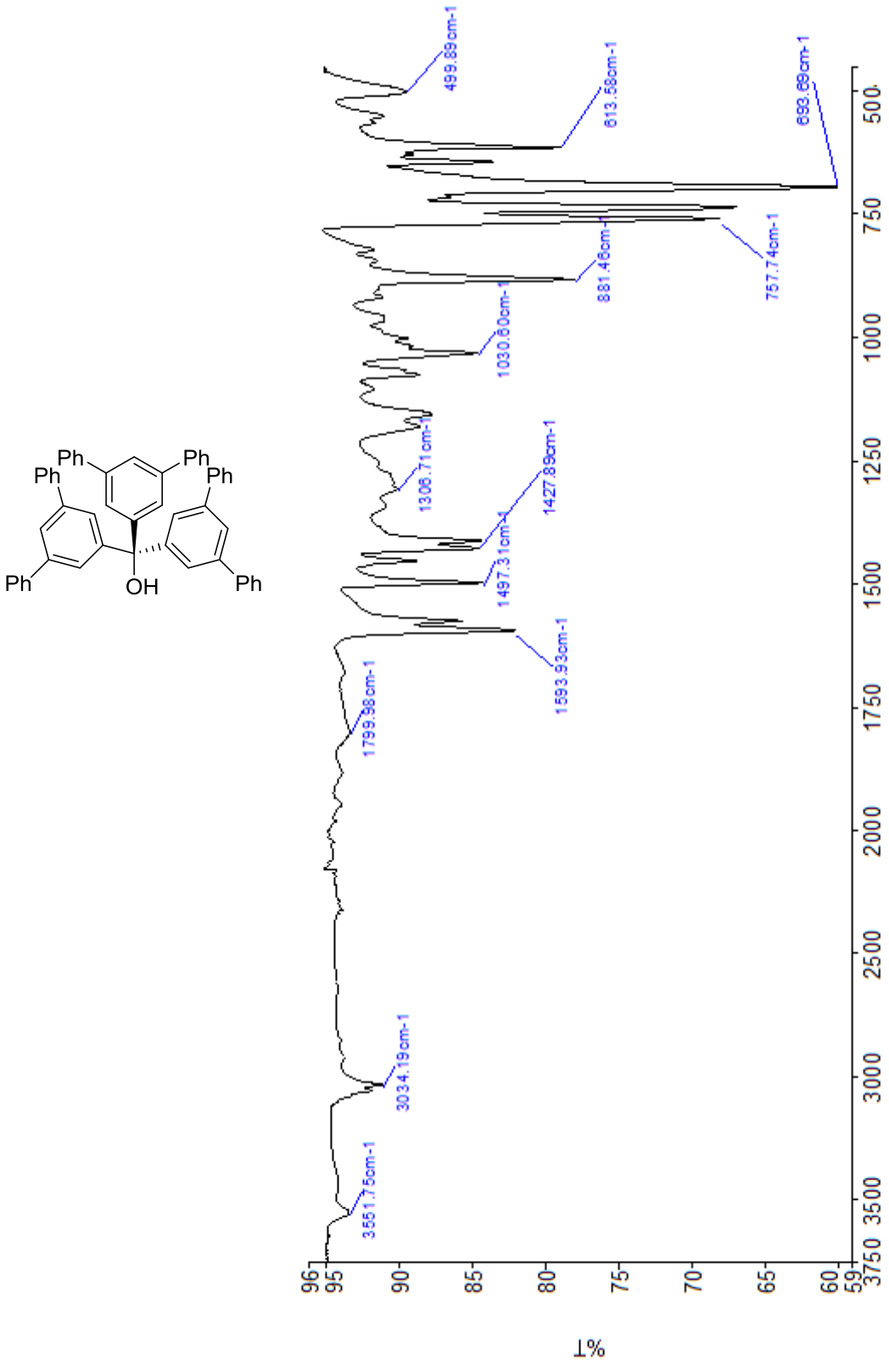


Figure 5. Infrared Spectrum of **2**.

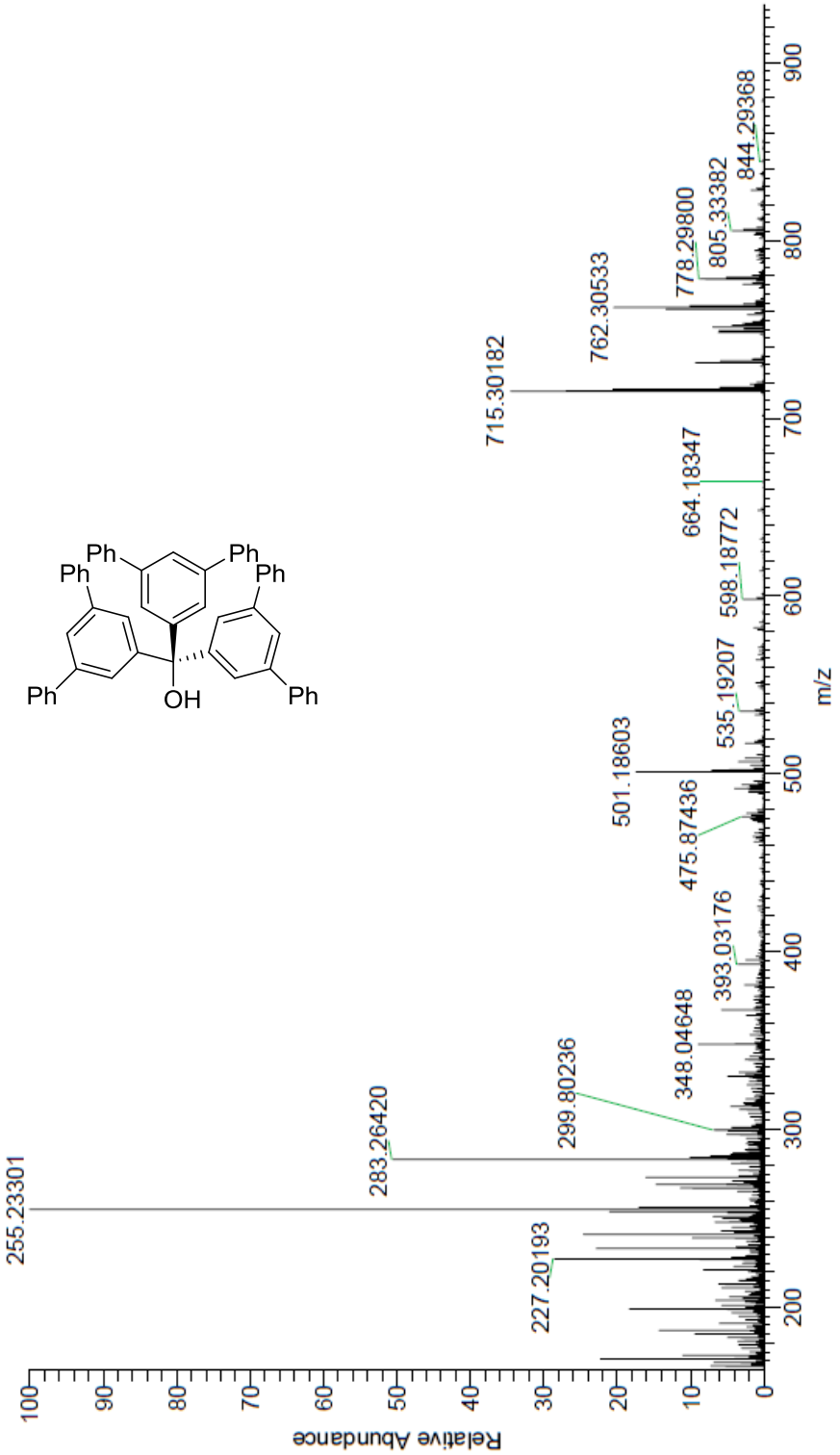


Figure 6. Mass spectrum of **2**.

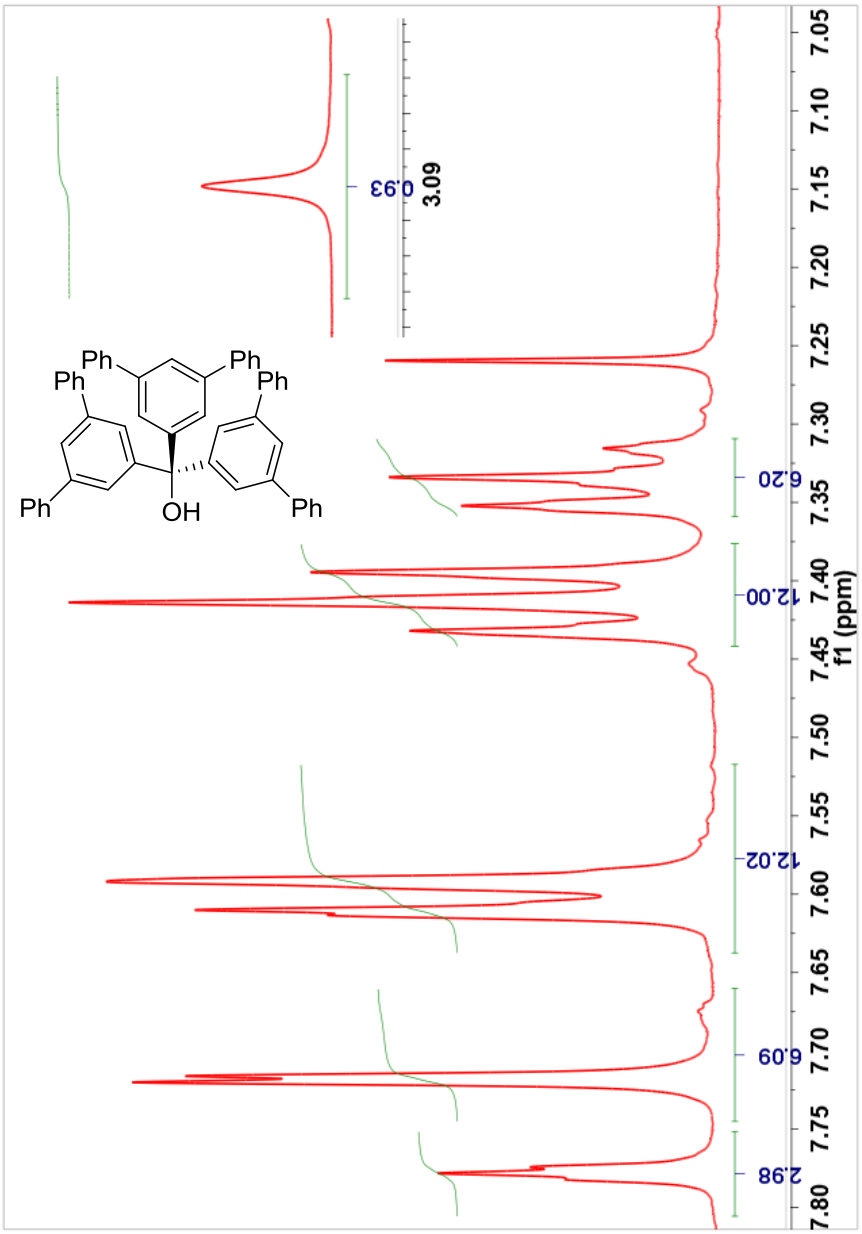


Figure 7. Proton NMR of **2**.

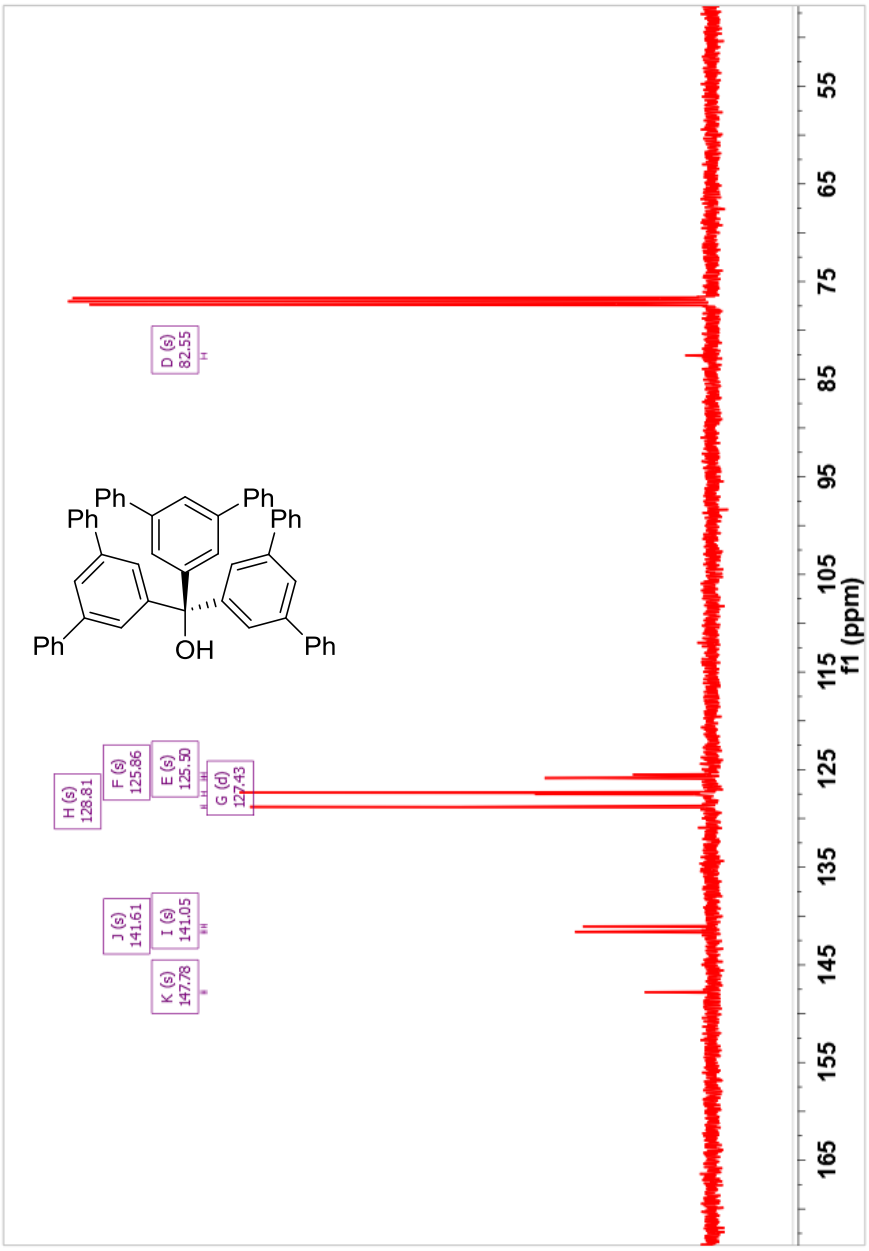


Figure 8. Carbon NMR of **2**.

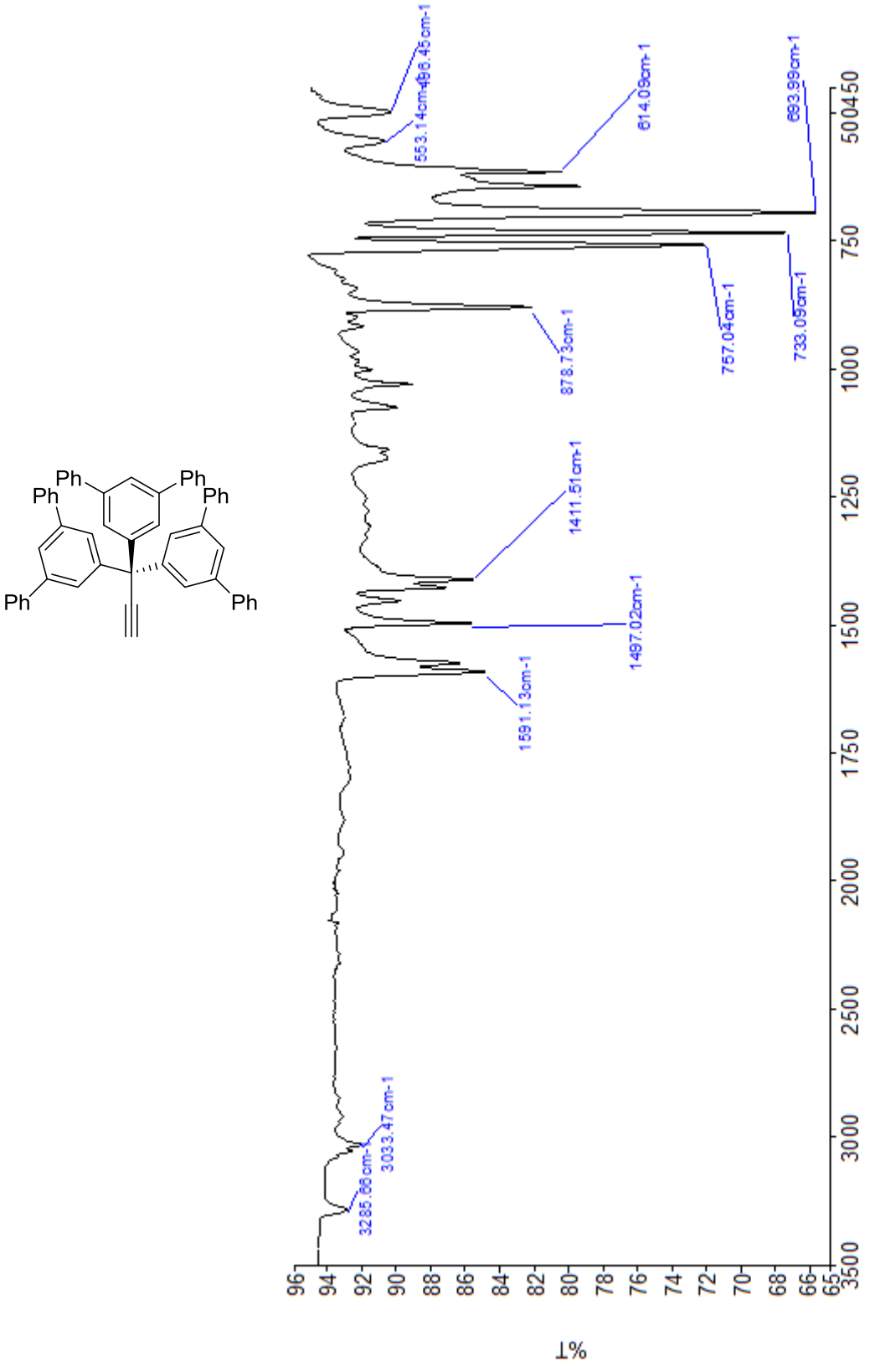


Figure 9. Infrared spectrum of **3**.

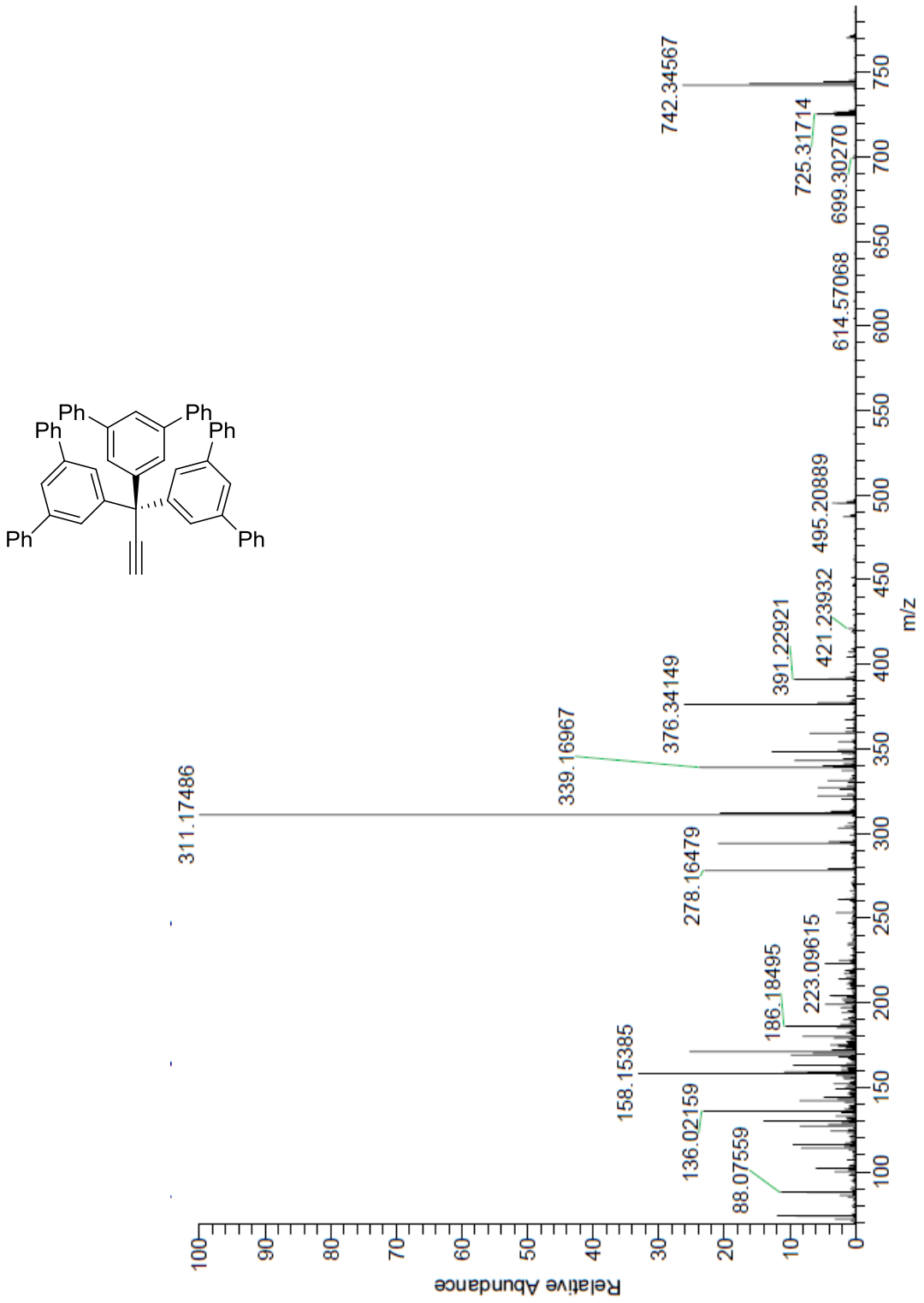


Figure 10. Mass spectrum of **3**.

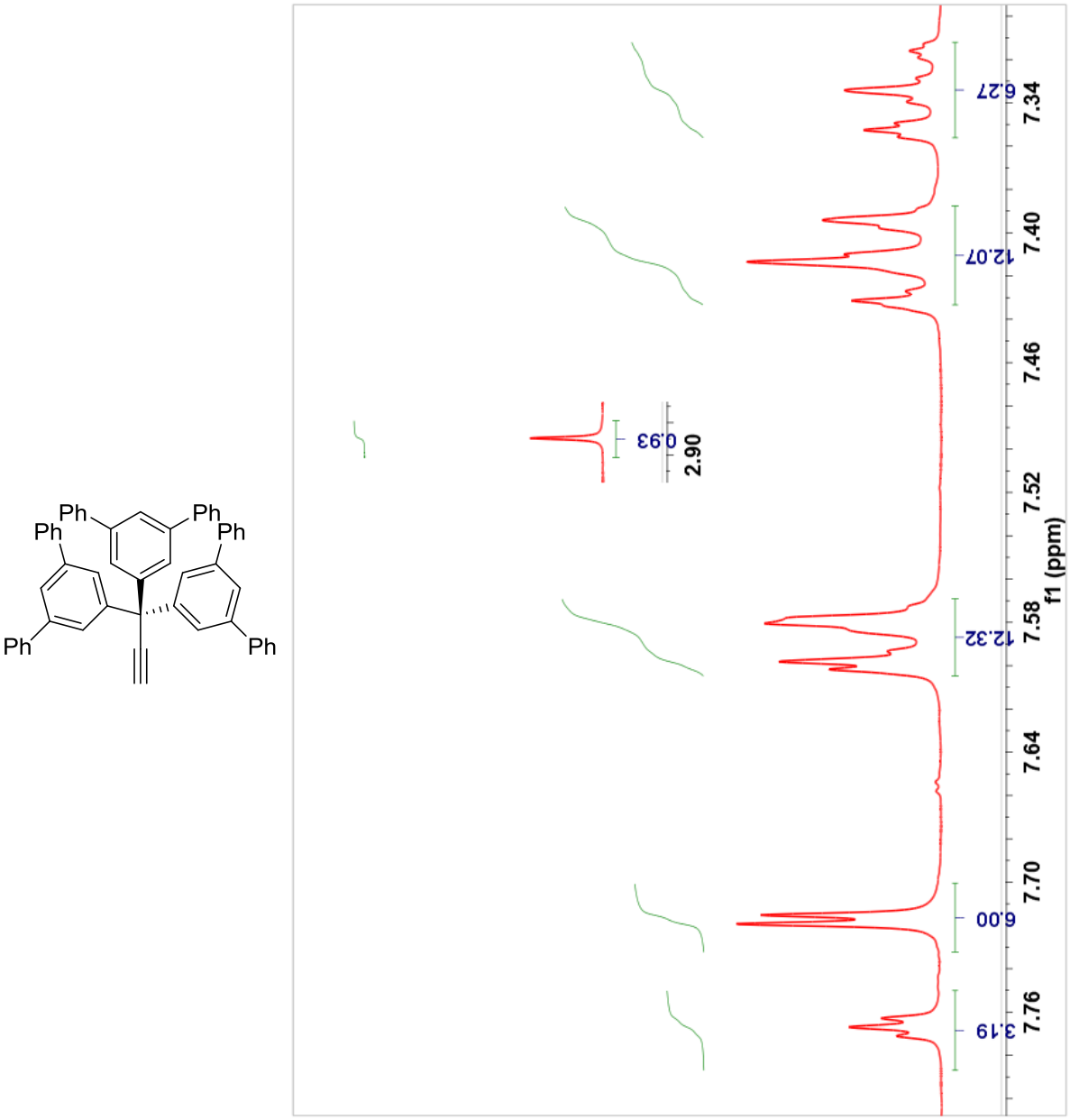


Figure 11. Proton NMR of **3**.

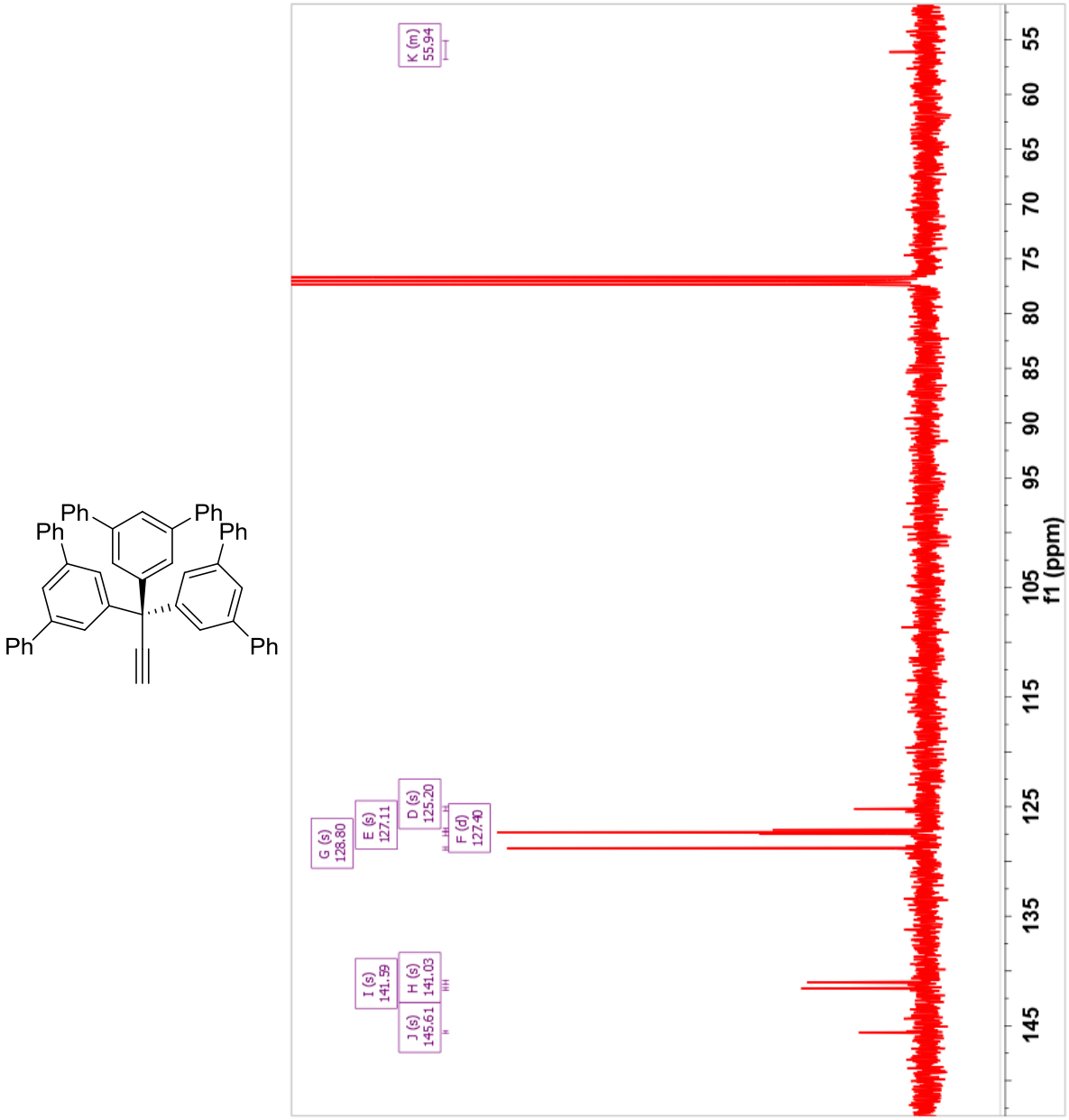


Figure 12. Carbon NMR of **3**.

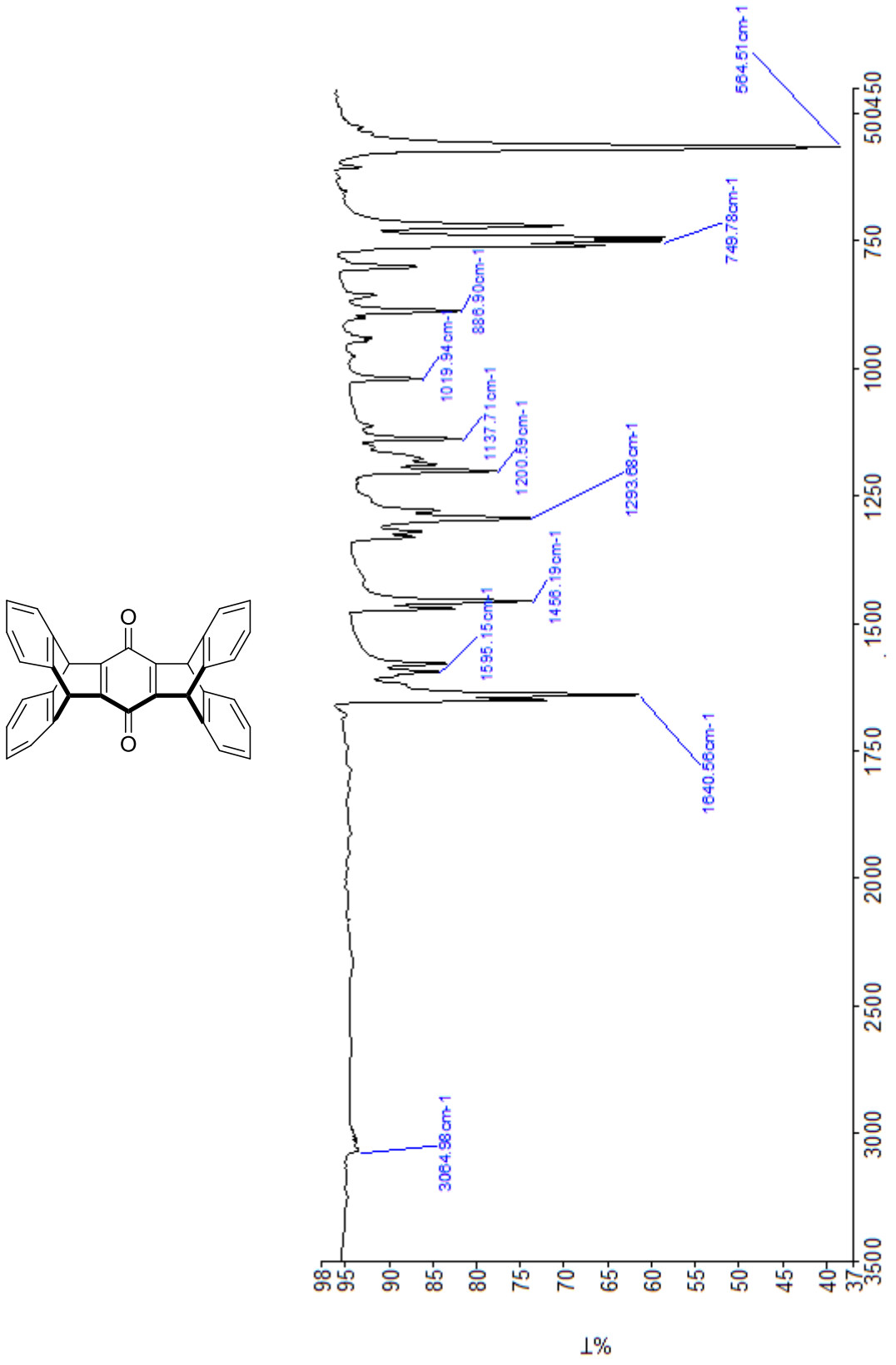


Figure 13. Infrared spectrum of **4**.

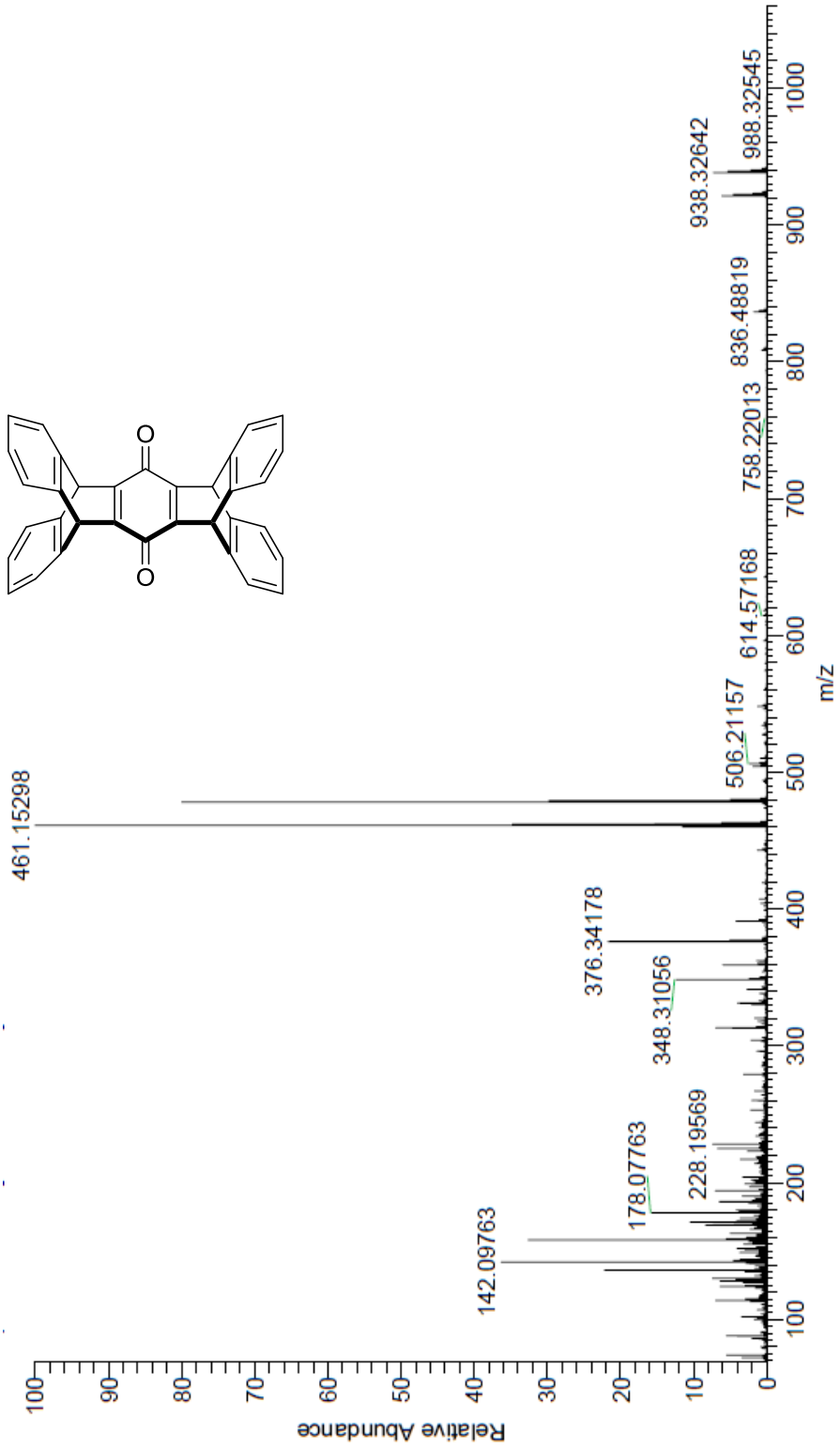


Figure 14. Mass spectrum of **4**.

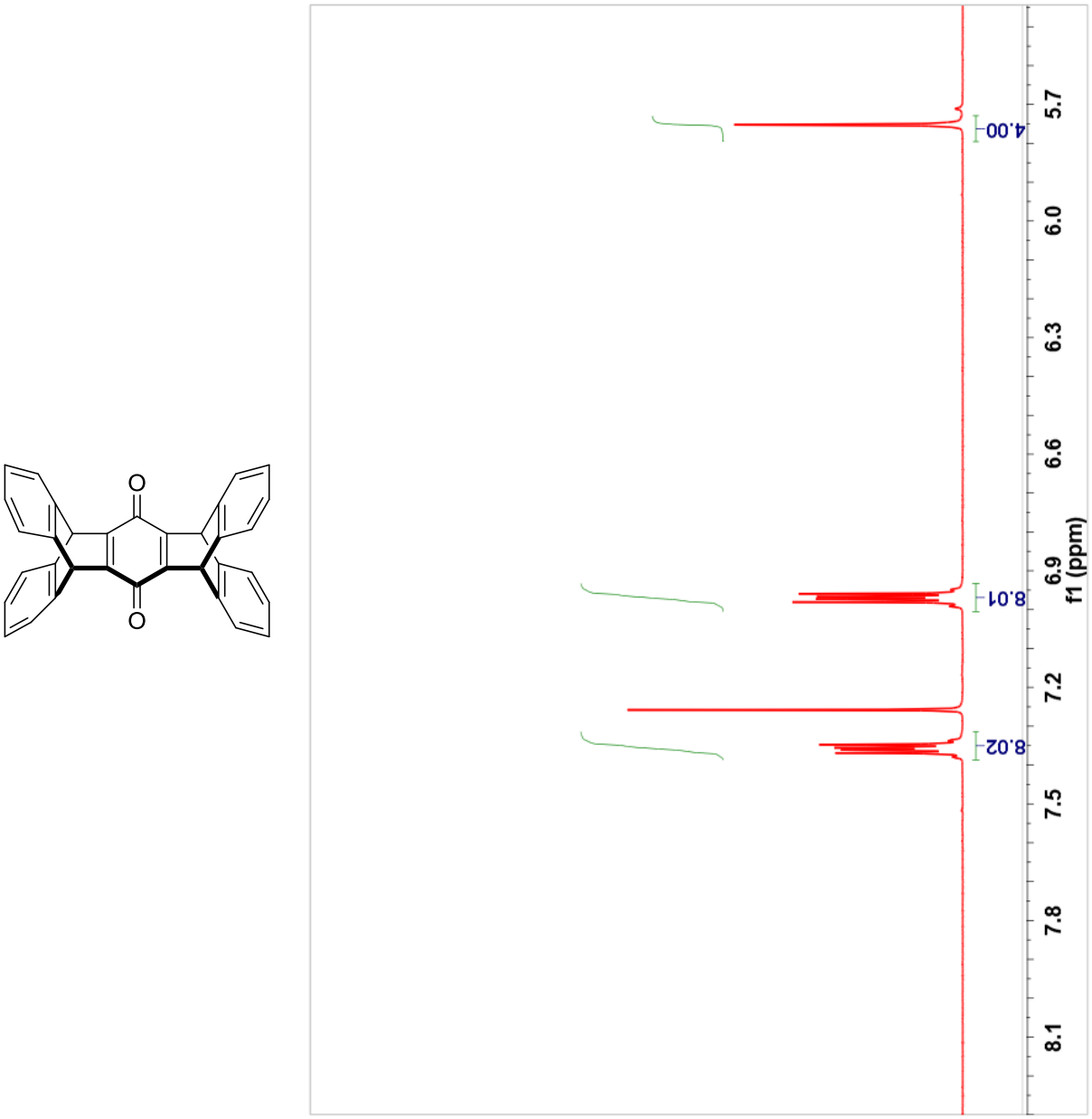


Figure 15. Proton NMR of **4**.

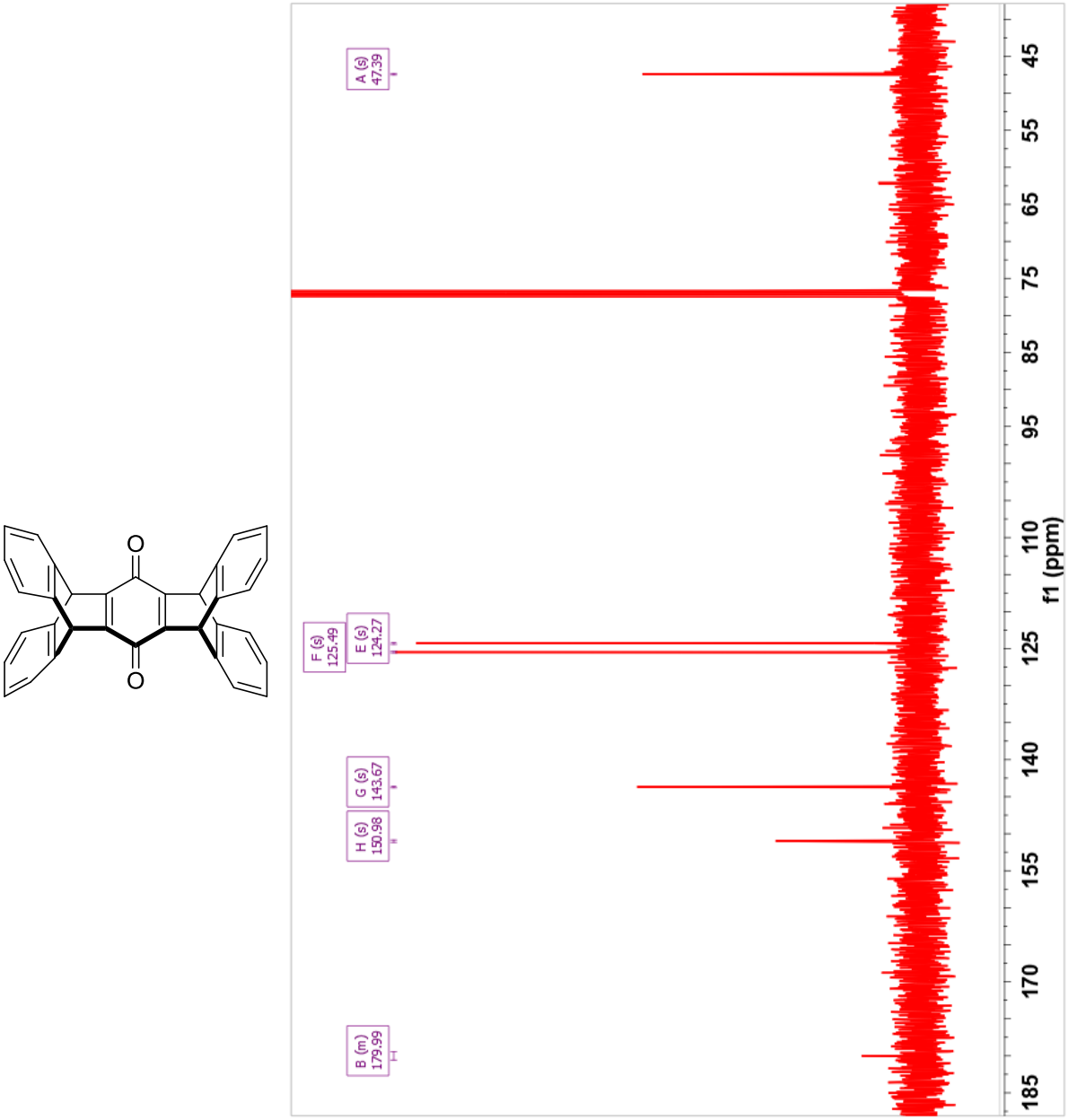


Figure 16. Carbon NMR of **4**.

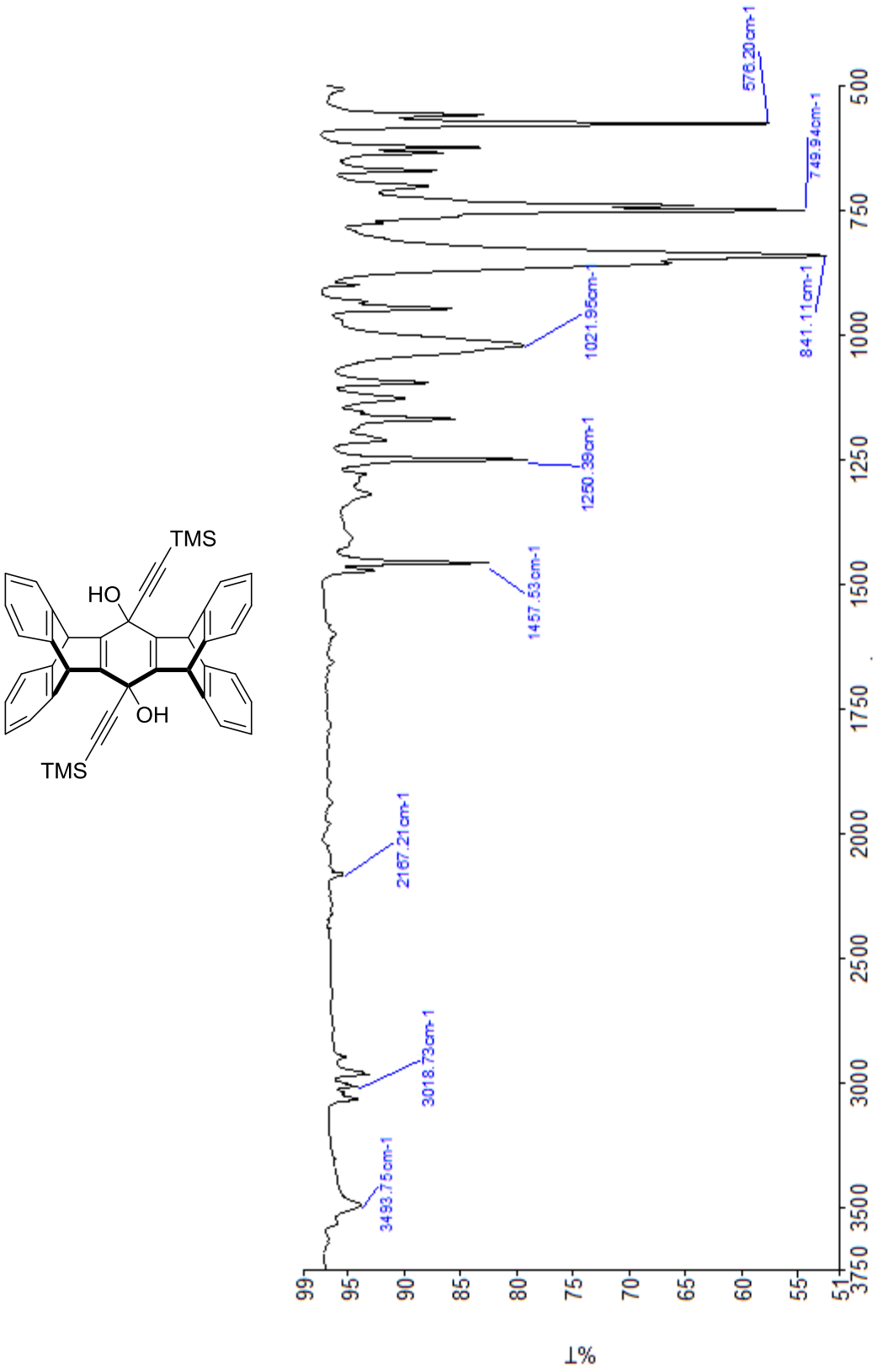


Figure 17. Infrared spectrum of **5**

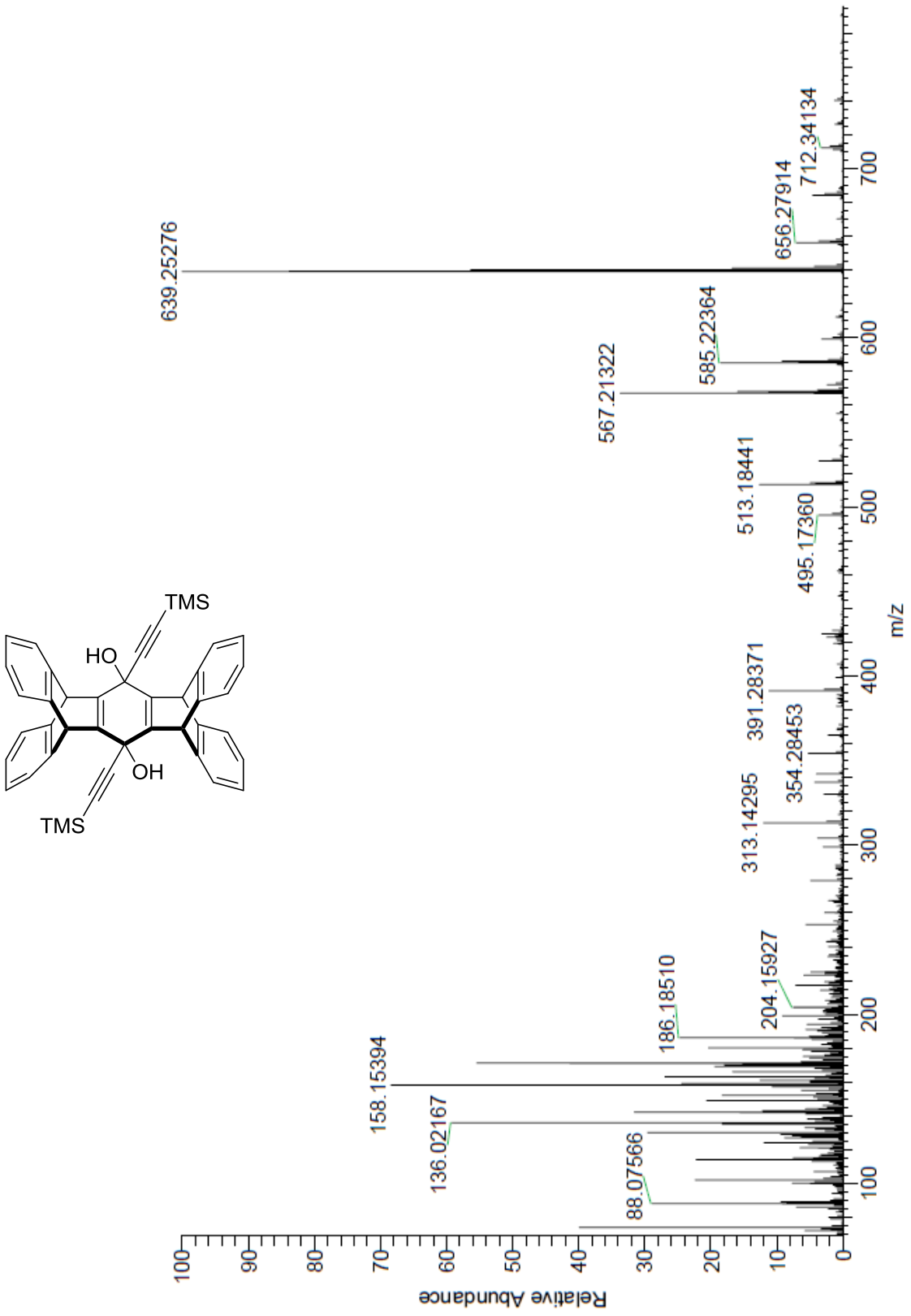


Figure 18. Mass spectrum of **5**.

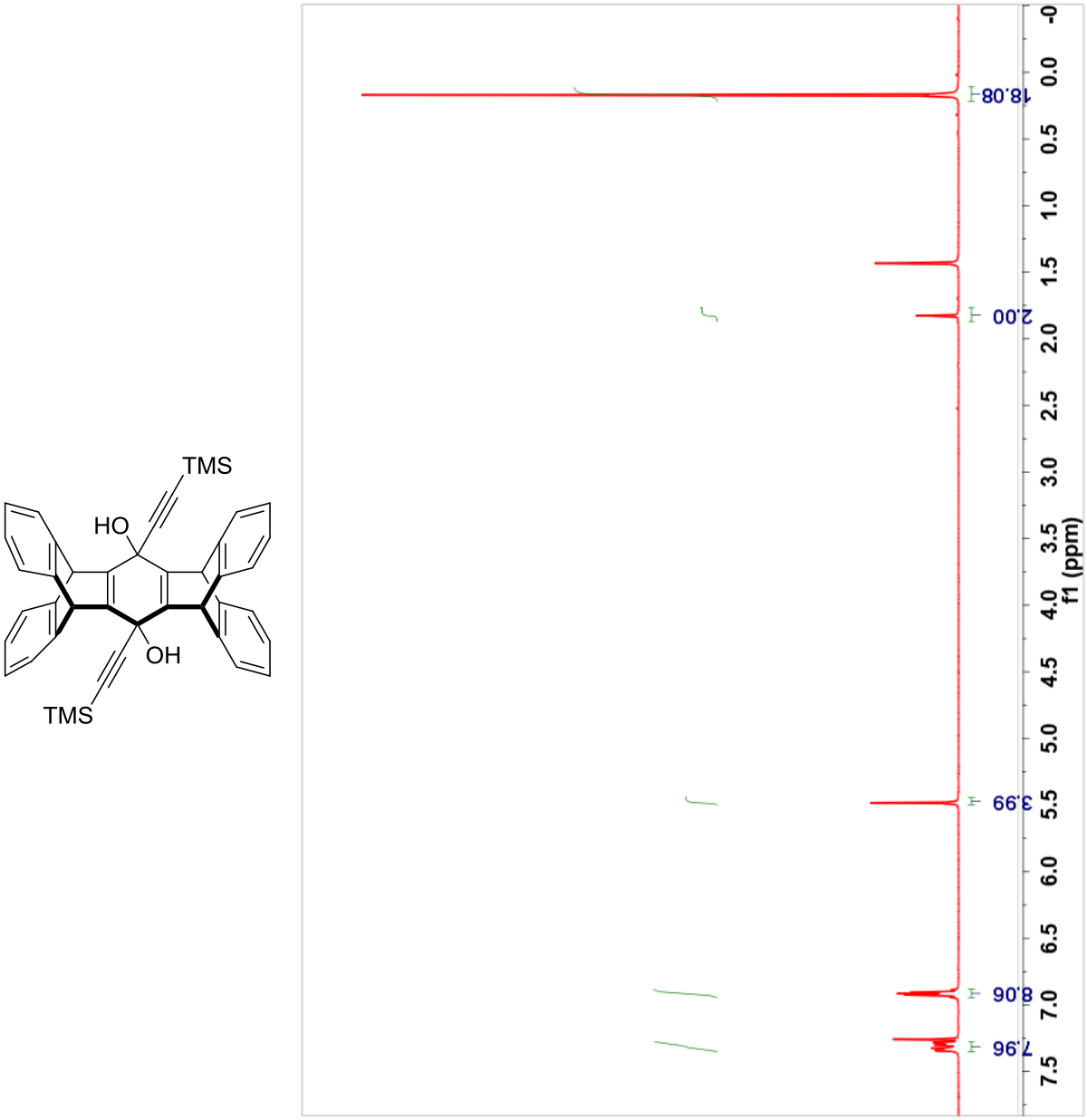


Figure 19. Proton NMR of **5**.

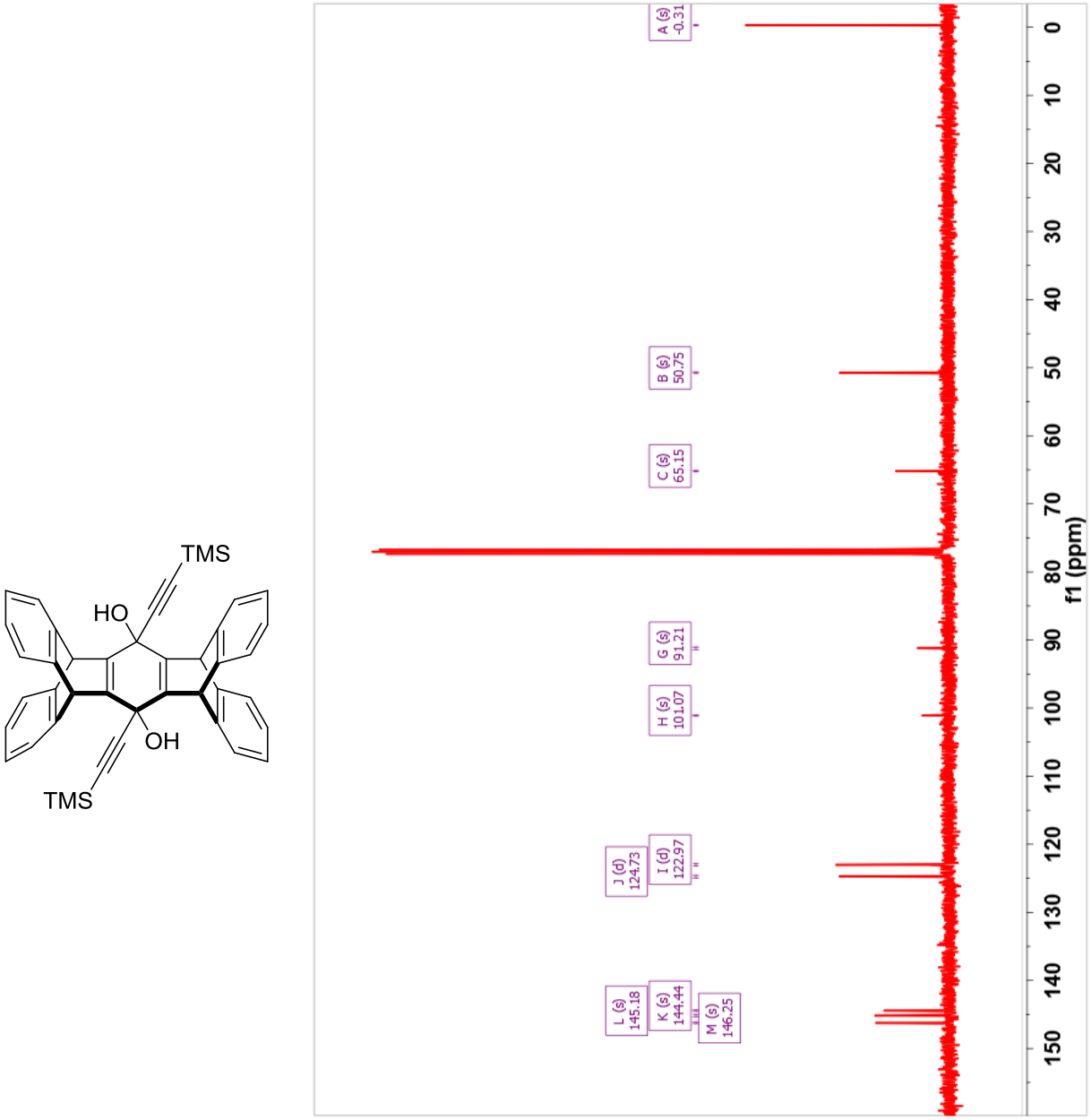


Figure 20. Carbon NMR of **5**.

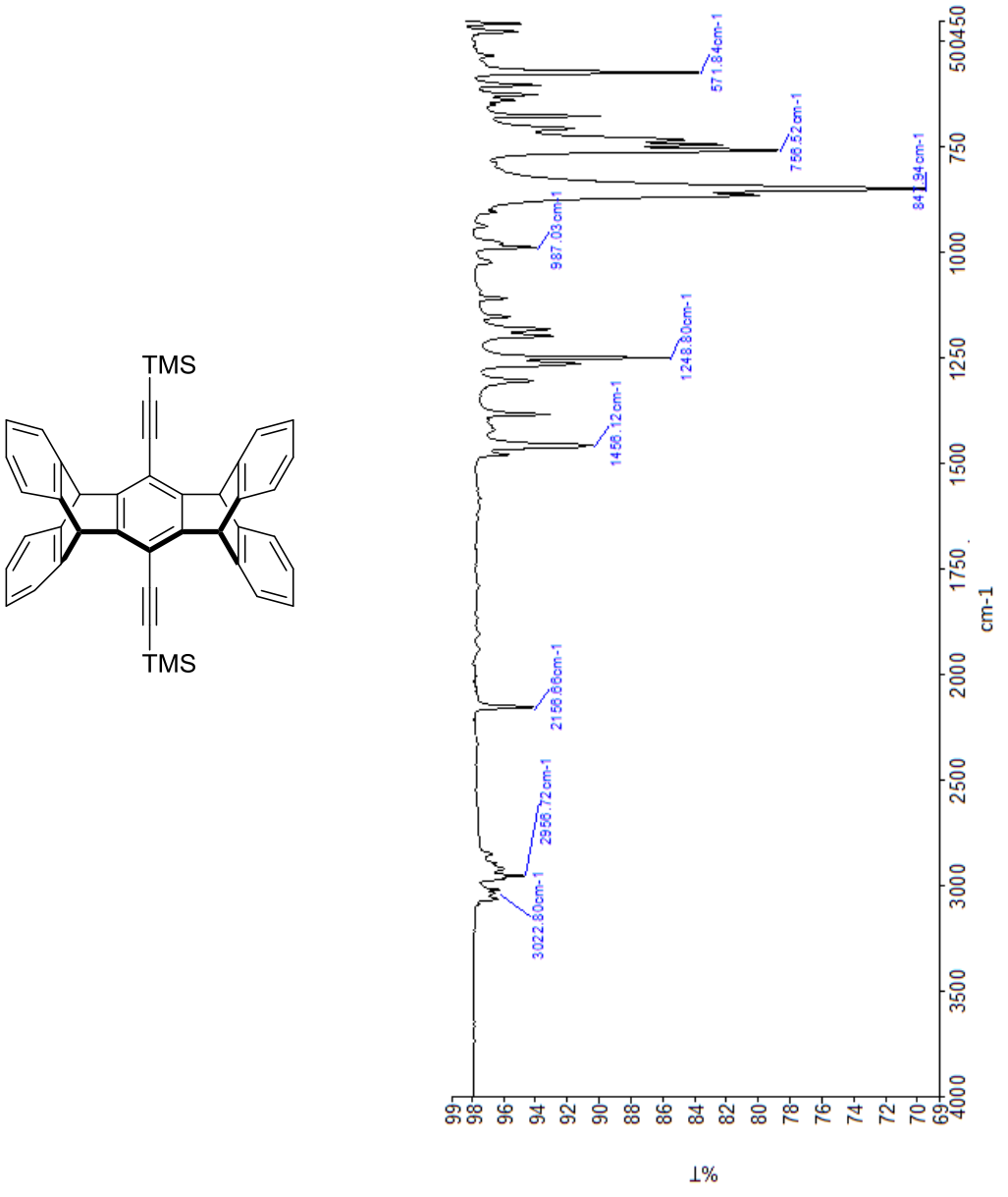


Figure 21. Infrared spectrum of **6**.

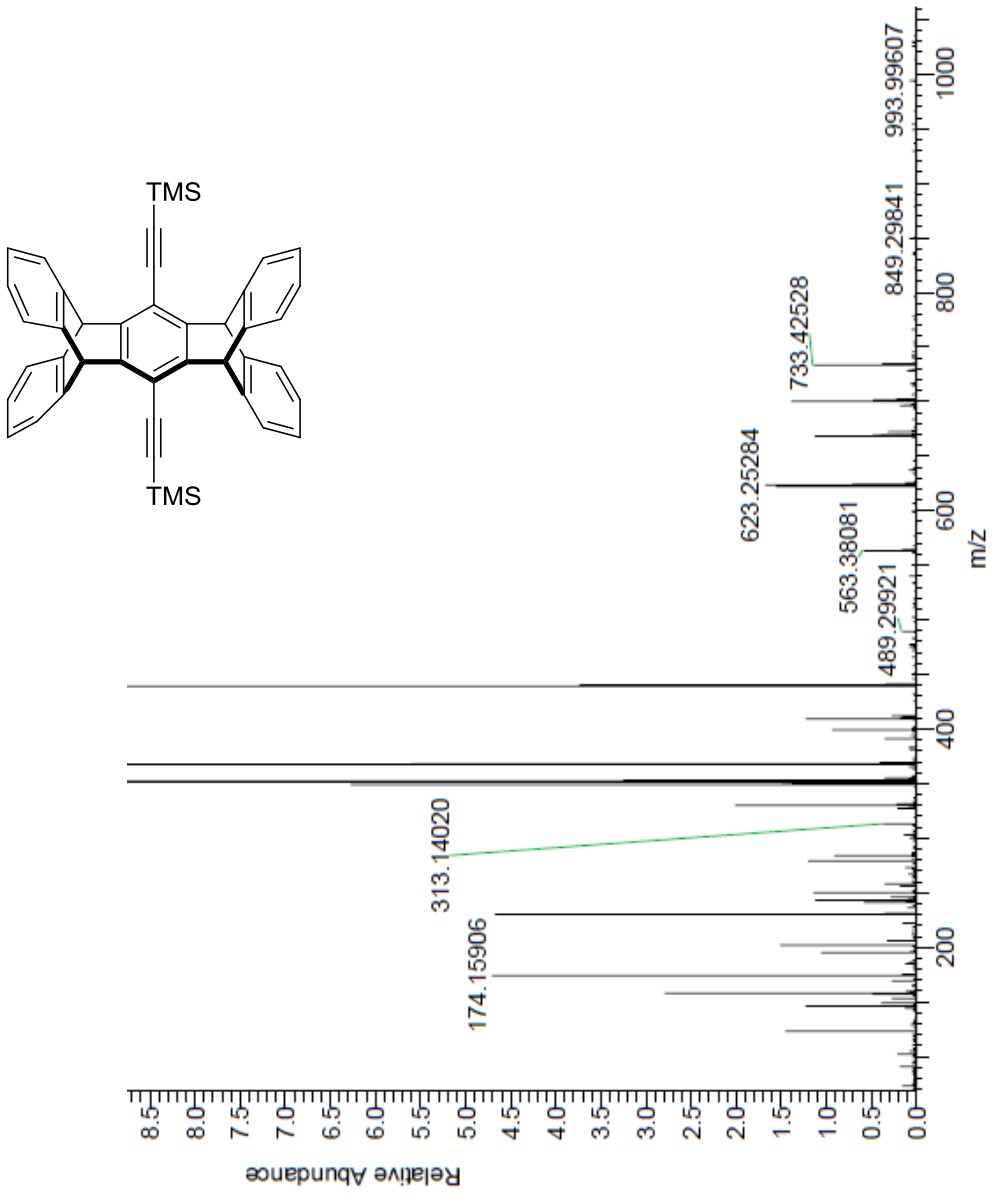


Figure 22. Mass spectrum of **6**.

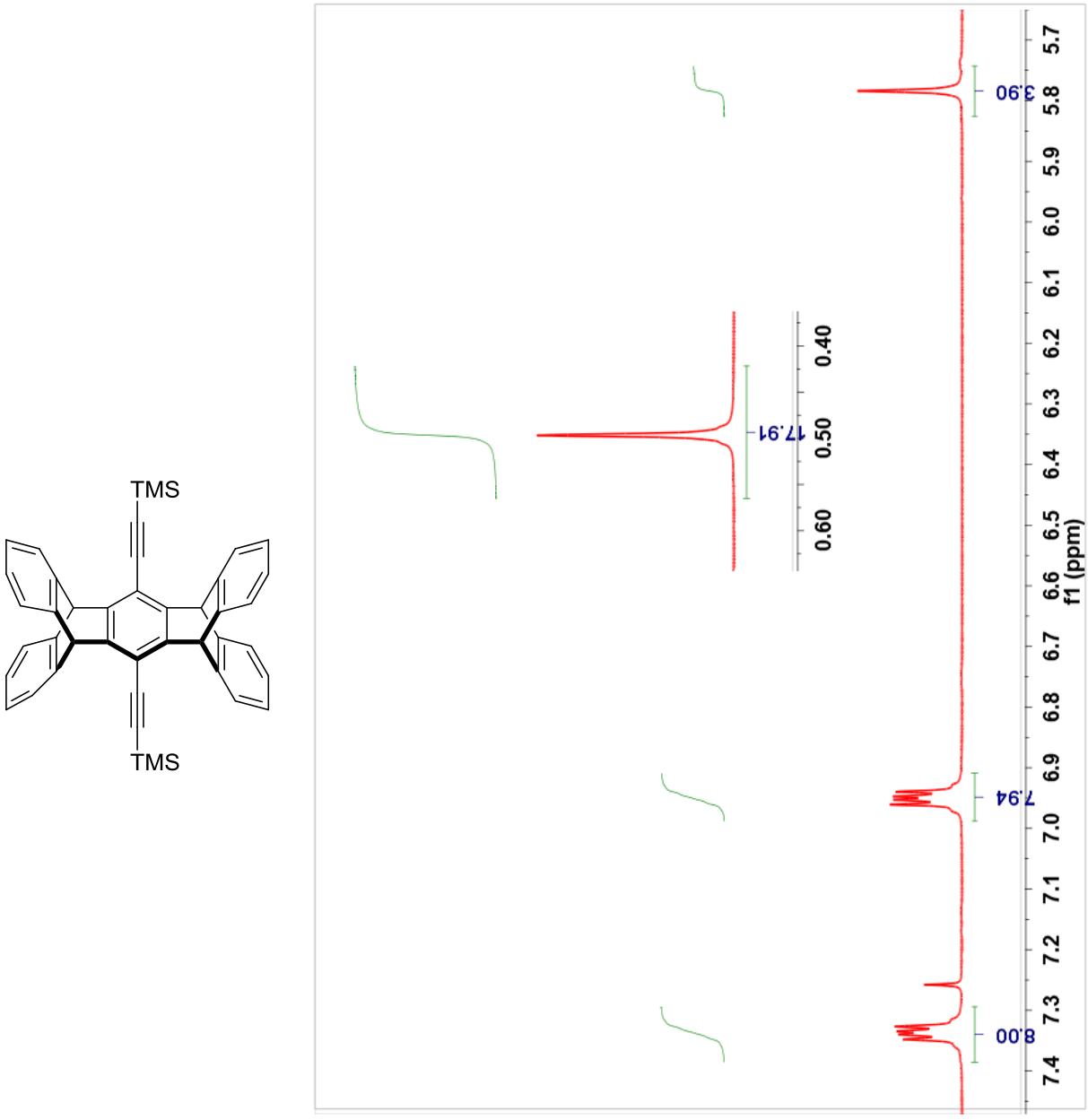


Figure 23. Proton NMR of **6**.

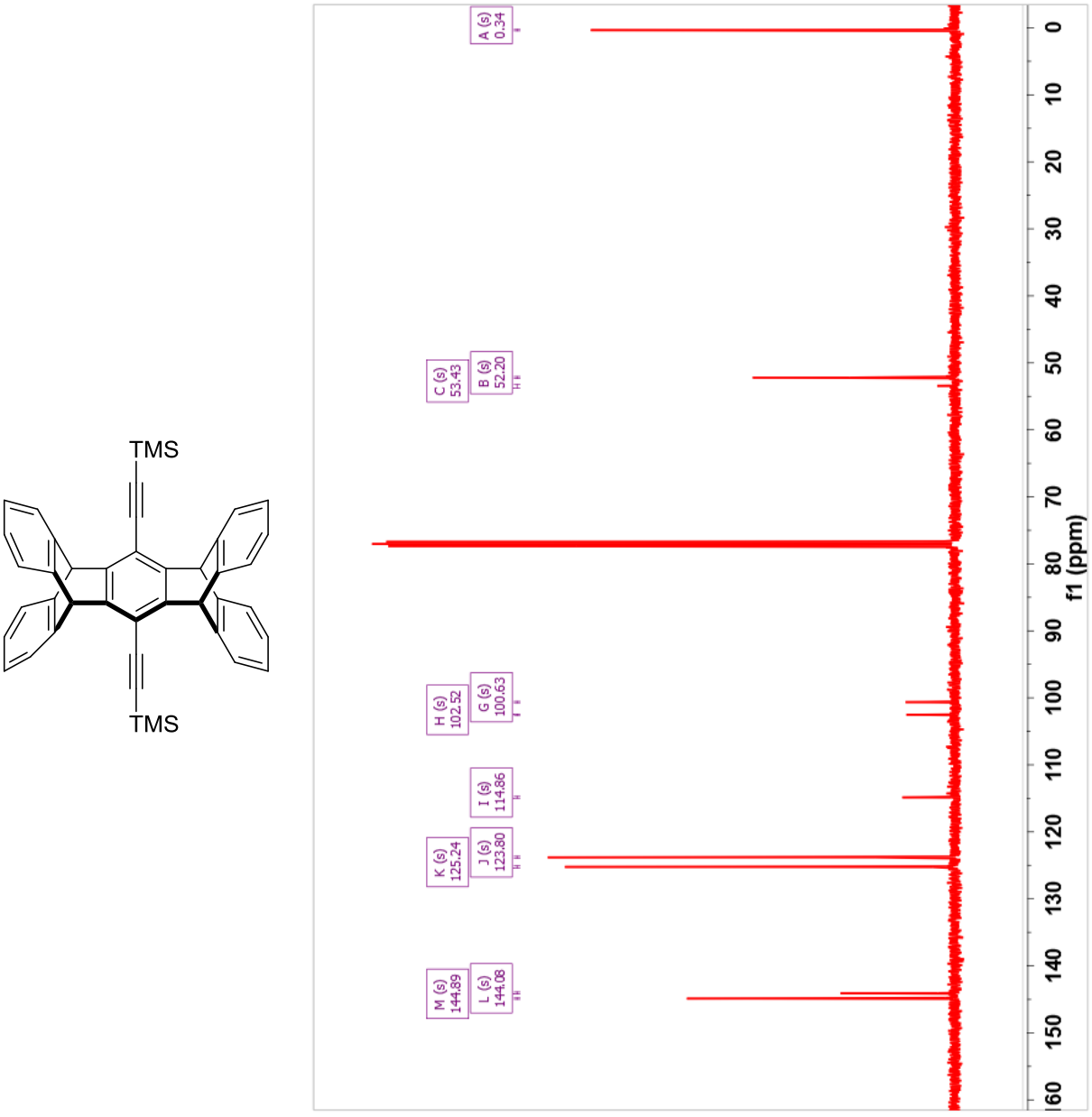


Figure 24. Carbon NMR of **6**.

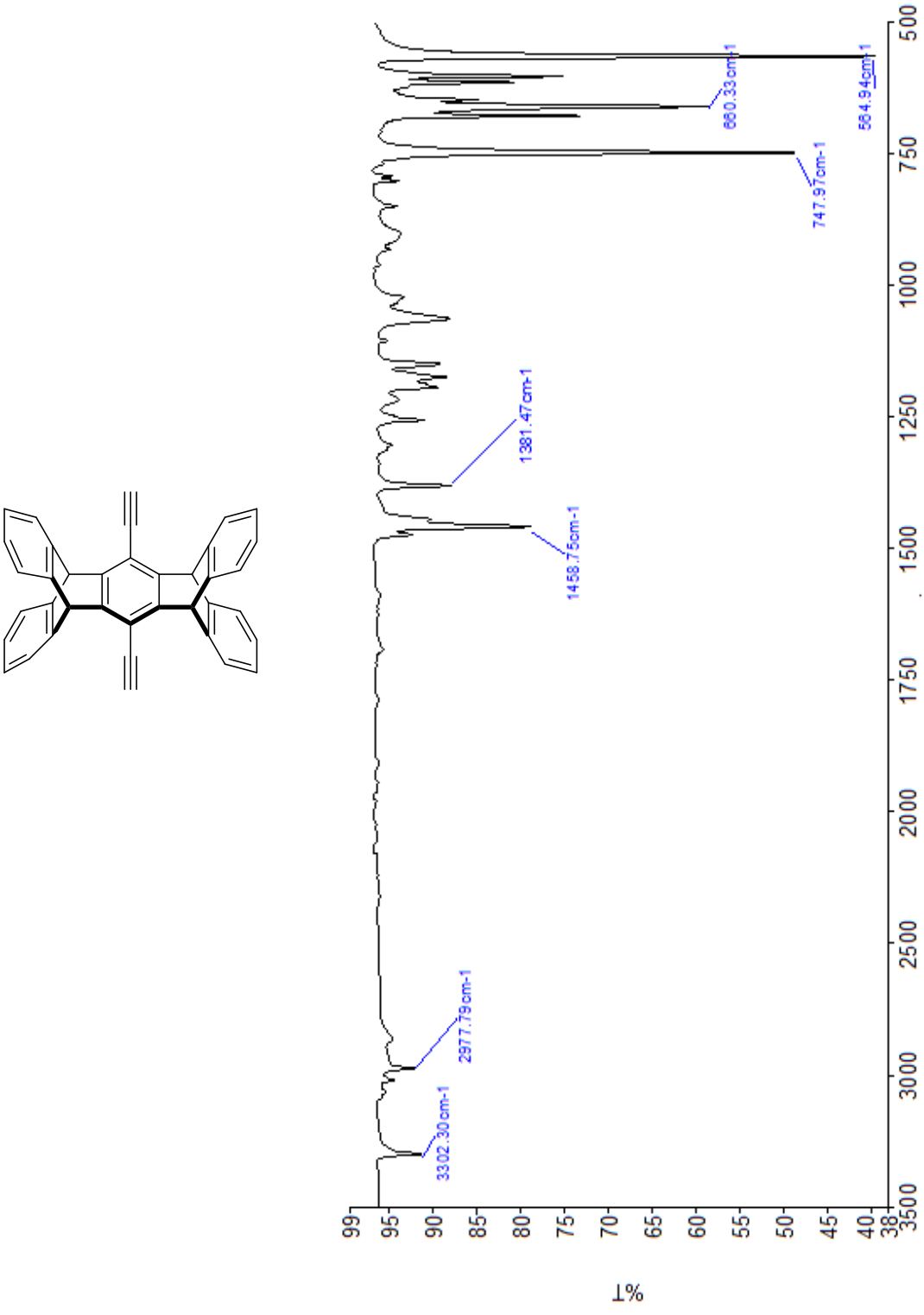


Figure 25. Infrared spectrum of **7**.

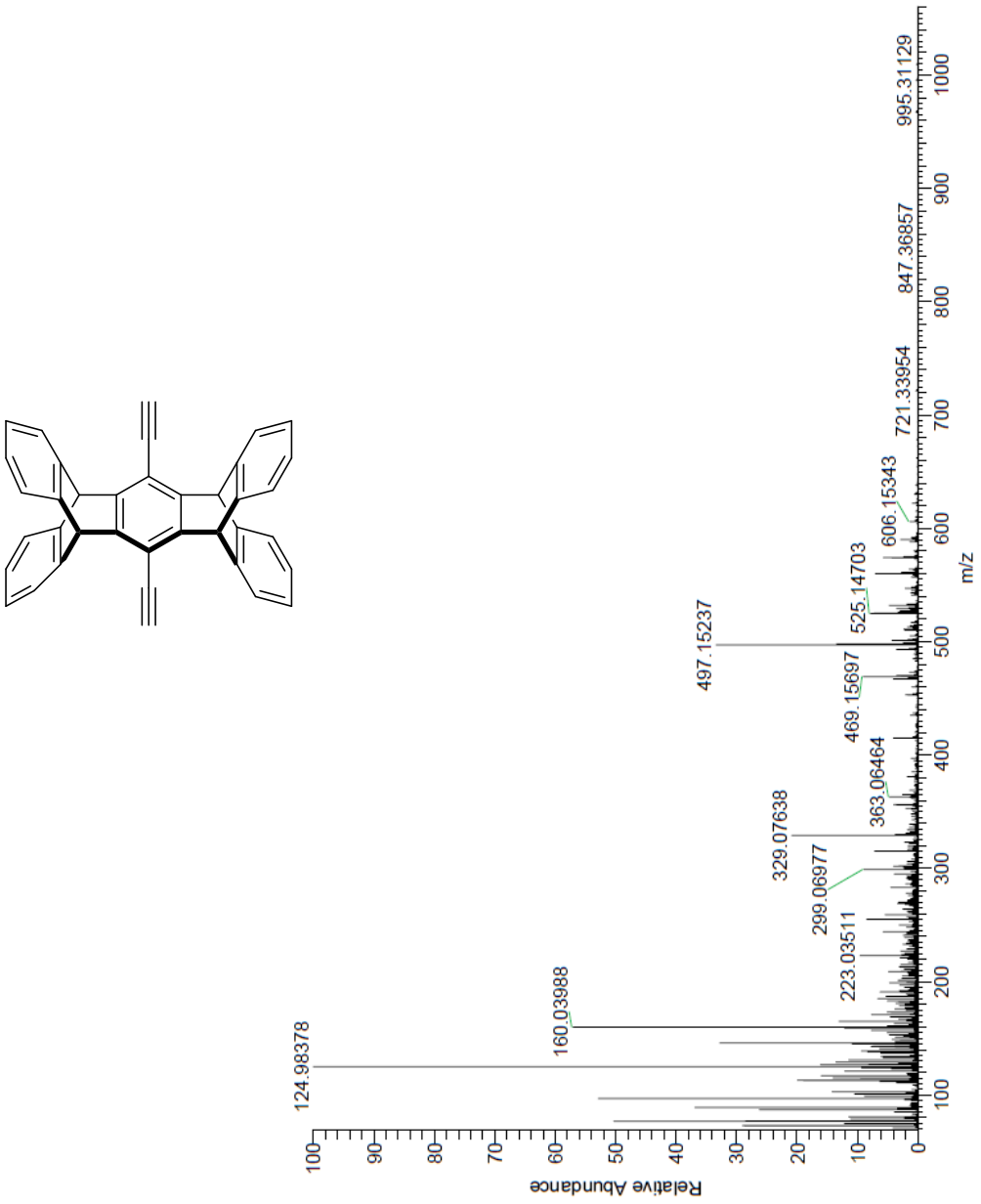


Figure 26. Mass spectrum of **7**.

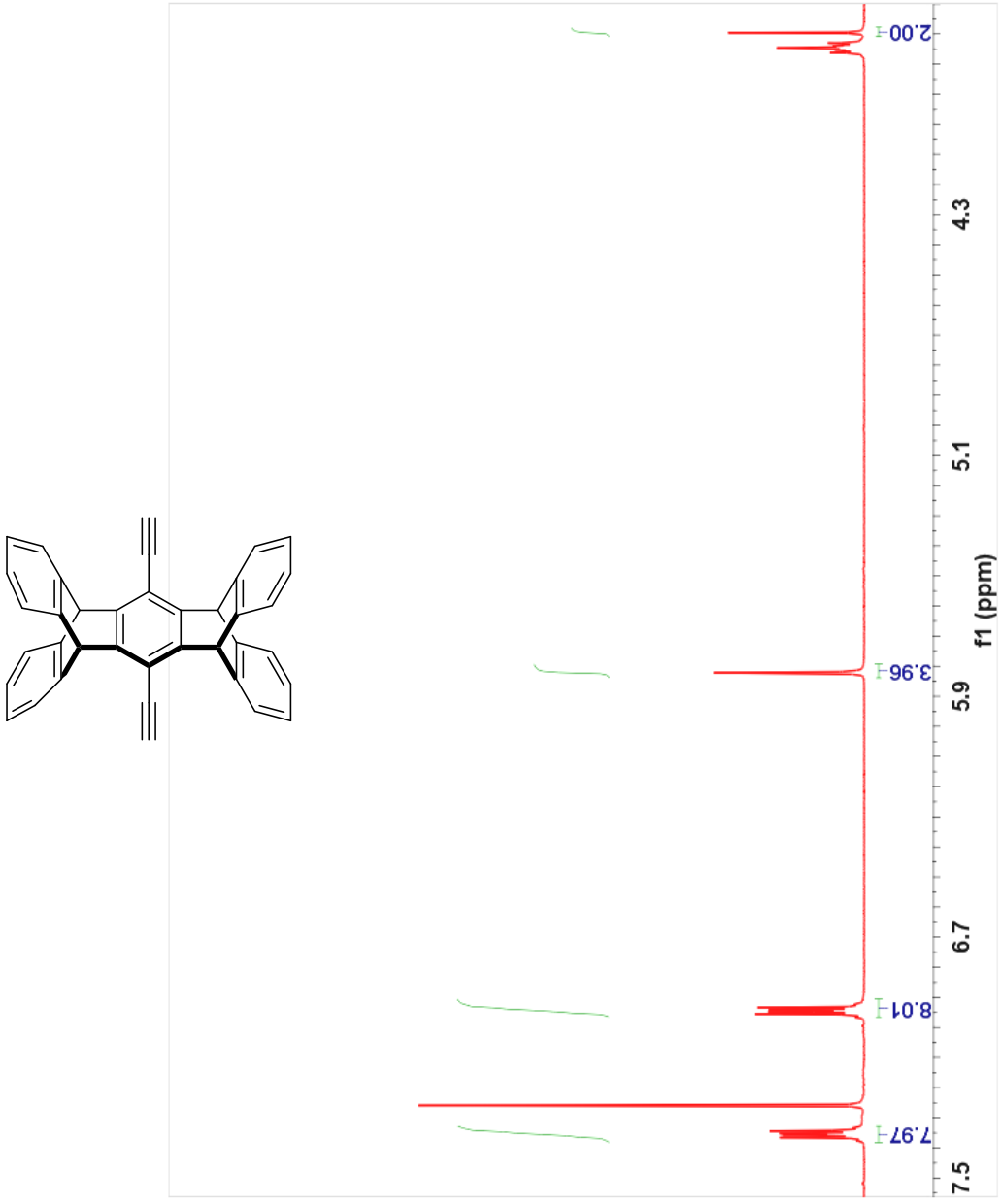


Figure 27. Proton NMR of **7**.

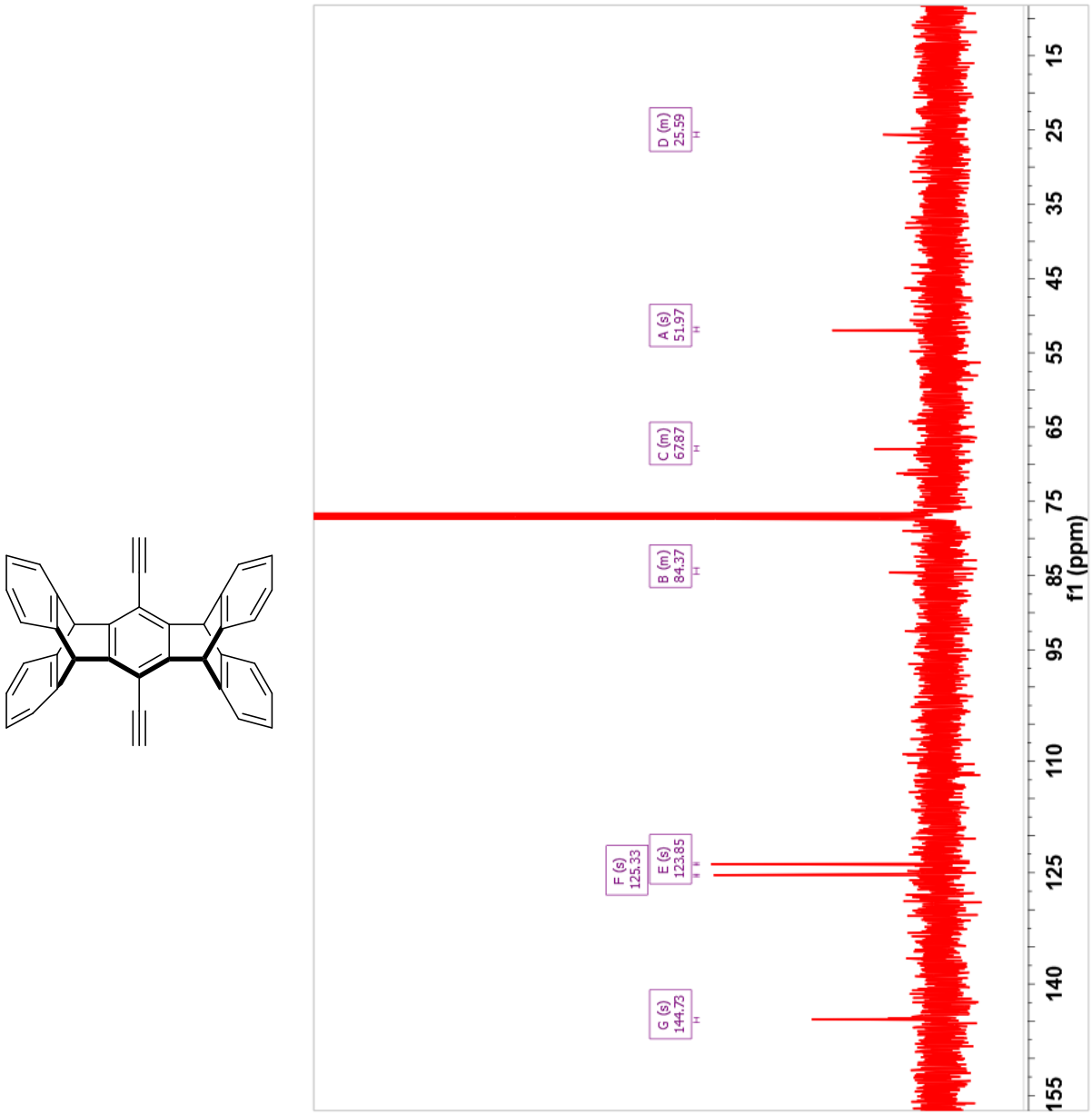


Figure 28. Carbon NMR of **7**.

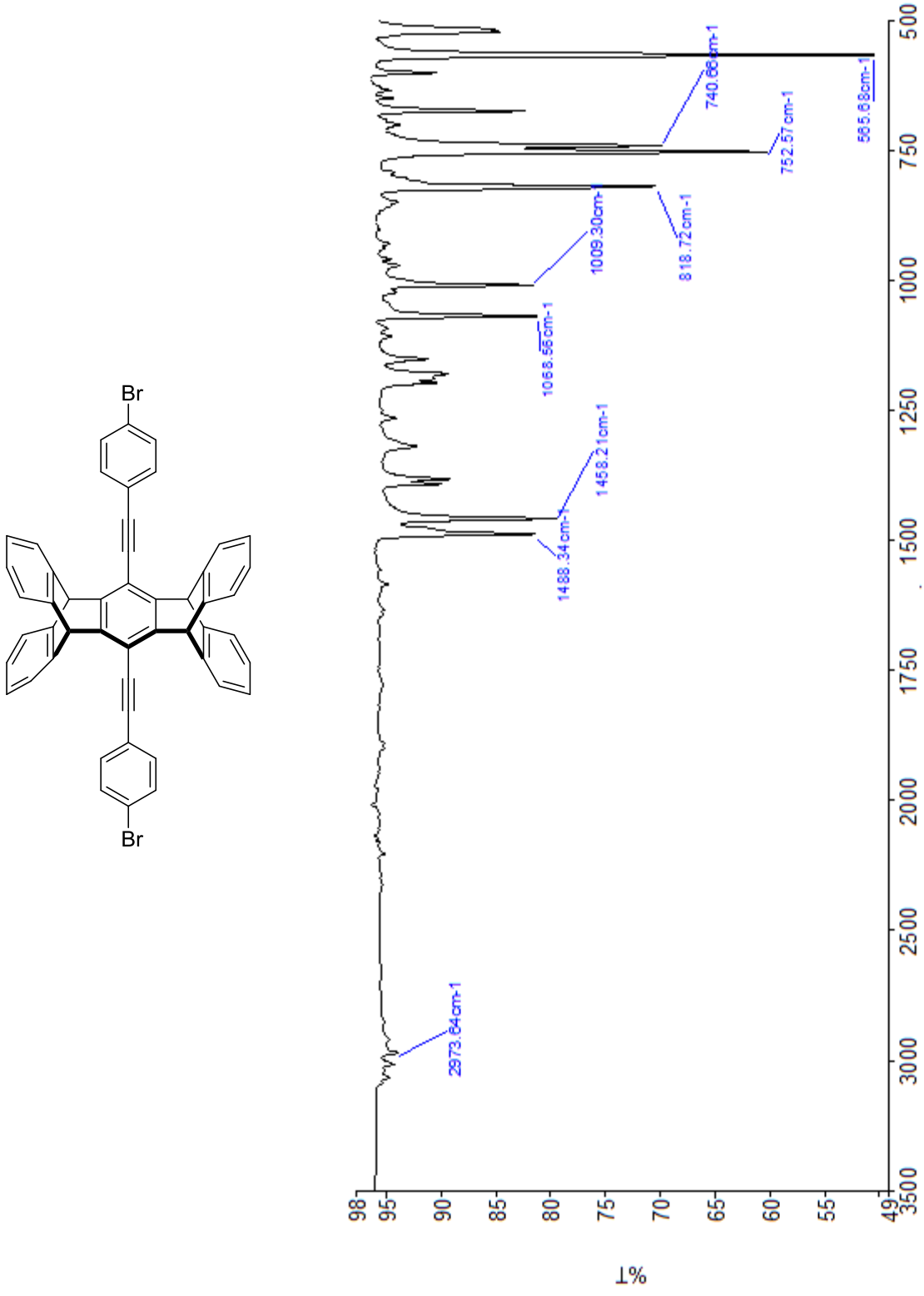


Figure 29. Infrared spectrum of **8**.

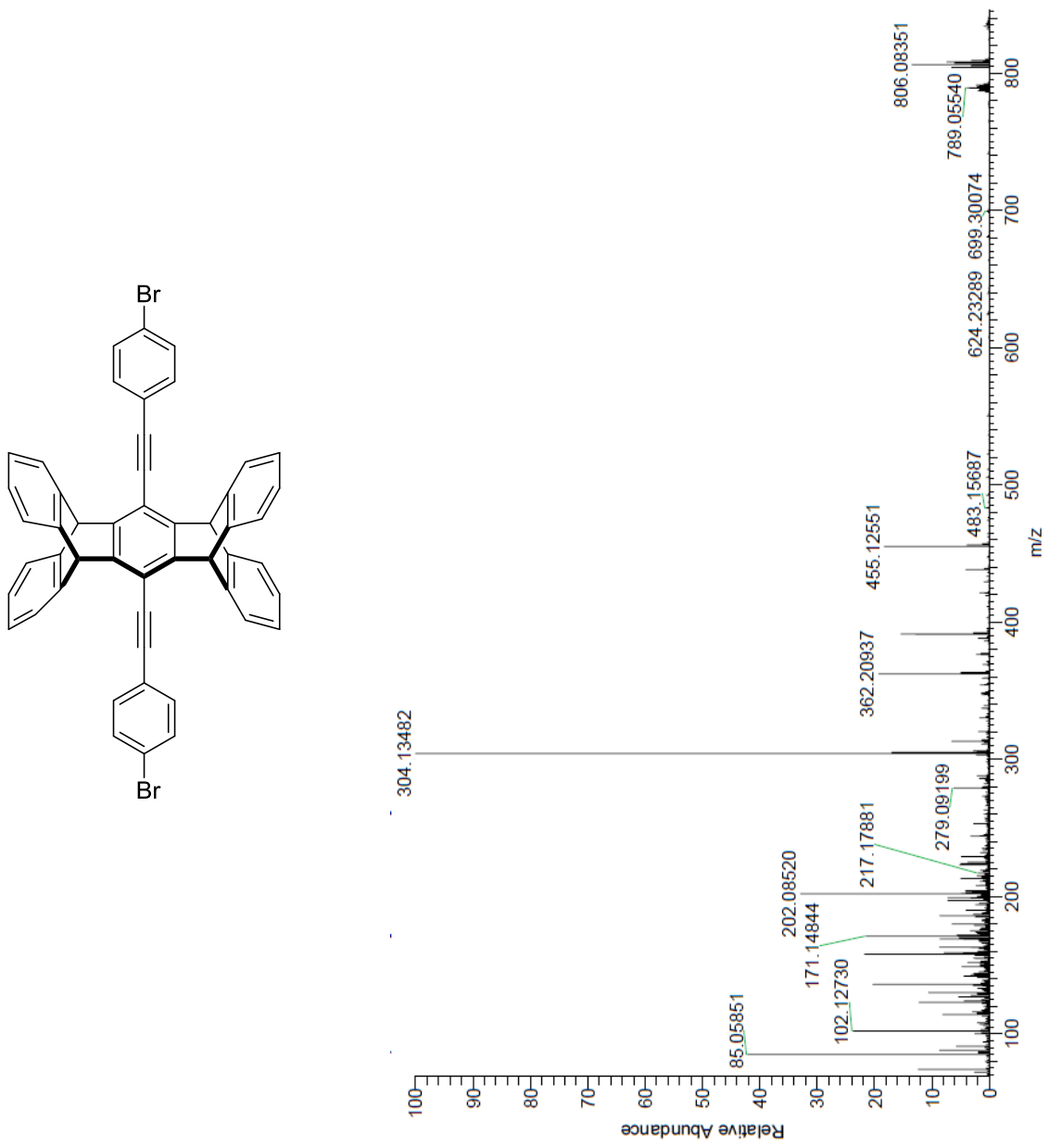


Figure 30. Mass spectrum of **8**.

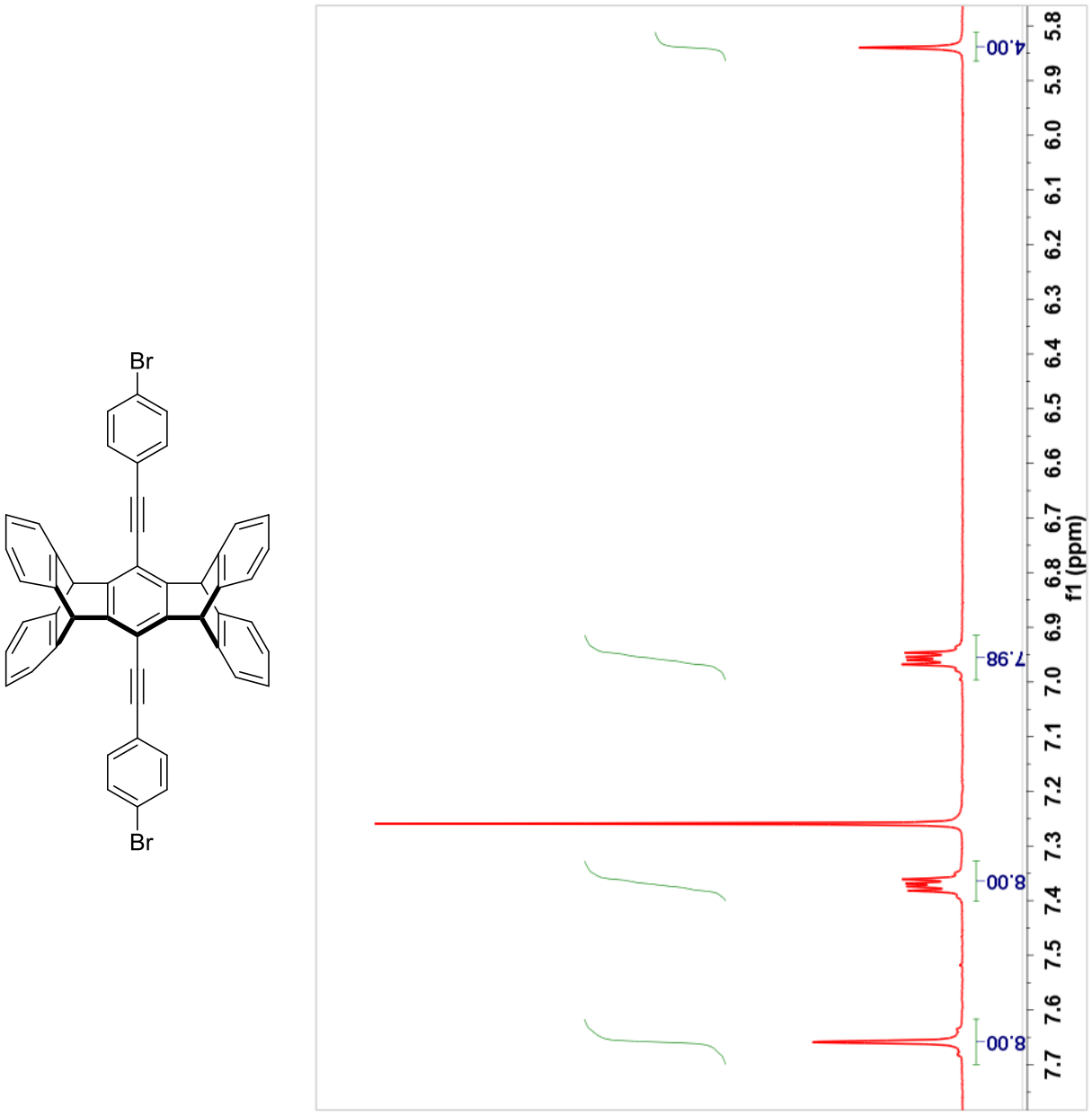


Figure 31. Proton NMR of **8**.

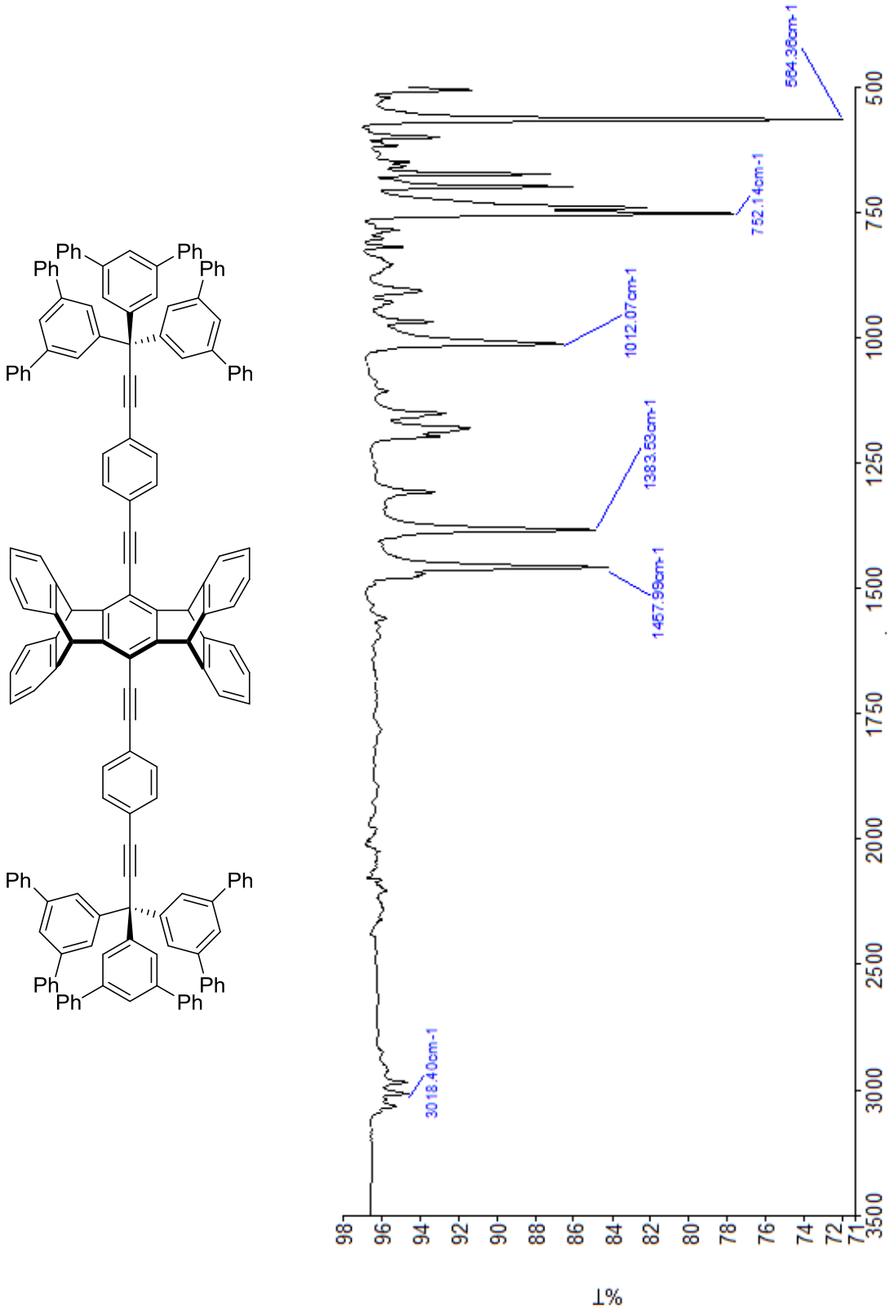


Figure 32. Infrared spectrum of **9**.

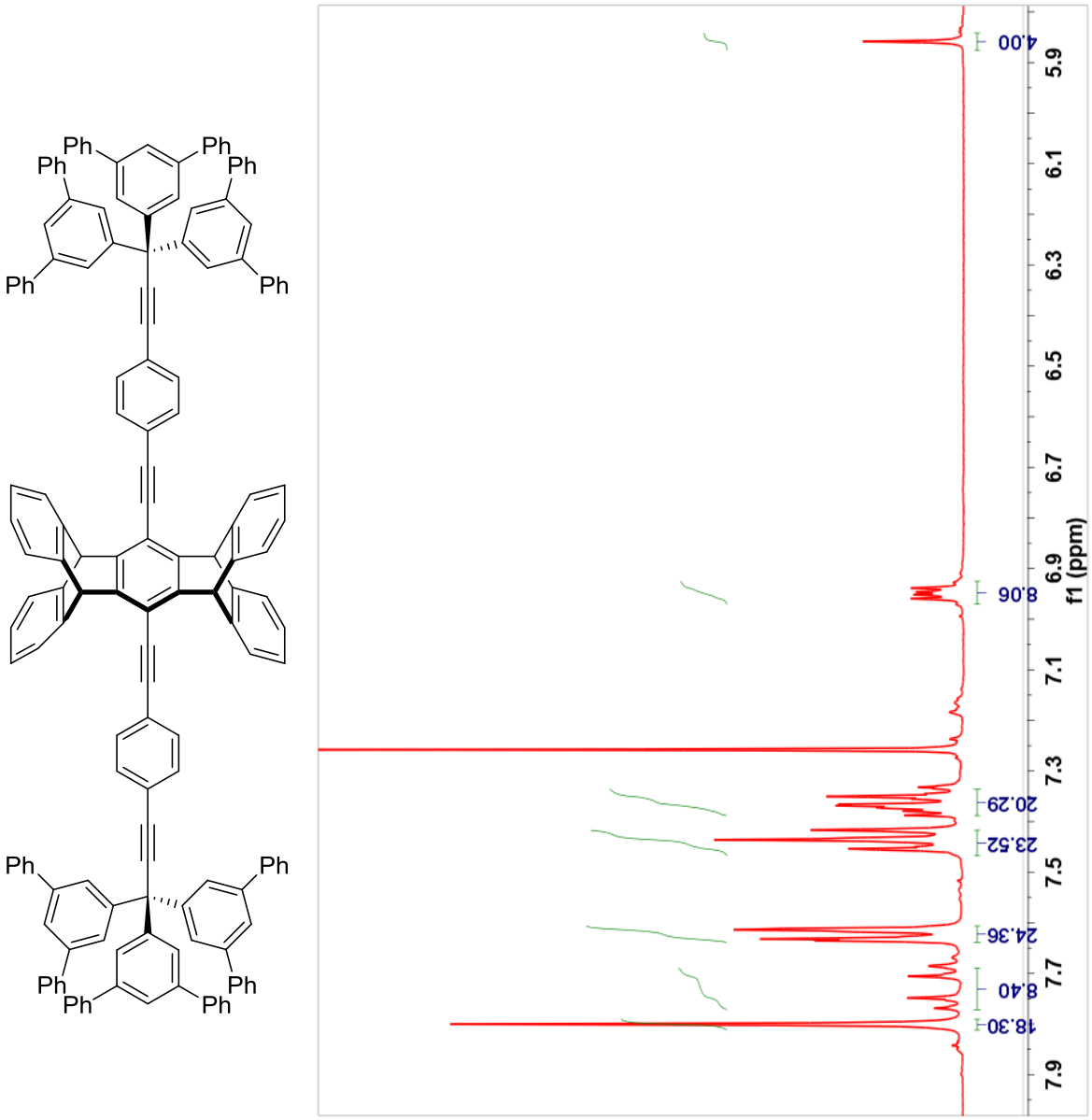


Figure 33. Proton NMR of **9**.

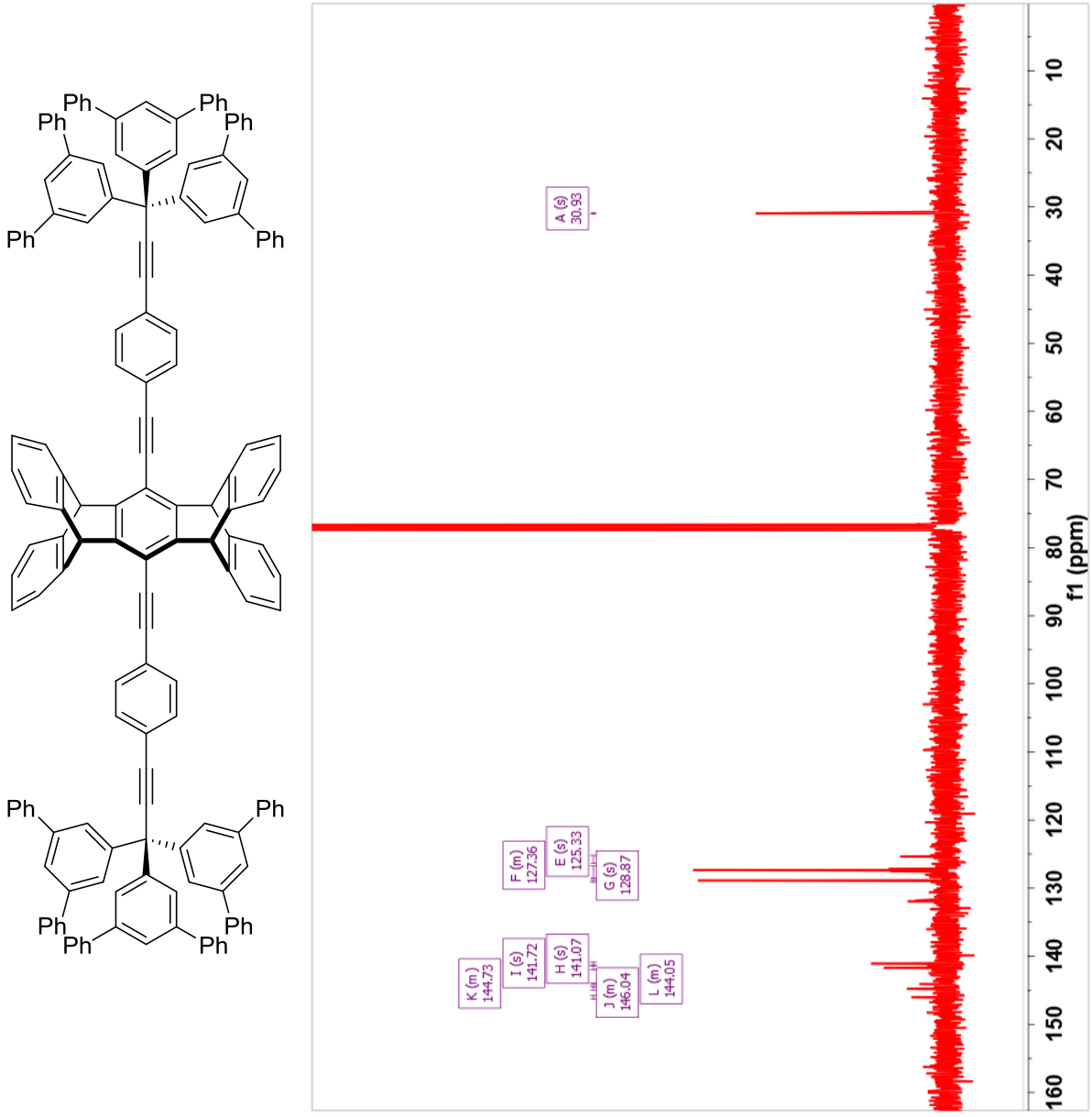


Figure 34. Carbon NMR of **9**.

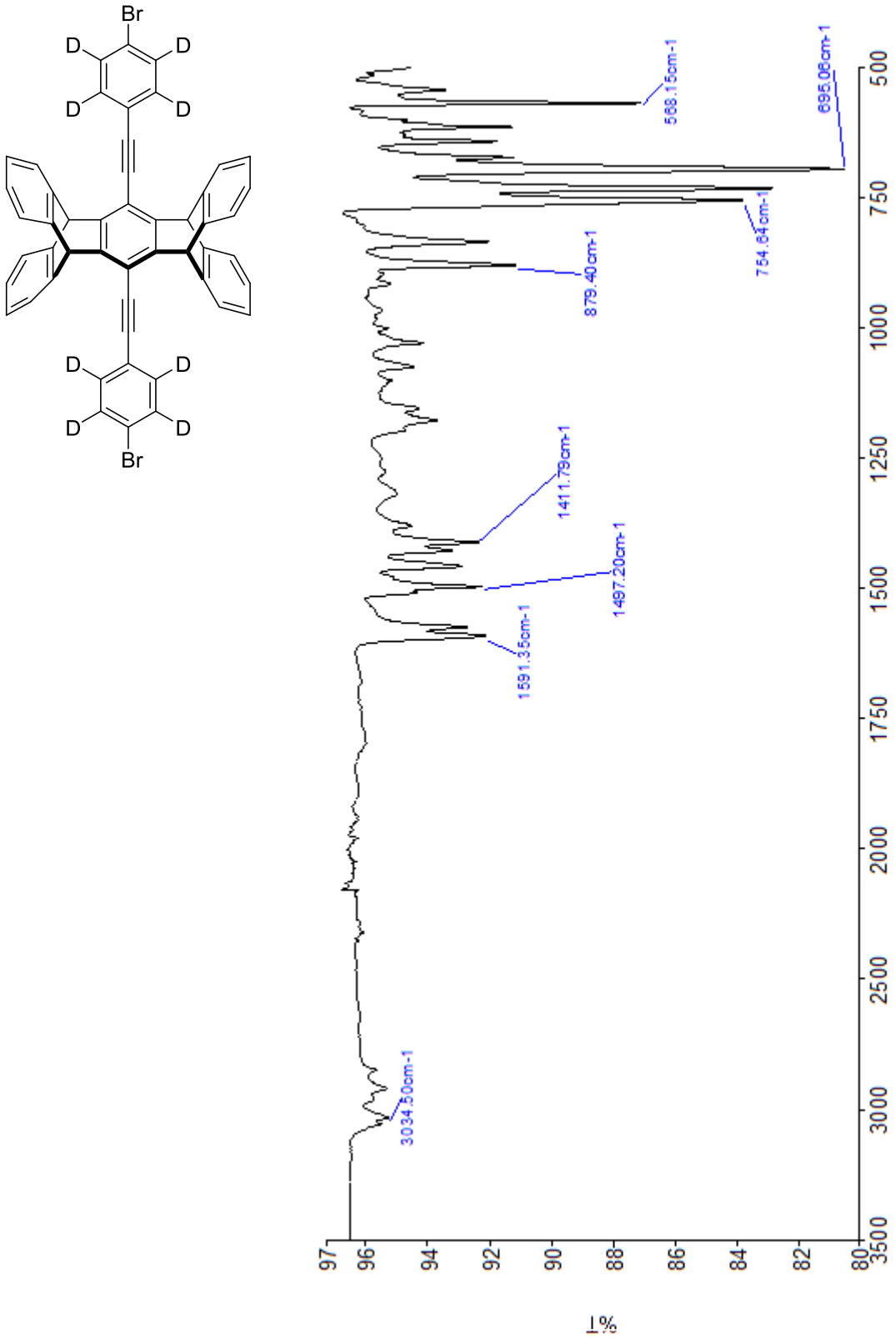


Figure 35. Infrared spectrum of **10**.

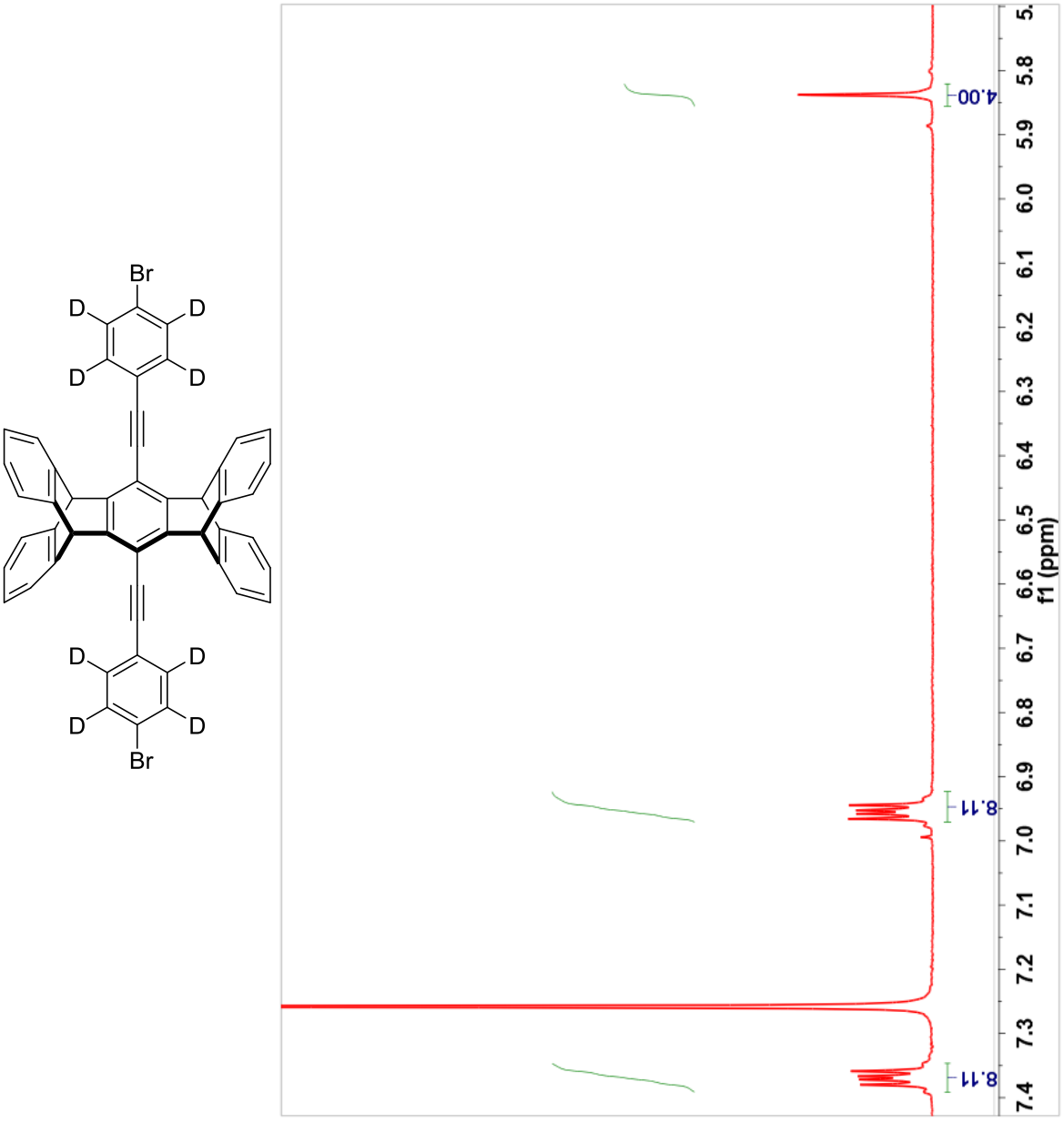


Figure 36. Proton NMR of **10**.

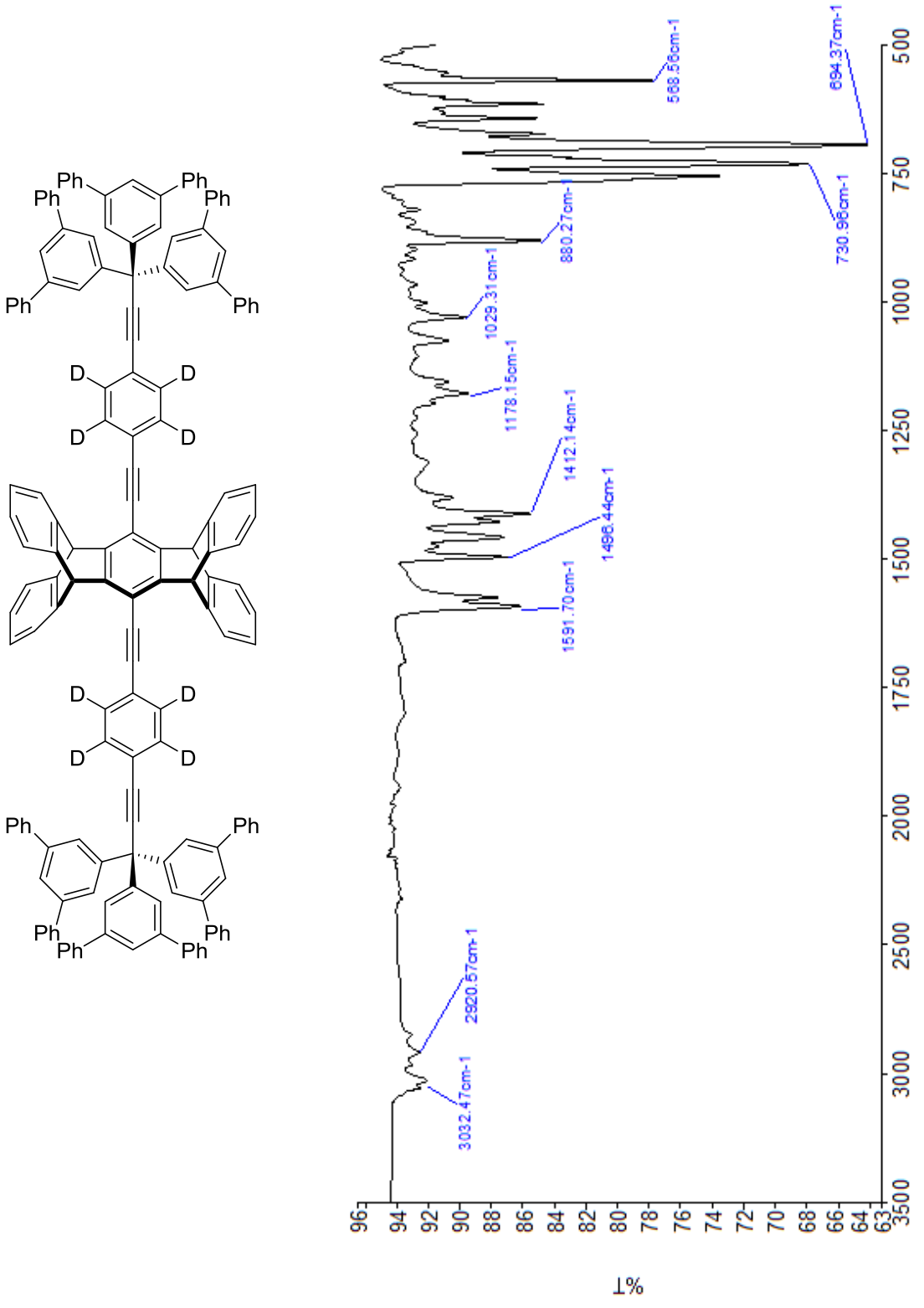


Figure 37. Infrared spectrum of **11**.

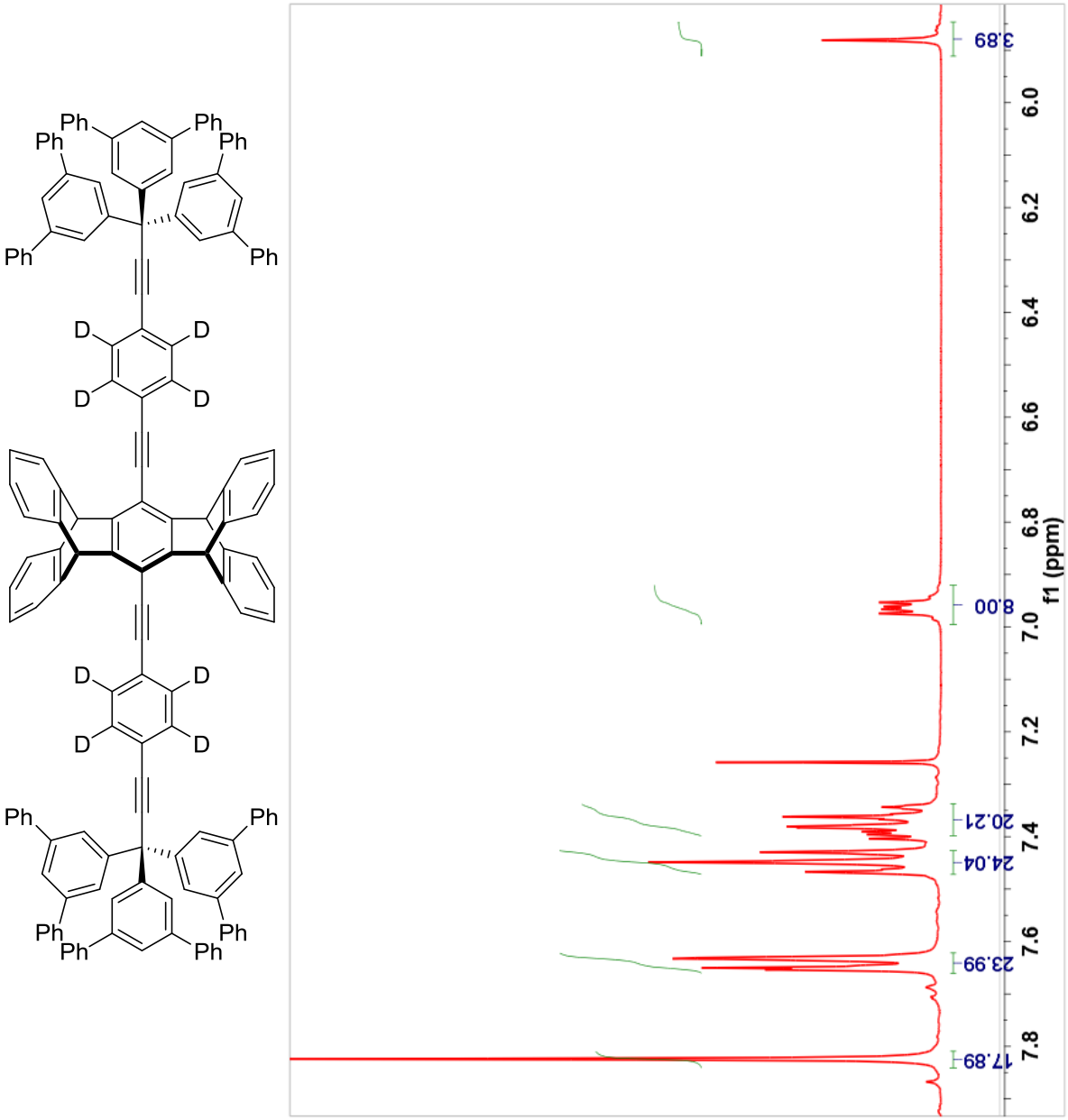


Figure 38. Proton NMR of **11**.

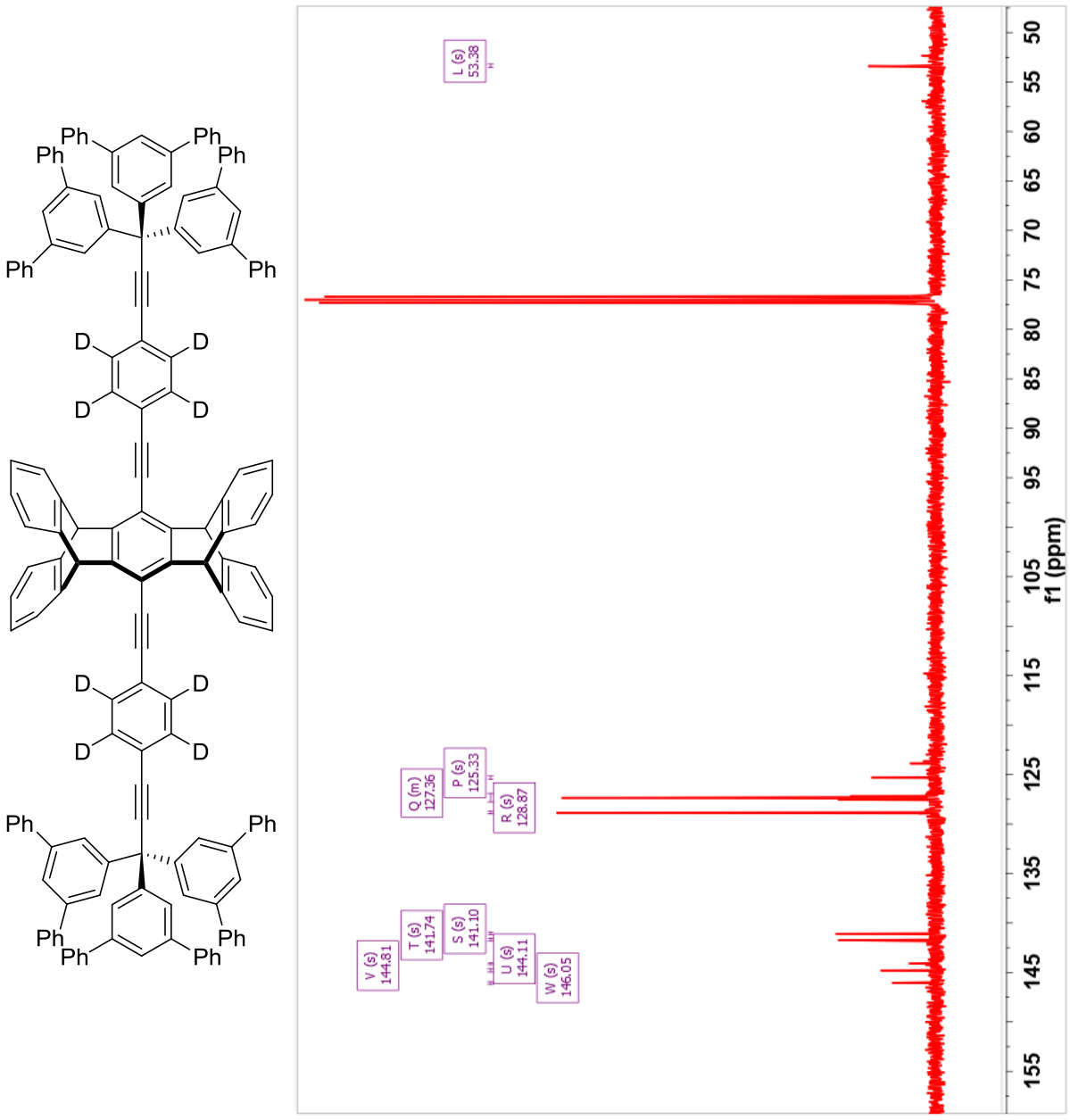


Figure 39. Carbon NMR of **11**.

References

1) Godinez, C. E. (2001). *Synthetic Strategies and Spectroscopic Studies of Organic Compounds with Freely Rotating Chromophores with Potentially Interesting Electro-Optical Properties.*

2) Saleh, B. E.; Teich, M. C. *Fundamentals of Photonics;* John Wiley & Sons: New York, 1991.

3) Collings, P. J.; Hird, M. *Introduction to Liquid Crystals Chemistry and Physics*; Taylor & Francis: Bristol, 1997.

4) Nakamoto, R. K.; Scanlon, J. A. B.; Al-Shawi, M. K. *Arch. Biochem. Biophys.* **2008,** *476*(1), 43–80.

5) Ballardini, R.; Balzani, V.; Credi, A.; Gandolfi, MT, Venturi, M. *Acc. Chem. Res., 34,* **2001**, 6, 445–455.

6) Merino, E.; Beilstein, M. R. *J. Org. Chem.* **2012**, *8*, 1071–1090.

7) Dominguez, Z.; Dang, H.; Strouse, M.J.; Garcia-Garibay, M.A. *J. Am. Chem. Soc*. **2002**, *124*, 2398-2399.

8) O'Brien, Z.J.; Natarajan, A.; Khan, S.I.; Garcia-Garibay, M.A. *Crystal Growth & Design.* **2011,** *11*, 2654-2659.

9) Hughs, M.; Jimenez, M.; Khan,S.I.; Garcia-Garibay, M.A. *J. Org. Chem*. **2013,** *78,* 5293–5302.

10) Horansky, R. D.; Clarke, L. L.; Winston, E. B.; Price, J. C.; Karlen, S. D.; Jarowski, P. D.; Santillan, R.; Garcia-Garibay, M. A. *Phys. Rev. B.* **2006,** *74,* 054306.

11) Levitus, M.; Schmieder, K.; Ricks, H.; Schimizu, K. D.; Bunz, U. H. F.; Garcia-Garibay, M. A. *J. Am. Chem. Soc.* **2001,** *124,* 8181.

12) Okuyama, K.; Hasegawa, T.; Ito, M; Mikami, N. *J. Phys. Chem.* **1984,** *88*, 1711.

13) Yang, J.-S.; Yan, j.-L; Lin, C. K.; Chen, C.-Y.; Chiou, S.-Y.; Liau, K. L.; Gavin Tsai, H. H.; Lee, G. H.; Peng, S. M. *J. Am. Chem. Soc.* ***2006,*** *128*, 14109.

14) Matsumoto, K.; Hatano, K.; Umuezawa, N.; Higuchi, T. *Synthesis* **2004,** *13,* 2181.

15) Yang, J.; Swager, T. M. *J. Am. Chem. Soc,* **1998*,*** *120,* 11864.

16) Crystallographic parameters of **9**: Empirical formula: $C_{164}H_{106}$ $3(C_7H_8)$, space group: P -1, Z = 1, a = 13.6175(3) Å, b = 13.8232(3) Å, c = 23.7947(6) Å, α = 75.3253(14) °, β = 87.3257(14) °, γ = 62.2624(13) °, V = 3821.74 $Å^3$, R = 7.72%.

17) Dominguez, Z.; Dang, H.; Strouse, J. M.; Garcia-Garibay, M. A. *J. Am. Chem. Soc.* **2002**, *124,* 7719.

18) Godinez, C. E; Zapeda, G.; Mortko, C. J.; Dang, H.; Garcia-Garibay, M. A. *J. Org. Chem.* **2003,** *124,* 7719.

19) Lakowicz, J. *Principles of Fluorescence Spectroscopy,* 2^{nd} ed.; Springer: Baltimore, MD, 2004.

20) Hoatson, G. L.; Vold, R. L., *NMR: Basic Princ. Prog.* **1994,** *32,* 1-67.

21) Fyfe, C. A. *Solid State NMR for Chemists;* CFC Press: Guelph, Ontario, 1983.

22) The simulation program NMR-WEBLAB from the Spiess lab is available on the web: Macho, V.; Brombacher, L.; Spiess, H. W. *Appl. Magn. Reson.* **2001**, *20*, 405.